Experimental Investigation of Optimal Heat Removal From a Surface

by

Hamdi Kozlu

Mühendis, Istanbul Technical University (1981)
S.M. Mechanical Engineering, M.I.T. (1986)

SUBMITTED TO THE DEPARTMENT OF MECHANICAL ENGINEERING
IN PARTIAL FULFILLMENT OF THE REQUIREMENTS
FOR THE DEGREE OF

Doctor of Philosophy
at the
Massachusetts Institute of Technology

March 1989

©Massachusetts Institute of Technology 1989

Signature of Author Signature Redacted
Department of Mechanical Engineering
March 3, 1989

Certified by Signature Redacted
Professor B. B. Mikić
Thesis Supervisor

Certified by Signature Redacted
Professor A. T. Patera
Thesis Supervisor

Accepted by Signature Redacted
Professor A. A. Sonin
Chairman, Department Committee on Graduate Studies

MASS. INST. TECH.
JUL 18 1989
LIBRARIES

ARCHIVES

Experimental Investigation of Optimal Heat Removal from a Surface

by

Hamdi Kozlu

Submitted to the Department of Mechanical Engineering
in partial fulfillment for the requirements for the degree of
Doctor of Philosophy

Abstract

Minimum-momentum-transport-penalty convective heat removal from a wall to a flowing fluid stream by scale-matched flow destabilization is considered. A universal scaling for the optimization problem is developed and it is shown from Reynolds analogy-hydrodynamic stability arguments that the momentum-transport-penalty-minimizing transport solution corresponds to flow destabilization at a Reynolds number (*and associated spatial scale*) that increases (*decreases*) with increasing thermal load. On the basis of the scale-matched flow destabilization theory the search for optimal enhancement techniques can be restricted to an important class of augmentation schemes: the enhancement of *mixing* processes by the generation of *hydrodynamic instabilities* in the region in which the highest resistance to heat transfer occurs.

An experimental research program to generate the thermal-hydraulic data required to validate and exploit this optimization procedure is performed for the following augmentation schemes: a) laminar heat transfer enhancement by macro-scale destabilization of laminar channel flows by eddy promoters, and b) turbulent heat transfer enhancement by micro-scale destabilization of the (channel) viscous sublayer by micro-grooves and micro-cylinders. The significant (almost order-of-magnitude) dissipation savings possible through optimization are demonstrated in a sample study of heat transfer in a channel. The optimizing transport-enhancement scheme is shown to proceed from macro-scale eddy promoters to micro-scale micro-grooves and micro-cylinders with increasing thermal load, thus verifying the validity of scale-matched destabilization theory for optimal convective transport enhancement.

A parametric study for micro-scale destabilized turbulent flows using micro-cylinders demonstrates that the excitation of local instabilities in the viscous

sublayer leads to a reduction in momentum-transport penalties at a fixed thermal load for micro-cylinders placed at $y^+ \simeq 20$. For micro-grooved-channel flows favorable transport augmentation is obtained for a wider range of Reynolds numbers, however optimal placement still requires a matching of geometric perturbation with the sublayer scale, so as to maximize destabilization and minimize non-analogous transport.

Thesis Supervisors: Professors Bora B. Mikić and Anthony T. Patera
Thesis Committee: Professor Shahryar Motakef

Contents

Acknowledgements 9

Nomenclature 10

1 Introduction 16

2 The Optimal Heat-Transfer Design 22

2.1 Motivation 24

2.1.1 General Considerations 24

2.1.2 Nondimensionalization 26

2.1.3 Thermal-Hydraulic Analysis 28

2.2 The Optimization Problem 31

2.2.1 Scaling Analysis of the Optimization Problem 33

2.2.2 The Optimization Procedure 34

2.3 Solution to the Optimization Problem 35

2.3.1 Laminar Smooth-Channel Flow 36

2.3.2 Turbulent Smooth-Channel Flow 38

2.3.3 Reynolds Analogy Flow 41

2.4 General Hydrodynamic Considerations 45

2.5 Thermodynamic Analysis of the Optimization Problem 49

2.6 The Minimum-Dissipation-Optimization Problem With a Constant Wall Temperature Boundary Condition 52

2.6.1 Laminar Smooth-Channel Flow 56

2.6.2 Turbulent Smooth-Channel Flow 57

3 Experimental Apparatus and Measurement Techniques 59

3.1 Introduction 59

3.2 Experimental Set-up 61

3.2.1 The Wind Tunnel 61

3.2.2 Enhancement Geometries 65

3.3 Measurement Techniques 66

3.3.1 Flow Measurements 67

3.3.2 Flow Visualizations 69

3.3.3 Heat-Transfer Measurements 73

4 Results of a Channel-Optimization Study of Heat Transfer 76

4.1 Hydrodynamic Stability and Transport Processes 77

4.1.1 Linear Stability of Plane Poiseuille Flow 78

4.1.2 Stability of Eddy-Promoter Channel Flows and Heat-Transfer Enhancement 80

4.2 Thermal-Hydraulic Data 84

4.3 Optimization Results 85

5 Turbulent Heat-Transfer Augmentation 91

5.1 Background 93

5.2 Experimental Apparatus 97

5.3 Results and Discussion 99

5.4 Minimum-Dissipation Heat Removal Considerations 105

6 Conclusions **107**

A Solution to the Orr-Sommerfeld Equation by a Hermitian Finite-Element Method **111**

A.1 The Hydrodynamic Stability Problem 113

A.1.1 Linearization 113

A.1.2 The Orr-Sommerfeld Operator 114

A.2 Finite-Element Formulation of the Orr- Sommerfeld Equation . . 116

A.2.1 Weak Form 116

A.2.2 The Finite-Element Method 117

Appendix 111

Bibliography 121

Figure Captions 130

Acknowledgements

I would like to express my deepest gratitude to my supervisors, Professors Bora B. Mikić and Anthony T. Patera. Throughout the development of this thesis, I have admired their continuous patience, encouragement, guidance and productive criticisms. It has been a special privilege to have been able to work with them. I would also like to express my sincere thanks to Professor Shahryar Motakef for his constructive criticisms and friendship.

I thank all my friends in the Fluids Mechanics and Heat Transfer Laboratories for their friendship. I am also indebted to Gül Mustafa for her continuous support during my years at MIT. Finally, I would like to express my deepest appreciation to my parents and sister for their long distance support.

This work was supported by the National Science Foundation under Grant CBT 85-06146, and by the Office of Naval Research and the Defense Advanced Research Projects Agency under Contract N00014-85-K-0208.

Nomenclature

a	groove length (Figure 7b)
A	area of the $y-z$ channel-cross section
A	constant in equation (2.42)
b	distance of the micro-cylinders from the wall (Figure 7c)
B	distance of the eddy-promoters from the top wall (Figure 7a)
B	constant in equation (2.43)
c	groove dwell (Figure 7b)
c_p	specific heat at constant pressure
d	diameter of the micro-cylinders (Figure 7c)
D	diameter of the eddy-promoter cylinders (Figure 7a)
D	circular channel diameter
D_H	channel-hydraulic diameter, $4WH/2(W+H)$
∂D_B	bottom wall surface (Figure 1)
∂D_T	top wall surface (Figure 1)
e	groove depth (Figure 7b)
E	Nusselt number enhancement ratio, $Nu_{enhanced}/Nu_{smooth}$
f	friction factor defined by equation (2.13)
$g(\mu)$	function defined by equation (2.35)

$g_T(\mu)$	function defined by Section 2.6.1
$\tilde{g}(\mu)$	function defined in Section 2.3.2
$\tilde{g}_T(\mu)$	function defined in Section 2.6.2
h	enthalpy
h	heat-transfer coefficient
H	channel height (Figure 1)
$\overline{H}$	non-dimensional channel height, H/L
j	modified Colburn analogy factor, $\frac{f}{2}\frac{Re}{Nu}Pr^{\frac{1}{3}}$
k	thermal conductivity
K	loss coefficient defined in Section 3.2.1
l	distance between successive micro-cylinders (Figure 7c)
L	distance between successive eddy-promoter cylinders (Figure 7a)
L	channel length (Figure 1)
n	number of waves per geometric periodicity
Nu	Nusselt number
p	porosity defined in Section 3.2.1
p'	disturbance pressure
P	pressure
ΔP	pressure drop
Pr	Prandtl number, ν/α

q''	heat flux per unit area
Q	total heat-transfer rate (equation (2.63))
Re	Reynolds number
Re_k	Roughness Reynolds number, $u_* e(b)/\nu$
s	entropy
t	time
T	temperature
$\overline{\Delta T}$	time-averaged temperature difference between wall temperature and mixed mean temperature of the fluid
u, v, w	velocity components in the $x-$, $y-$ and $z-$directions, respectively
u', v', w'	disturbance velocity components in the $x-$, $y-$ and $z-$directions, respectively
u_*	friction velocity, $\sqrt{\tau_w/\rho}$
$\mathbf{v}$	velocity vector
W	channel width (Figures 13-15)
V	channel-average velocity defined by equation (2.1)
x, y, z	Cartesian coordinates
y^+	non-dimensional y coordinate, yu_*/ν
Y	set of fluid properties, $\{c_p, k, \nu, \rho\}$
Z_n	set of geometric parameters for channel geometry n.

GREEK SYMBOLS

α	thermal diffusivity, $k/\rho c_p$
α	non-dimensional wave number
β	constant in equation (2.43)
γ	Reynolds' analogy constant
ϵ	non-analogous momentum transfer coefficient in equation (2.54)
η	constant in equation (2.42)
λ	non-dimensional channel height, $q^{''}H/k\delta T = \Lambda\overline{H}$
Λ	non-dimensional thermal load, $q^{''}L/k\delta T$
Λ_T	non-dimensional thermal load defined in equation (2.65)
μ	non-dimensional inverse velocity, $q^{''}L/k\delta TRePr$
μ	dynamic viscosity
ν	kinematic viscosity
ω	non-dimensional frequency (equation A.6))
Ω	non-dimensional frequency (equation (4.2))
σ	non-dimensional growth constant (equation (4.2))
ξ	constant in equation (2.43)

τ_w	shear stress at the wall
Ψ	dissipation per unit width of the channel (equation (2.5))
$\overline{\Psi}$	non-dimensional dissipation parameter defined by equation (2.11).

SUBSCRIPTS

av	average
cr	critical
cl	centerline
cyl	local
in	inlet
m	mixed mean
max	maximum
min	minimum
n	channel geometry
out	exit
tr	transition
w	wall
0	base geometry, smooth channel

1	periodic eddy-promoter channel
2	periodic micro-grooved channel
3	periodic micro-cylindered channel.

SUPERSCRIPTS

$*$	optimum
UB	upper bound.

Chapter 1

Introduction

The problem of convective heat removal is one of the major considerations in the thermal-hydraulic design of important technological systems such as conventional heat exchangers and high-power-density electronic equipment. In many of these engineering applications the design of heat removal system depends on the constraints related to size, material and manufacturing cost and safety. On the other hand, in certain systems (e.g. aerospace designs and electronic equipment) functionality and extended life of the device are determined by physically limited heat removal rates at desired surface temperatures on the heated surface (Keyes [30]).

These considerations for 'effective' convective heat removal result in several important thermal-hydraulic design problems. First, for any particular application, a cost function must be introduced to reflect the constraints and goals of the overall system. For many technological applications the cost function

mainly depends on the momentum-transport penalties as well as manufacturing and material cost. It is clear that a 'good' thermal-hydraulic design requires high heat removal rates to maintain the surface temperature at a desired level with the associated low unavoidable momentum-transport penalties. Second, for the development of 'high-technology' equipment, the need for high heat removal rates at a given hydrodynamic condition is essential. It thus follows that the relationship between thermal-hydraulic design and heat-transfer augmentation is inevitable; it is clear that a 'good' understanding of the thermal-hydraulic design in unenhanced transport systems is necessary as a point of departure to gain better insight into the physical phenomena that relate transport enhancement and momentum-transport penalties.

The optimization problem for a thermal-hydraulic system from the momentum-transport-penalty viewpoint is defined as maintaining a *fixed* thermal load while *minimizing* either one of the following hydrodynamic penalties: shear stress, pressure drop or viscous dissipation (pumping power). The choice of momentum-transport-penalty heat transfer optimization is motivated by the following facts: excessive shear stress can adversely effect the structural integrity (e.g. in biomedical applications (Belhouse *et al.* [4])); excessive pressure drop can result in large structural loads leading to failure or significant cost of materials (Tuckerman and Pease [57]); and excessive power dissipation can lead to

increases in the size and cost of the prime mover, as well as in associated manufacturing and operating costs (Isaacson and Sonin [21]). Although it is clear that a design which minimizes momentum-transport penalties will be '*optimal*' from the engineering point of view, it is also clear that in many other applications other criteria may be of equal importance, such as size, material and manufacturing cost, manufacturability, safety and acoustic emission (Bergles [5]; Nakayama [40]).

A large number of studies have been undertaken in the past that aim to improve (or optimize) convective heat removal with respect to various penalties. Although momentum-transport penalties were the most important considerations in these studies, unfortunately, no study clearly demonstrated that the *optimal* thermal-hydraulic design with respect to these penalties exists for heat transfer in a plane channel flow (probably the simplest case). Following the conventional wisdom that an increase in heat-transfer rates at a fixed Reynolds number is in some sense 'good', much of this previous work on single phase flow has concentrated on the enhancement of heat-transfer coefficient (by augmentation hardware modifications, rough surfaces and flow oscillation (Bergles [5])) and the associated unavoidable increase in the friction factor with respect to smooth-channel flow.

Most of the results have been evaluated in terms of the *performance-evaluation criteria* (PEC) as given by Bergles [5], Webb and Bergles [58], and Webb and Scott [59]. As a good example, Bergles [5] presented PEC's of three different sets of geometrical constraints associated with the tube diameter and length for 12 cases of enhanced and smooth circular tubes of the same inside diameter. In this evaluation method certain geometric and thermal-hydraulic parameters (constraint variables) are kept fixed and required modifications for control variables are reported to achieve specified design objectives (e.g. required heat removal associated with low-pumping-power penalty). The main drawback of this evaluation critera is that it does not present general guidelines for the selection of proper enhancement scheme for a desired application. Therefore, the large number of augmentation schemes and number of geometric parameters in each enhancement modification leads to an intractable problem. Tuckerman [56], and Tuckerman and Pease [57] presented the minimum-pressure-drop and minimum-pumping-power optimization problems for electronic equipment applications. However, they did not extend their results for turbulent flows and they did not consider heat-transfer augmentation as a strategy to achieve the desired heat removal rates. As a result, to date, there is no general theory for the treatment of thermal-hydraulic design optimization, or an adequate understanding of the underlying physics that governs hydrodynamic behavior in augmented

transport systems.

The aim of this work is to analyze the optimal heat-transfer-design problem based on reduced variable '*universal*' scalings, and via the classical Reynolds' analogy (Reynolds [46]), to develop a broad theory relating hydrodynamic behavior and optimal scalar transport. On the basis of this theory we can restrict the number of effective (i.e. potentially optimal) enhancement techniques to an important class of augmentation techniques: the enhancement of *mixing* processes by the generation of *hydrodynamic instabilities* in the region in which the highest resistance to heat transfer occurs. The main thrust of the current work is to present a basic understanding of the underlying physical transport phenomena which permits choice of the proper enhancement scheme at a given thermal load.

In Chapter 2 we state the optimization problem for the channel flow configuration of interest and we present the analysis and solution of the optimization problem based on reduced variable 'universal' scalings. An analysis of the problem from the thermodynamic viewpoint is also presented. The results are related to general hydrodynamic stability criteria via Reynolds' analogy and extended to plane-channel flows with different thermal constraints (i.e. constant wall temperature rather than constant heat flux at the wall). In Chapter 3 we

describe experimental apparatus used to generate the thermal-hydraulic data required by the optimization procedure. In Chapter 4 we present the results of a channel optimization study based on several augmentation schemes and we briefly discuss the stability of eddy-promoter channel flows. In Chapter 5 we perform a parametric study for micro-scale destabilized turbulent flows using micro-cylinders. Lastly, in Chapter 6, conclusions of the present study are presented.

Chapter 2

The Optimal Heat-Transfer Design

In technological applications one important task is to determine the required system-design parameters (e.g. Reynolds number and channel dimensions) that yield minimum-momentum-transport penalty for a chosen convective cooling system with specified thermal requirements. In general, individually designed different cooling systems, that satisfy the same functional constraints, require different 'optimal' momentum-transport penalties at the design point. Comparison of these systems (e.g. laminar or turbulent flow in a smooth channel, or various augmentation schemes) leads to the selection of the *optimal* heat removal method and identification of flow and geometric parameters on which the design and operation of the selected system should be based. Although this selection process seems simple, the availability of a large number of heat-transfer enhancement methods results in an intractable problem.

The aim of this chapter is to investigate the possibility of the *optimal*

heat-transfer design as regards the minimum-momentum-transport-penalty convective heat removal for smooth-channel flows, and via the classical Reynolds' analogy, to develop a broad theory relating hydrodynamic behavior and optimal scalar transport. Based on the results of this theory we focus on potentially optimal enhancement techniques in which *mixing* processes are intensified by the generation of *hydrodynamic instabilities* in order to have a Reynolds-flux-dominated scalar transport (e.g. destabilization of the main flow in laminar flows and destabilization of the viscous sublayer in turbulent flow).

In Section 2.1 we consider the thermal-hydraulic design problem in a plane channel; we define the channel flow configuration of interest, and introduce a 'universal' non-dimensionalization for the problem. We then show that the *optimal* heat-transfer design, resulting in significant reductions in momentum-transport penalties, exists for heat transfer in a smooth channel. In Section 2.2 we state the optimization problem of interest. In Section 2.3 we solve the optimization problem analytically for the following flows: laminar smooth-channel flow, turbulent smooth-channel flow, and Reynolds' analogy flow. In Section 2.4 we relate the results of the solution for Reynolds' analogy flow to a general hydrodynamic stability criteria that allows *a priori* evaluation of augmentation schemes. In Section 2.5 we present the thermodynamic analysis of the optimization problem and show that the *minimum-dissipation-optimization* problem cor-

responds to the *minimum-entropy-generation-optimization* problem. In Section 2.6 we analyze the minimum-dissipation-optimization problem with a constant wall temperature and present a sample study of heat transfer in a channel for laminar and turbulent flows.

2.1 Motivation

2.1.1 General Considerations

We consider the problem shown in Figure 1 of steady-incompressible flow in a plane channel of length L and height H, with uniform heat flux q'' imposed on the top wall ∂D_T, and an adiabatic bottom surface ∂D_B. The flow is assumed to be hydrodynamically and thermally fully developed in x, independent (on average) of the spanwise coordinate z. The flow is forced by a pressure gradient $\Delta P/L$, resulting in a channel-average velocity of

$$V = \frac{1}{A}\int_{-\infty}^{+\infty}\int_{-H/2}^{+H/2} < u(x,y,z,t) > \, dy\, dz, \tag{2.1}$$

where u is the x-component of the velocity, $\mathbf{v} = u\hat{\mathbf{x}} + v\hat{\mathbf{y}} + w\hat{\mathbf{z}}$, A the area of the $y-z$ channel cross section ($= H$ per unit width of the channel), and $< . >$ refers to temporal average. The fluid is assumed to be characterized by constant

(temperature-independent) properties given by the specific heat c_p, the thermal conductivity k, the density ρ, and the kinematic viscosity ν. Natural convection and radiation are assumed negligible. The set of physical properties will be denoted $Y = \{c_p, k, \rho, \nu\}$. We choose the maximum heated wall temperature $T_{w_{max}}$ $(= T_{w_{out}})$ as our thermal constraint as this is the quantity that typically limits the functionality and performance of the device on the heated surface (e.g. computer chips (Nakayama [40]; Tuckerman [56]; Tuckerman and Pease [57])).

We now consider the general thermal-hydraulic design problem associated with the plane-channel flow of Figure 1. The aim of this section is to show that the *optimal* heat-transfer design as regards momentum-transport penalties exists even for the case of plane-channel flow. Although we consider here the thermal-hydraulic design problem associated with plane-channel flow that has the aforementioned constraints, it is clear that results can be easily extended to other geometric and thermal conditions (Mikić, Kozlu and Patera [38]).

To begin, we write the energy balance as

$$q'' L = V H \rho c_p (T_{m_{out}} - T_{m_{in}}), \tag{2.2}$$

where $T_{m_{in}}$ and $T_{m_{out}}$ are the mixed mean temperature of the fluid at the inlet $(x = 0)$ and at the exit $(x = L)$, respectively. We write the total temperature

difference (using equation (2.2)) $\delta T = T_{w_{out}} - T_{m_{in}}$ as

$$\delta T = \frac{q'' L}{\rho c_p V H} + \overline{\Delta T}, \tag{2.3}$$

where $\overline{\Delta T}$ is the time-averaged temperature difference between wall temperature and mixed mean temperature of the fluid ($\overline{\Delta T} =< T_w(x) - T_m(x) >$) and, in general, is a function of heat transfer at a given heat flux. As can be seen in Figure 2, the first term on the right-hand side of equation (2.3), the 'thermodynamic temperature rise', is the increase in the mixed mean temperature of the fluid from the inlet ($x = 0$) to the exit ($x = L$). The mixed mean temperature $T_m(x)$ is given by

$$T_m(x) = \frac{1}{V A} \int_{-\infty}^{+\infty} \int_{-H/2}^{+H/2} < u T > dy\, dz. \tag{2.4}$$

To proceed, a hydraulic performance parameter (pumping power (dissipation) per unit width of the channel) is defined as

$$\Psi = \Delta P V H. \tag{2.5}$$

2.1.2 Nondimensionalization

To reduce the thermal-hydraulic design problem of interest to a universal form, we introduce a nondimensionalization in which only fixed constraint variables (q'', δT, L, Y) (*not* control variables (H, V)) are used to scale length,

time, and temperature. To start, we introduce a Prandtl number, a Reynolds number, and a Nusselt number

$$Pr = \frac{\nu}{\alpha} \tag{2.6}$$

$$Re = \frac{V H}{\nu} \tag{2.7}$$

$$Nu(Re, Pr) = \frac{q'' H}{k \overline{\Delta T}}, \tag{2.8}$$

and a thermal load parameter

$$\Lambda = \frac{q'' L}{k \delta T}. \tag{2.9}$$

The thermal load parameter Λ can also be interpreted as a 'Nusselt number' based on the total temperature difference δT and channel length L. We define a non-dimensional channel height as

$$\overline{H} = \frac{H}{L}, \tag{2.10}$$

and a non-dimensional dissipation parameter $\overline{\Psi}$ as

$$\overline{\Psi} = \frac{L^2}{\rho \nu^3} \Delta P V H. \tag{2.11}$$

In terms of the non-dimensional variables, the energy balance equation (2.2) can be written as

$$\Lambda = \frac{1}{\frac{\overline{H}}{Nu(Re,Pr)} + \frac{1}{Re\,Pr}}. \tag{2.12}$$

Equation (2.12) must be satisfied for any thermal-hydraulic system that has the specified boundary conditions; it provides a fundamental relationship between thermal load, system geometry, coolant properties, heat-transfer performance (Nusselt number) and flow rate (Reynolds number).

To proceed further we introduce the friction factor

$$f = \frac{(\Delta P/L)\,(H/2)}{(1/2)\,\rho V^2} \tag{2.13}$$

to write equation (2.11) as

$$\overline{\Psi} = f(Re)\,\frac{Re^3}{\overline{H}^3}. \tag{2.14}$$

2.1.3 Thermal-Hydraulic Analysis

In Figure 3 we plot the dimensionless channel height $\overline{H}$ as a function of the thermal load Λ for fixed Reynolds numbers and dissipation parameters using equations (2.12) and (2.14) for the problem shown in Figure 1. We also present the same plot for circular channels in Figure 4. For circular channels we assume that uniform heat flux q'' is imposed around the perimeter and the non-dimensional channel height is taken as $\overline{H} = D/L$ where D is the diameter of circular channel (note that for circular channels the energy balance equation (equation (2.12)) needs a modification due to the different geometric constraint

(Mikić, Kozlu, Patera [38])). Air is chosen as the working fluid ($Pr = 0.71$) for both cases. For laminar flow in a plane channel we use the exact solutions (Kays and Crawford [27])

$$f = \frac{12}{Re} \tag{2.15}$$

$$Nu = 2.70. \tag{2.16}$$

For Laminar flows in circular channels we use (Kays and Crawford [27])

$$f = \frac{16}{Re} \tag{2.17}$$

$$Nu = 4.364. \tag{2.18}$$

For turbulent smooth-channel flows we use correlations for the friction factor (Hussain and Reynolds [20]; Kays and Crawford [27]) and Nusselt number (Kays and Perkins [29])(for $Re \leq 10,000$)

$$f = \frac{0.040}{Re^{0.2}} \tag{2.19}$$

$$Nu = \frac{(f/2)\,(Re - 500)\,Pr}{1.0 + 12.7\,(f/2)^{0.5}\,(Pr^{2/3} - 1)}. \tag{2.20}$$

For Reynolds numbers higher than $10,000$ we use the correlation[1] developed by Kays and Crawford [27]

$$Nu = \frac{0.142\,Re^{0.9}\,Pr}{0.833[2.25\,\ln(0.213\,Re^{0.9}) + 13.2\,Pr - 5.8]}. \tag{2.21}$$

[1]Experimental verification of these correlations is presented in Chapter 4.

It can be seen from Figures 3 and 4 that for a fixed Λ, depending on the choice of different non-dimensional channel height, dissipation[2] may vary roughly by a factor of 10^3 indicating that significant dissipation savings result from a properly designed cooling system. This analysis clearly shows that there is an *optimal* operating point (a set of Re and $\overline{H}$) to minimize the dissipation at a given thermal load even for the case of *unenhanced* heat removal for any thermal-hydaulic system.

It is clear that (from equations (2.12) and (2.14)) for a fixed $\overline{H}$ the minimum-transport-penalty-optimization problem becomes one of increasing the Nusselt number at a fixed Reynolds number while controlling the increase in the friction factor in order to achieve a specified thermal load with a smaller hydrodynamic penalty. This clearly indicates a requisite for heat-transfer enhancement implying that the design problem of optimal heat removal is best considered as a problem in hydrodynamic stability theory as first pointed out for laminar flows by Karniadakis, Mikić and Patera [25]; a more unstable flow will generate the 'desired' (higher) Reynolds fluxes at lower Reynolds numbers resulting in a reduction in momentum-transport penalties. This, in turn, implies

[2]It is also clear that similar savings in other momentum-transport penalties (e.g. shear stress and pressure drop) are possible through a proper design; henceforth, dissipation, in fact, implies either one of the momentum-transport penalties (e.g. dissipation, shear stress, or pressure drop).

that for turbulent heat-transfer enhancement destabilization process should be effected on the 'stable' part of the flow, the viscous sublayer. Effect of heat-transfer augmentation on the optimal heat-transfer design will be extensively studied in Chapter 4.

2.2 The Optimization Problem

In this section we introduce the minimum-dissipation optimization problem for the plane Poiseuille flow of Figure 1. We do not consider the minimum-stress and minimum-pressure-drop problems as they follow along similar lines. We state the minimum-dissipation optimization problem as

$$\min_{V,H,Z_n} \Psi = \{\Delta P\, V\, H\} \quad \text{for fixed} \quad \{q'', \delta T, L, Y\} \tag{2.22}$$

where the parameter Ψ is the viscous dissipation per unit width of the channel. Here, we denote the enhancement geometries by the sets Z_n. Essentially, the optimization problem (2.22) requires that for a given thermal load, q'', channel length, L, and coolant, Y, that we find the flow velocity V, channel size H, and enhancement parameters Z_n to minimize the total dissipation for a fixed maximum wall temperature δT. An equivalent procedure is to find the maximum thermal load (Λ) for a fixed dissipation parameter for the specified constraints.

As can be seen from Figures 3 and 4, there is only one maximum thermal load for each constant value of dissipation. For each optimal operating condition (Ψ_{min} for fixed Λ, or Λ_{max} for fixed Ψ), there is only one set of corresponding values of the control variables V and H for each Z_n in which we are interested.

The optimization problem corresponds to a multivariate constrained minimization problem, and inasmuch is rather to difficult to solve. Furthermore, the relationship between the dissipation and the control and constraint variables will be highly nonlinear, requiring the solution of full Navier-Stokes equation. We approach to the problem as follows: first, using the nondimensionalization procedure introduced in Section 2.1.2, we reduce the optimization problem to a 'universal' curve which can be obtained on the basis of standard thermal and hydraulic characterizations; second a physical analysis will be developed that allows for *a priori* evaluation of the relative effectiveness of various Z_n as regards dissipation minimization.

2.2.1 Scaling Analysis of the Optimization Problem

In addition to the non-dimensional parameters[3][4] introduced in Section 2.1.2, we introduce two other non-dimensional control parameters as

$$\lambda = \frac{q'' H}{k \delta T} \tag{2.23}$$

$$\mu = \underbrace{\frac{q'' L}{k \delta T}}_{A} \frac{1}{Re\, Pr}, \tag{2.24}$$

where λ is a non-dimensional channel spacing[5], and μ is a non-dimensional inverse velocity. Note μ can be interpreted as the ratio of the difference between the fluid mixed mean temperature at the exit ($x = L$) and the inlet ($x = 0$), to the total temperature difference δT. In terms of non-dimensional variables, the optimization problem (2.22) can be written as

$$\min_{\mu, \lambda, Z_n} \overline{\Psi} \quad \text{for fixed} \quad \{q'', \delta T, L, Y\} \tag{2.25}$$

subject to the fixed δT constraint (2.3)

$$\frac{\lambda}{Nu} + \mu = 1. \tag{2.26}$$

[3]We redefine here the non-dimensional dissipation parameter with a convenience constant of $\frac{3^3 2}{5^5} Pr^2$ ($\overline{\Psi} = \frac{3^3 2}{5^5} Pr^2 \frac{L^2}{\rho \nu^3} \Delta P V H$).

[4]Here, thermal-hydraulic parameters Nu and f will also depend on Z_n ($Nu = Nu(Re, Pr; Z_n)$, $f = f(Re; Z_n)$).

[5]λ can be interpreted as a different non-dimensionalized version of channel height H ($\lambda = A \overline{H}$).

To proceed further we write the non-dimensional dissipation parameter as

$$\overline{\Psi} = \frac{3^3 2}{5^5} \{f\, Re^3 \lambda^{-3} Pr^2\}. \tag{2.27}$$

Finally using the constraint $\lambda = Nu(1-\mu)$ and the relation $Re = \frac{\Lambda}{\mu Pr}$ (equation 2.24) we arrive at the following problem

$$\min_{\forall \mu \in [0,1],\, Z_n} \overline{\Psi} = \frac{3^3 2}{5^5} \frac{\Lambda^6}{Pr} \frac{f(\Lambda/\mu\, Pr;\, Z_n)}{Nu^3(\Lambda/\mu\, Pr,\, Pr;\, Z_n)\, \mu^3\, (1-\mu)^3}. \tag{2.28}$$

Note that by 'optimal Z_n' we refer to both the choice of n and the choice of non-dimensional parameters within Z_n (see Chapter 3).

It can be seen from equation (2.28) that for a given Z_n the optimal operating conditions depend only on the Prandtl number Pr, the thermal load Λ, and the non-dimensional thermal ($Nu(Re, Pr; Z_n)$) and hydraulic ($f(Re; Z_n)$) behavior of the system.

2.2.2 The Optimization Procedure

In practice, the optimization proceeds as follows:

1 choose a fluid[6] (Pr) and the thermal load (Λ);

[6]Note that high-Prandtl-number fluids are, in general, favorable coolants as regards the minimum-dissipation optimization.

2 for each Z_n find μ_n^* such that

$$\overline{\Psi}_n^* = \overline{\Psi}(\mu_n^*, Z_n) < \overline{\Psi}(\mu, Z_n) \; \forall \mu \in [0,1]; \tag{2.29}$$

3 find Z_{n^*} such that

$$\overline{\Psi}^* = \overline{\Psi}(\mu_{n^*}^*, Z_{n^*}) < \overline{\Psi}(\mu_n^*, Z_n) \; \forall \, Z_n. \tag{2.30}$$

The dimensional V and H are then determined as follows: μ implies Re, Nu and hence λ; λ implies H; knowledge of H and Re then gives the velocity V. Examples of the optimization procedure based on several augmentation schemes will be given in Chapter 4.

2.3 Solution to the Optimization Problem

We consider here three cases in which the optimization problem (2.28)

$$\overline{\Psi}^* < \overline{\Psi} = \frac{3^3 2}{5^5} \frac{\Lambda^6}{Pr} \frac{f(\Lambda/\mu\, Pr)}{Nu^3(\Lambda/\mu\, Pr,\, Pr)\; \mu^3\,(1-\mu)^3} \quad \forall \mu \in [0,1] \tag{2.31}$$

can be 'solved' in closed form. The three flows amenable to analytical treatment are: laminar smooth-channel flow; turbulent smooth-channel flow; and Reynolds' analogy flows. These exact optimizations are interesting not only in terms of the results they produce, but also in terms of the insight they give into the hydrodynamic behavior in augmented transport systems.

2.3.1 Laminar Smooth-Channel Flow

For laminar smooth-channel flow we have the exact solutions (Kays and Crawford [27])

$$f = \frac{12}{Re} \tag{2.32}$$

$$Nu = 2.70 \tag{2.33}$$

giving for $\overline{\Psi}(\mu)$

$$\overline{\Psi}(\mu) = \frac{3^3 2}{5^5} \frac{12\,\Lambda^5}{2.70^3} \frac{1}{\mu^2\,(1-\mu)^3}. \tag{2.34}$$

We now minimize the function

$$g(\mu) = [\mu^2\,(1-\mu)^3]^{-1} \quad \mu \in [0,1]. \tag{2.35}$$

It is readily shown from Figure 5 that $g(2/5) \leq g(\mu)$ for all $\mu \in [0,1]$, from which it directly follows that

$$\mu^* = 2/5 \tag{2.36}$$

$$\overline{\Psi}^* = 0.305\,\Lambda^5. \tag{2.37}$$

It is also clear from Figure 5 that the 'near-optimal' operating conditions can be achieved for $0.3 < \mu < 0.5$, whereas operating outside this range results in drastic increases in dissipation (this result becomes an important issue in studying enhanced heat-transfer systems). The result $\overline{\Psi}^* = 0.305\ \Lambda^5$ is only valid for a limited range of Λ, as laminar flow can only occur for $Re < Re_{tr}$. We

take Re_{tr} here to be $Re_{tr} = 1,300$; although Re_{tr} can be larger than this value in quiet experiments, in most engineering situations $Re_{tr} = 1,300$ is a very good predictor of transition (Schlichting [47]). This implies from equation (2.24) that we should minimize $\overline{\Psi}(\mu)$ only for $(\Lambda/Re_{tr}Pr) < \mu < 1$. If $(\Lambda/Re_{tr}Pr) < 2/5$ our previous result holds, $\mu^* = 2/5$, $\overline{\Psi}^* = 0.305\,\Lambda^5$, however, if $(\Lambda/Re_{tr}Pr) > 2/5$ the minimum $\overline{\Psi}$ now occurs at the end point $\mu = \Lambda/Re_{tr}\,Pr$. Our final result for laminar flow is therefore

$$0 < \Lambda < \frac{2\,Re_{tr}\,Pr}{5} = 369.2, \quad \mu^* = 2/5, \quad \overline{\Psi}^* = 0.305\,\Lambda^5 \tag{2.38}$$

$$369.2 < \Lambda < Re_{tr}\,Pr = 923, \quad \mu^* = \Lambda/923, \quad \overline{\Psi}^* = \frac{8975.05\,\Lambda^3}{(1-(\frac{\Lambda}{923}))^3}, \tag{2.39}$$

where the numerical values given are for $Pr = 0.71$, $Re_{tr} = 1,300$. No laminar solution exists for $\Lambda > Re_{tr}Pr = 923$, as in the this case the mixed-mean temperature rise *alone* is greater than the allowable δT for which the energy balance equation (2.2) is violated (recall that μ is the ratio of the difference between the fluid mixed mean temperature at the exit ($x = L$) and the inlet ($x = 0$), to the total temperature difference δT).

In Figure 6 we plot the optimal dissipation $\overline{\Psi}^*$ as a function of the thermal load Λ for laminar flows. It can be seen that as Λ approaches the limiting value $Re_{tr}\,Pr = 923$ the dissipation goes to infinity, as $V\,H$ is finite but H goes to zero.

Knowing the optimal value of $\mu^* = 2/5$, we find the optimal flow-Reynolds number and the optimal channel height as a function of thermal load (using equations (2.24) and (2.23)) as

$$Re^* = 3.52\,\Lambda \tag{2.40}$$

$$\overline{H}^* = \frac{1.62}{\Lambda}, \tag{2.41}$$

where the numerical value in equation (2.40) is for $Pr = 0.71$. Again the above optimal design parameters are for $(\Lambda/Re_{tr}Pr) < 2/5$.

2.3.2 Turbulent Smooth-Channel Flow

We assume here power-law correlations for the friction factor and Nusselt number

$$f = A\,Re^{\eta} \tag{2.42}$$

$$Nu = B\,Re^{\beta}\,Pr^{\xi} \tag{2.43}$$

giving

$$\overline{\Psi}(\mu) = \frac{3^3 2}{5^5}\,\frac{A}{B^3}\,\frac{\Lambda^{6+\eta-3\beta}}{Pr^{1+\eta+3\xi-3\beta}}\,\frac{1}{\mu^{3+\eta-3\beta}\,(1-\mu)^3}. \tag{2.44}$$

Defining the function $\tilde{g}(\mu) = [\mu^{3+\eta-3\beta}(1-\mu)^3]^{-1}$ it can be readily shown that for $\mu^* = \frac{3+\eta-3\beta}{6+\eta-3\beta}$, $\tilde{g}(\mu^*) \leq \tilde{g}(\mu)\ \forall\,\mu \in [0,1]$, from which the corresponding minimum

dissipation can be calculated from equation (2.44) as

$$\overline{\Psi}^* = \frac{3^3 2}{5^5}\,\frac{A}{B^3}\,\frac{\Lambda^{6+\eta-3\beta}}{Pr^{1+\eta+3\xi-3\beta}}\left(\frac{3+\eta-3\beta}{6+\eta-3\beta}\right)^{3\beta-3-\eta}\left(\frac{3}{6+\eta-3\beta}\right)^{-3}. \qquad (2.45)$$

For turbulent flow in the channel shown in Figure 1 we have $A = 0.04$, $\eta = -0.2$, $B = 0.019$, $\beta = 0.8$, $\xi = 0.5$ (Kays and Crawford [27]) for which we obtain

$$\mu^* = 2/17 \qquad (2.46)$$

$$\overline{\Psi}^* = 333.66\,\Lambda^{3.4}, \qquad (2.47)$$

where the numerical value in equation (2.47) is for $Pr = 0.71$. The value of $\mu^* = 2/17$ for a turbulent flow is less than the corresponding value $\mu^* = 2/5$ (equation (2.36)) for a laminar flow, implying that for optimal-performance turbulent flow relatively more of the temperature rise should be lateral as opposed to streamwise. Note that for any Z_n that has a thermal ($Nu(Re, Pr; Z_n)$) and hydraulic ($f(Re; Z_n)$) data in the form of equations (2.42) and (2.43), minimum dissipation can be easily obtained from the equation (2.45).

Turbulent flows can only exist for $Re > Re_{tr}$ implying that $\mu < (\Lambda/Re_{tr}\,Pr)$, and thus equation (2.46) and (2.47) are, in fact, only valid for $(\Lambda/Re_{tr}\,Pr) > 2/17$. To be more precise for lower Λ an 'endpoint' analysis similar to that used

for laminar flows is performed. Our final result for turbulent flow is therefore

$$0 < \Lambda < \frac{2\,Re_{tr}\,Pr}{17} = 108.59, \quad \mu^* = \frac{\Lambda}{923}, \quad \overline{\Psi}^* = \frac{97.38\,\Lambda^{3.4}}{(\frac{\Lambda}{923})^{0.4}(1-\frac{\Lambda}{923})^3} \tag{2.48}$$

$$108.59 < \Lambda, \quad \mu^* = \frac{2}{17}, \quad \overline{\Psi}^* = 333.66\,\Lambda^{3.4}. \tag{2.49}$$

In Figure 6 we also plot the optimal dissipation $\overline{\Psi}^*$ as a function of the thermal load Λ for turbulent flows. Referring to Figure 6, for low Λ, laminar flow performs better than turbulent flow. As Λ increases, turbulent flow becomes more efficient than laminar flow since transition to the turbulence causes relatively large increase in Nusselt number than the corresponding increase in dissipation, resulting in reduced dissipation at the same thermal load.

We again calculate the optimal flow Reynolds number and the optimal channel height (for $\Lambda > 108.59$) as a function of thermal load for turbulent flow (using equations (2.24) and (2.23)) as

$$Re^* = 11.97\,\Lambda \tag{2.50}$$

$$\overline{H}^* = \frac{0.103}{\Lambda^{0.2}}, \tag{2.51}$$

where the numerical values given are for $Pr = 0.71$.

2.3.3 Reynolds Analogy Flow

An analogy existing between any two scalar quantities (e.g. heat and momentum (Reynolds [46])) has a significant importance in many engineering applications, in which expressing the variables underlying the transport process of one scalar quantity (usually heat) in terms of the variables underlying the transport process of the other scalar quantity (momentum) plays an essential part in the prediction of heat transfer. Investigations on the existence of analogies for general flows, therefore, have occupied a substantial part of the research in heat transfer.

The earliest work is reported by Reynolds [46] in 1874 in which he stated that the rate of any scalar transport (e.g. heat and momentum) depends on the molecular and turbulent exchange caused by eddy motions. It is clear from the constitutive relations (governing the total heat and momentum transfer) that direct proportionality between shear stress and heat transfer is expected in flows having the similar velocity and temperature boundary conditions in the absence of viscous heating and compressibility if turbulent exchange dominates and the turbulent Prandtl number of unity (we also assume that the molecular Prandtl number is different than 1). In the case of turbulent flows this criteria is generally satisfied with the exception of a relatively small region near the wall,

the viscous sublayer.

The classical Reynolds' analogy is extended mainly to pipe flows due to their technological importance by considering the two important regions of the fluid: the turbulent region in which turbulent exchange dominates, and a 'viscous-laminar' region (the viscous sublayer) in which molecular transport is significant (Prandtl [45]; Taylor [51]; Von Karman [22]; Colburn [7]). However, to date, no rigorous theoretical work exists to verify the validity of the Reynolds analogy for general flows except for the recent paper by Magen, Mikić and Patera [34], in which an upper bound for forced convection in turbulent plane Couette flow has been obtained.

Our aim in this section is to establish a basis for the understanding of hydrodynamic behavior in enhanced heat-transfer systems via the classical Reynolds' analogy. This, in turn, implies the choice of the proper enhancement scheme at a given thermal load.

To start, we first consider the plane-channel flow shown in Figure 1. For this flow, Reynolds' analogy is expressed as

$$\frac{< \tau_w >}{\mu \frac{V}{H}} = \frac{\gamma q''}{k \frac{\overline{\Delta T}}{H}}, \tag{2.52}$$

where $< \tau_w >$ is the shear stress at the wall and μ the dynamic viscosity of

the fluid. Here, γ[7] is 'Reynolds' analogy constant' which, in general, scales as $Pr^{-1/3}$ and is a function only of Prandtl number.

As is well known, the Reynolds analogy is exact for a laminar boundary layer flow on an isothermal plate at Prandtl number of unity ($\gamma = 1$), in which the transport processes of heat and momentum are dominated by a convective-diffusive balance in the absence of viscous heating and compressibility (Schlichting [47]). In laminar internal flows γ is strongly sensitive to the choice of mean scales indicating that the analogy is not 'valid'; there is no convective-diffusive balance in the purely diffusive laminar flow, thus, γ depends on the boundary conditions and forcing functions. It is also a well known fact that, the analogy holds (within several percent) for the internal and boundary layer turbulent flows ($\gamma = Pr^{-1/3}$, Colburn [7]) is due to the fact that the transport to the wall in these flows can be described as a series of coherent boundary layer events in the viscous sublayer (the surface-renewal model (Thomas [53]; Mikić [36])) and that the effect of the pressure gradient in internal flows on destroying the analogy is negligible (at least experimentally). The length scale of these 'coherent' sublayer structures in the viscous sublayer is very small compared to the mean-

[7]Although the precise value of γ depends on the chosen velocity V and temperature scale $\overline{\Delta T}$ (Karniadakis, Mikić and Patera [25]), it is relatively insensitive to the choice of mean variables in high-Reynolds-number turbulent flows as a result of the well-mixed core flow (Taylor [51]).

flow length scale so that a roughly 'constant temperature' boundary condition is achieved over these length scales; it is because of that, the analogy 'weakly' (well within the limits of experimental uncertainties) depends on the thermal boundary conditions in internal and boundary-layer turbulent flows. In terms of our non-dimensional variables (equations (2.13), (2.8), and (2.7)) equation (2.52) can be written as

$$f(Re) = \frac{2\gamma\, Nu(Re,\, Pr)}{Re}. \tag{2.53}$$

Extension of the classical Reynolds' analogy to flows with augmentation hardware modifications (e.g. eddy promoter flows) are given by Karniadakis, Mikić and Patera [25] in that a second term involving the drag on the cylinder is added to the right-hand side of equation (2.53) that represents the non-analogous momentum transfer; eddy-promoters are specified as adiabatic; it then follows that the shear stress and pressure forces on the cylinder have no thermal analogue. It is important to note that these considerations are generally valid for any flow having augmentation hardware modifications. Then, our 'Reynolds' analogy equation' for these flows can be written as

$$f(Re;\, Z_n) = \frac{2\gamma\, Nu(Re,\, Pr;\, Z_n)}{Re} + \frac{\epsilon(Re;\, Z_n)}{Re}. \tag{2.54}$$

Note that although equation (2.54) is perfectly general, it will only be

useful for small ϵ/Nu. A more detailed analysis of ϵ for transitional eddy promoter flows is given by Karniadakis [24].

We now insert equation (2.54) into equation (2.28), and neglect the $0(\epsilon)$ term to reduce our minimization problem to

$$\overline{\Psi}(\mu) = \frac{3^3 2}{5^5} \frac{\gamma \Lambda^5}{Nu^2(\Lambda/\mu\, Pr,\, Pr)} \frac{1}{\mu^2 (1-\mu)^3}. \tag{2.55}$$

To proceed further we construct an *upper* bound for the minimum of $\overline{\Psi}(\mu)$ by neglecting the variation of Nu with μ and minimizing the function

$$g(\mu) = [\mu^2 (1-\mu)^3]^{-1} \quad \mu \in [0,1]. \tag{2.56}$$

It is shown that (see Section 2.3.1) $g(2/5) \leq g(\mu)$ for all $\mu \in [0,1]$, from which it directly follows that

$$\mu^{*UB} = \frac{2}{5} \tag{2.57}$$

$$\overline{\Psi}_n^{*UB} = \gamma \Lambda^5\, Nu^{-2}(\frac{5\,\Lambda}{2\,Pr},\, Pr;\, Z_n). \tag{2.58}$$

This result is extensively analyzed in the next section.

2.4 General Hydrodynamic Considerations

The general minimization procedure presented in Section 2.2.2 for a given Z_n is relatively simple, and can be effected once one set of experimen-

tal evaluations of $Nu(Re, Pr; Z_n)$ and $f(Re; Z_n)$ have been conducted for any H. Unfortunately, the number of parameters in each enhancement geometry Z_n (see Chapter 3), and potentially large number of augmentation schemes (Bergles [5]) can lead to an intractable problem in determining the proper enhancement method at a given thermal load. It is thus clear that a broad theory relating hydrodynamic behavior and scalar transport is required in order to reduce the number of effective enhancement geometries that are potentially optimal as regards the minimum-dissipation optimization.

In this section we analyze the result (equation (2.58)) obtained from the solution of the optimization problem for Reynolds analogy flow to understand the hydrodynamic behavior and scalar transport in augmented transport systems. We then perform an experimental research program which will be desribed in the next chapter to demonstrate the validity of physical arguments which will be described below.

Taking the upper bound for $\overline{\Psi}^*$ as given in equation (2.58), and that $\overline{\Psi}^{*UB}$ and $\overline{\Psi}^*$ behave similarly we can make the following conclusions as regards the relationship between augmentation and minimum-dissipation optimization.

First, we see that an increase in Nu at fixed Re (here $5\Lambda/2Pr$) by an enhancement Z_n *does* result in a quadratic decrease in dissipation. This

is consistent with the conventional wisdom that an increase in Nu at fixed Re is in some sense 'good'. This condition is necessary but not sufficient to yield a reduction in dissipation as we also require ϵ to be small in equation (2.54), so as to maximize destabilization and minimize non-analogous transport. It thus follows that the larger heat-transfer enhancement may not be optimal as pertains minimum-dissipation optimization. Note that for the minimum-stress and minimum-pressure-drop problems the results are similar, however, the reduction in these quantities is only linear in Nu^{-1}. The desired increase in Nu at fixed Re is best considered as a decrease in the stability of the flow, that is, an increase in the correlated velocity-temperature fluctuations (Ghaddar, Mikić and Patera [15]; Greiner [17]; Karniadakis, Mikić and Patera [25]). The more unstable flow will have a lower critical Reynolds number which results in a Reynolds-flux-dominated transport at a lower Reynolds number for which the same heat-transfer rate is achieved as in the case of high-Reynolds-number flows. The enhancement problem then becomes one of maximizing destabilization while maintaining non-analogous momentum transport small.

It is clear that once a flow is destabilized by some enhancement hardware modifications (e.g. eddy promoters, rough surfaces) at some critical Reynolds number Re_{cr} (corresponding to a certain Λ), for $Re \gg Re_{cr}$ there will be significant non-linear saturation; the relative increase in Nusselt number will decrease,

and non-analogous drag will dominate. It thus follows that as the thermal load Λ increases, an enhancement procedure is required to modify the Nusselt number at higher Reynolds number. In essence, equation (2.58) indicates that $5\Lambda/2\,Pr$ is roughly (since we neglected the variations of Nu with Re and we assumed $\epsilon \rightarrow 0$) the Reynolds number at which the most important dissipation reduction is achieved; increase in Nu at other Reynolds numbers will have a less significant effect at this thermal load Λ. As we know with increasing Reynolds number the range of naturally unstable scales increases (e.g. the energy cascade), this implies that with increasing Λ we require destabilization at smaller and smaller (intrinsically stable) spatial scales-in essence, *scale-matched destabilization.*

The scale-matched flow destabilization regarding the minimum-dissipation optimization can be physically interpreted as follows. As is well known, the only scalar transport mechanism in a laminar flow is the molecular conduction between the fluid particles. An increase in the transport rates can be best achieved by creating the Reynolds-flux-dominated transport (eddy convection), that is, to destabilize the flow at the naturally stable scales of motion (e.g. destabilization of main flow). However, when the flow becomes turbulent, it is clear that the main resistance to heat transport occurs in the viscous sublayer requiring that an effective enhancement scheme should destabilize this 'laminar-like' near-wall region to achieve a desired increase in transport rates.

To verify the validity of scale-matched destabilization in utilizing the optimization procedure an experimental research program is carried out based on the above physical arguments. We apply the theory of scale-matched destabilization in order to achieve minimum dissipation convective heat removal over all possible Λ by considering the following enhancement schemes: a) laminar heat-transfer enhancement by macro-scale destabilization of channel flows by eddy promoters (Figure 7a); b) turbulent heat-transfer enhancement by micro-scale destabilization of the viscous sublayer by micro-grooves (Figure 7b) and micro-cylinders (Figure 7c). The experimental research program will be described in the next chapter.

2.5 Thermodynamic Analysis of the Optimization Problem

In the previous sections we have studied the optimal heat-transfer design utilizing fundamental balance equations (e.g. energy and momentum) and constitutive relations. We consider here the optimal heat-transfer design from the thermodynamic viewpoint, in which we minimize the entropy generation that results from irreversibilities in the system; for the problem of interest

the primary sources of irreversibilities are the heat-transfer process over a finite temperature difference, and friction between the fluid and solid boundaries due to the bulk flow. Our aim is to investigate the relationship between the *minimum-dissipation-optimization* problem and *minimum-entropy-generation-optimization* problem.

We consider the same problem shown in Figure 1. To start, we write the energy balance[8] for an infinitesimal control volume as

$$\rho V H \, dh = q'' \, dx \tag{2.59}$$

which states that the enthalpy increase of the fluid is equal to the total heat input through the boundary (see Figure 1) in the absence of any change in potential and kinetic energy. Here, dh represents the differential change in enthalpy. Entropy balance for the same control volume can also be written as

$$d\dot{S}_{irr} = \rho V H \, ds - \frac{q''}{T + \overline{\Delta T}} \, dx, \tag{2.60}$$

where ds is the differential change in entropy, T the temperature in K, $\overline{\Delta T} =< T_w - T_m >$, and $d\dot{S}_{irr}$ the total entropy generation in this infinitesimal control volume.

[8] We denote an extensive property by a capital letter and an intensive property by a lowercase letter.

To proceed further, we write the equation of state of a simple compressible substance (Huang [19]) as

$$T\,ds = dh - v dP, \tag{2.61}$$

where v is the specific volume and dP the differential change in pressure. Equation (2.61) is also known as the $T - ds$ equation in thermodynamics which enables us to calculate the entropy change from measurable quantities. Substituting equation (2.61) into (2.60) and using (2.59) we arrive at the following equation

$$\frac{d\dot{S}_{irr}}{dx} = \frac{q''\,\overline{\Delta T}}{T\,(T + \overline{\Delta T})} + \frac{V\,H}{T}\left(-\frac{dP}{dx}\right), \tag{2.62}$$

where $\frac{d\dot{S}_{irr}}{dx}$ is the total entropy generation due to irreversibilities per unit width and per unit length of the channel. It is clear from equation (2.62) that the entropy generation occurs as a result of the heat transfer from wall to fluid (first term on the left-hand side of equation (2.62)) and friction between the fluid and solid boundaries as a result of the bulk flow (second term on the left-hand side of equation (2.62)). As can be seen for $\overline{\Delta T}/T \ll 1$, which is usually the case in many engineering applications, first term is negligible compared to the second term[9]. It is also clear that the first term will become smaller in enhanced heat removal systems, in which a decrease in $\overline{\Delta T}$ is a requisite in order to achieve a

[9]It can be shown that error in neglecting the first term in equation (2.62) is within several percent indicating that frictional losses dominate.

higher heat-transfer coefficient compared to smooth-channel flow. The second term $\{dP\,V\,H\}$ is, in fact, the viscous dissipation term for the considered control volume on which our minimum-dissipation optimization is based.

As a result of the above analysis we conclude that the *minimum-dissipation-optimization* problem is equivalent to the *minimum-entropy-generation-optimization* problem under the assumption that $\overline{\Delta T}/T \ll 1$.

2.6 The Minimum-Dissipation-Optimization Problem With a Constant Wall Temperature Boundary Condition

We consider here the problem shown in Figure 8 of steady-incompressible flow in a plane channel of length L and height H, with a constant wall temperature T_w on the top wall ∂D_T, and an adiabatic bottom surface ∂D_B[10]. Applications of the specified problem can be found in industrial condenser type of heat exchangers (Kays and London [28]). The flow is assumed to be hydrodynamically and thermally fully developed in x, independent (on average) of the

[10]This is the problem stated in Section 2.1.1 except that we change the top wall boundary condition as a constant wall temperature.

spanwise coordinate z. We proceed using the same procedure as in the previous optimization problem in order to analyze the minimum-dissipation optimization for the present configuration.

To begin, we write the energy balance as

$$Q = V\,H\,\rho\,c_p\,(T_{m_{out}} - T_{m_{in}}), \tag{2.63}$$

where Q is the total energy that has to be removed by the fluid. Since $T_{m_{out}} - T_{m_{in}} = (T_w - T_{m_{in}}) - (T_w - T_{m_{out}})$ as seen in Figure 9, we can write equation (2.63) as

$$\frac{Q}{V\,H\,\rho\,c_p} = \delta T - \overline{\Delta T}_{out}, \tag{2.64}$$

where δT is the total temperature difference in the system ($\delta T = T_w - T_{m_{in}}$), and $\overline{\Delta T}_{out}$ the time-averaged temperature difference between wall temperature and mixed mean temperature of the fluid at the exit $x = L$ ($\overline{\Delta T}_{out} =< T_w - T_{m_{out}}(x) >$). In terms of the Prandtl number Pr, the Reynolds number Re, defined as in Section 2.1.2 (equations (2.6) and (2.7)), and the thermal load parameter Λ_T, redefined as

$$\Lambda_T = \frac{(Q/L)\,L}{k\,\delta T} = \frac{q''_{av}\,L}{k\,\delta T}, \tag{2.65}$$

where q''_{av} is the average heat flux on the top wall ∂D_T, the global energy balance becomes

$$\Lambda_T = Re\,Pr\,\left(1 - \frac{\overline{\Delta T}_{out}}{\delta T}\right). \tag{2.66}$$

This is, in fact, our constraint for the current optimization problem. Applying the energy balance for an infinitesimal control volume and integrating over the channel length L yields

$$\frac{\overline{\Delta T}_{out}}{\delta T} = \exp\left(-\frac{h\,L}{V\,H\,\rho\,c_p}\right), \tag{2.67}$$

where h is the heat-transfer coefficient. Using our non-dimensional parameters we express equation (2.67) as

$$\frac{\overline{\Delta T}_{out}}{\delta T} = \exp\left(-\frac{Nu}{Re\,Pr\,\overline{H}}\right). \tag{2.68}$$

Substituting equation (2.68) into equation (2.66) we arrive at the following equation

$$\Lambda_T = Re\,Pr\,\left(1-\exp\left(-\frac{Nu}{Re\,Pr\,\overline{H}}\right)\right). \tag{2.69}$$

Equation (2.69) is the equivalent of equation (2.12) which was obtained for the constant heat flux case, and must be satisfied for any thermal-hydraulic system that has the specified constraints; it provides a fundamental relationship between thermal load, system geometry, coolant properties, heat-transfer performance (Nu), and flow rate (Re).

In Figure 10 we plot the dimensionless channel height $\overline{H}$ as a function of the thermal load Λ for fixed Reynolds numbers and dissipation parameters using equations (2.69) and (2.11) for the problem shown in Figure 8. For laminar flow

we use the exact solutions (Kays and Crawford [27])

$$f = \frac{12}{Re} \tag{2.70}$$

$$Nu = 2.43, \tag{2.71}$$

whereas we use the correlations given in equations (2.19), (2.20), and (2.21) for turbulent flow. It is clear from Figure 10 that our results obtained in Section 2.1.3 are also valid for the present case of interest reconfirming that the momentum-transport penalties can be minimized at a given thermal load in a channel-heat-transfer design.

Substituting equation (2.69) in equation (2.11) and using the definitions of the friction factor and Nusselt number (equations (2.13) and (2.8)) we arrive at the following optimization problem

$$\min_{\forall \mu \in [0,1], Z_n} \overline{\Psi} = -\frac{3^3 2}{5^5} \frac{\Lambda_T}{Pr^3} \frac{f(Re;\, Z_n)\ [\ln(1-\mu)]^3}{Nu^3(Re,\, Pr;\, Z_n)\ \mu^6}. \tag{2.72}$$

It can be seen from equation (2.72) that, as in the previous study, for a given Z_n the optimal operating conditions depend only on the Prandtl number Pr, the thermal load Λ_T, and the non-dimensional thermal ($Nu(Re, Pr; Z_n)$) and hydraulic ($f(Re; Z_n)$) behavior of the system. The optimization procedure for the augmentation sets Z_n is the same as the procedure given in Section 2.2.2. In the following sections we give the exact solution to the optimization problem

for laminar smooth-channel flow and turbulent smooth-channel flow. We do not consider here Reynolds analogy flows as they follow along similar lines (see Section 2.3.3).

2.6.1 Laminar Smooth-Channel Flow

For laminar smooth-channel flow we have the exact solution for the friction factor (equation (2.70)) and Nusselt number (equation (2.71)) giving for $\overline{\Psi}(\mu)$

$$\overline{\Psi}(\mu) = -\frac{3^3 2}{5^5}\frac{12\,\Lambda_T^5}{2.43^3\,Pr^2}\frac{[\ln(1-\mu)]^3}{\mu^5}. \tag{2.73}$$

We now minimize the function $g_T = \frac{[\ln(1-\mu)]^3}{\mu^5}$ $\mu \in [0,1]$. It is readily shown from Figure 11 that $g_T(0.615) \leq g(\mu)$ for all $\mu \in [0,1]$ from which it directly follows that

$$\mu^* = 0.615 \tag{2.74}$$

$$\overline{\Psi}^* = 0.311\,\Lambda_T^5 \tag{2.75}$$

$$Re^* = 2.29\,\Lambda_T \tag{2.76}$$

$$\overline{H}^* = \frac{1.57}{\Lambda_T}. \tag{2.77}$$

It is clear from Figure 11 that the 'near-optimal' operating conditions can be also achieved for $0.5 < \mu < 0.7$, whereas operating outside this range results in drastic

increases in dissipation. The above numerical values are given for $Pr = 0.71$. Laminar flow can only exist for $Re < Re_{tr}$, and these equations (2.74)-(2.77) are, in fact, only valid for $\Lambda_T/Re_{tr}Pr < 0.615$. However, if $\Lambda_T/Re_{tr}Pr > 0.615$ to be more precise, an 'endpoint' analysis should be performed similar to that presented in Section 2.3.1.

2.6.2 Turbulent Smooth-Channel Flow

We assume here power-law correlations for the friction factor (equation (2.42)) and Nusselt number (equation (2.43)) giving

$$\overline{\Psi}(\mu) = -\frac{3^3 2}{5^5} \frac{A\,\Lambda_T^{6-3\beta+\eta}}{B^3\,Pr^{3-3\beta+3\xi+\eta}} \frac{[\ln(1-\mu)]^3}{\mu^{6-3\beta+\eta}}. \tag{2.78}$$

Defining the fuction $\tilde{g}_T = \frac{[\ln(1-\mu)]^3}{\mu^{6-3\beta+\eta}}$ it can be shown that to find the μ^* the following equation has to be solved for a given β and η:

$$\frac{(1-\mu)\,\ln(1-\mu)}{\mu} = -\frac{3}{6-3\beta+\eta}. \tag{2.79}$$

For turbulent flow in the channel shown in Figure 8, we have $A = 0.04$, $\eta = -0.2$, $B = 0.019$, $\beta = 0.8$, $\xi = 0.5$ (Kays and Crawford [27]) for which we obtain

$$\mu^* = 0.225 \tag{2.80}$$

$$\overline{\Psi}^* = 510\,\Lambda_T^{3.4} \tag{2.81}$$

$$Re^* = 6.26\,\Lambda_T \tag{2.82}$$

$$\overline{H}^* = \frac{0.061}{\Lambda_T^{0.2}}. \tag{2.83}$$

The above results are valid for $(\Lambda_T/Re_{tr}Pr) > 0.225$ (see Section 2.3.2) and $Pr = 0.71$.

Comparison of these exact solutions for laminar flow and turbulent flow with the previous case clearly shows that the optimization process with a constant wall temperature follows along similar lines and that the significant dissipation savings are possible through the optimal design.

Chapter 3

Experimental Apparatus and Measurement Techniques

3.1 Introduction

The design and operation of the experimental apparatus and measurement techniques used to investigate the thermal-hydraulic behavior in destabilized channel flows of interest are described in this chapter. On the basis of scale-matched destabilization theory to achieve the *optimal* thermal-hydraulic design as regards the minimum-momentum-transport-penalty optimization, we consider here three heat-transfer enhancement geometries corresponding to the addition of a) streamwise-periodic eddy-promoters, b) streamwise-periodic micro-grooves, and c) streamwise-periodic micro-cylinders, shown schematically in Figures 7a, 7b, and 7c, respectively. Eddy promoters and micro-cylinders are adiabatic, and thus they effect the heat transfer only through flow modification.

We shall denote the base geometry in Figure 1 as Z_0 and desribe the three enhancement geometries by the sets Z_n, $Z_1 = \{D/H, B/H, L/H\}$ for the eddy promoters, $Z_2 = \{e/H, a/H, c/H\}$ for the micro-grooved channels, and $Z_3 = \{d/H, b/H, l/H\}$ for the micro-cylindered channels for which a parametric study will also be presented in Chapter 5 for different geometric configurations by changing the distance between successive micro-cylinders, and the diameter of the micro-cylinders. Here D is the eddy-promoter-cylinder diameter, B the distance between the eddy promoters and the top wall, and L the distance between successive cylinders in the array; e is the micro-groove depth, a the micro-groove length, and c the micro-groove dwell; d is the micro-cylinder diameter, b the distance between the micro-cylinders and the top/bottom wall, and l the distance between successive micro-cylinders in the array. Note that micro-cylinders are the scaled-down version of the eddy promoters to the viscous sublayer scale (see Chapter 5). The geometries Z_0, Z_1, Z_2, Z_3 are all periodic, and thus the concept of being fully developed is well defined (Ghaddar, Karniadakis and Patera [13]; Patankar, Liu and Sparrow [43]).

In Section 3.2 we describe the experimental apparatus which consists of a low-speed wind tunnel and an individual test section for each enhancement geometry. In Section 3.3 we present the measurement techniques for the flow and heat-transfer measurements and flow visualization methods employed for

the eddy-promoter channel flows.

3.2 Experimental Set-up

3.2.1 The Wind Tunnel

A low-speed wind tunnel built in order to perform the experimental research is shown schematically in Figure 12. The purpose of the wind tunnel is to obtain the uniform mean flow with a low turbulence level in the test section to conduct the required heat-transfer and fluid-flow measurements for the optimization studies undertaken. In this double-contraction open-circuit wind tunnel air follows a straight path from entrance to the test section. The necessary dust-free air for the wind tunnel is supplied from an existing compressor of capacity of about 1,000 scfm at 5 psig pressure. Although much higher Reynolds-number flows can be achieved as a result of this abundant air supply, the maximum Reynolds number in the experiments is kept about 150,000 (based on the hydraulic diameter of the test section of $9'' \times 1''$ and average-flow velocity) to avoid the possible compressibility effects associated with high velocities. Below we discuss the segments of the wind tunnel to describe their important design characteristics related to their functions.

Temperature of the air is controlled by a custom-made heat exchanger located at the entrance of the wind tunnel. This cross-flow heat exchanger, consisting of four 'honeycomb-like' plate-fin structured segments connected in parallel via a manifold, has also effect on straightening the air flow entering the diffuser. City water is used as the coolant and water flow rate is regulated by a throttle valve located in the upstream of the manifold to achieve the desired air temperature in the test section.

The heat exchanger is followed by a three-dimensional diffuser in which kinetic energy is converted into static energy at the exit in order to reduce the air velocity in a relatively short distance without creating any intermittant or steady flow separation prior to the settling chamber; the separation of the flow might cause oscillations in the velocity and vibrations in the wind tunnel. Since the design of a diffuser unavoidably depends on its geometry (e.g. divergence angle, area ratio, wall shape) and inlet and exit conditions, and almost all data are on two-dimensional diffusers and empirical (Kline, Moore, and Cochran [31]), the proper design for a special application is to design the diffuser using the available data, if there exists, and to conduct the necessary tests in order to accomplish the satisfactory results.

In the present design the desired diffuser performance is achieved by

using screens in the diffuser and honeycombs at the exit and the inlet. Although this method, in general, is not favorable due to the fact that it results in a power loss, pressure loss was not a major concern in our design due to the avaliable pressurized air. As is well known, the resistance of a boundary layer regarding the separation process under an imposed adverse pressure gradient can be increased by decreasing the boundary layer thickness (this is one of the reasons that long diffusers (having a small divergence angle) are not favorable) for which the use of screens plays an important role. Due to the presence of screens and honeycombs, the flow takes place throughout all available upstream portion of the device avoiding (or delaying) the separation as well as reducing the axial turbulence and non-uniformities in the mean flow. Screens used in the diffuser design, (mesh size 30×30, gage 32, wire diameter $0.012''$, opening $0.0213''$, porosity $p = 0.410$, estimated loss coefficient $K = 2.52$)[11] were previously tested in a performance improvement study of a wide angle diffuser by Wo [60]. A honeycomb (Cyanamid, N5052, 3.1-1/8-0.001, $0.0625''$) is used at the exit of the diffuser to reduce the lateral velocities.

Flow non-uniformities are further smoothed out in the settling chamber using a combination of honeycomb and screens (mesh size 20×20, gage 28, wire

[11]The porosity p is defined as $p \simeq (1 - md)^2$ where m is the mesh size and d the wire diameter. The loss coefficient is defined as $K \simeq 0.51 \frac{1-p^2}{p^2}$.

diameter 0.016", opening 0.034", porosity $p = 0.462$, estimated loss coefficient $K = 1.88$). The honeycomb is installed upstream of the screens in the settling chamber as suggested by Loehrke and Nagib [33].

The settling chamber is connected to the contraction section in which non-uniformities and turbulence level are further reduced. This three-dimensional contraction has a contraction ratio of about 7 and has a cubic-shaped wall (matched in the middle) which is sugessted by Morel [39] as the one produces the lowest combination of inlet and exit wall pressure coefficients of all the curves indicating that a cubic-shaped nozzle is the most suitable one for the shortest non-separated contraction.

This contraction section is followed by a second 'small-scale' settling chamber in which we again use honeycomb (1/8, 3.0") and screen (mesh 20×20) to reduce non-uniformities further, and a cubic-shaped (matched in the middle) two-dimensional contraction having a contraction ratio of 9. The exit of the second contraction is connected to the test section having a cross-section of $9" \times 1"$. It is clear that the use of double-contraction method is a conservative choice in obtaining the smooth mean flow with a controllable turbulence level. It is also clear that for the future use of the wind tunnel test section dimensions can be easily altered by changing the design of the second nozzle.

High-quality plywood used in the wind tunnel construction is made water-proof in that the smooth surface properties is also achieved. The plywood skeleton of the contraction sections is carefully hand-shaped and its cubic-shaped walls are made with formica. The wind tunnel is bolted to the laboratory floor and is free of any appreciable vibration under the experimental conditions. The test sections used in the study are connected to the tunnel exit and they are fixed on a sturdy base bolted to the laboratory floor, on which the traversing mechanism for velocity measurements is also placed.

3.2.2 Enhancement Geometries

The details of three enhancement geometries considered in this study are presented in Figures 13, 14, and 15. All these test sections are fixed on a sturdy base bolted to the laboratory floor. The cases studied are Z_0, $Z_1 = \{D/H = 0.2, B/H = 0.25, L/H = 3.33\}$, $Z_2 = \{e/H = 0.025, a/H = 0.035, c/H = 0.015\}$, and $Z_3 = \{d/H = 0.015, b/H = 0.025, l/H = 9.33\}$. Six more geometric configurations of micro-cylinders studied are presented in Chapter 5 as our purpose here is to verify the scale-matched destabilization theory as an optimal heat-transfer enhancement method. For the geometry Z_0 the same test section for Z_1 and Z_3 are used with the augmentation hardware modifica-

tions are removed. For the geometries Z_0 ($Re < 9,000$), Z_1 ($Re < 8,000$), and Z_2 ($Re < 48,000$) thermal-hydraulic data are obtained in one of the low-speed wind tunnels (similar and bigger than the one we built) of the Department of Aeronautics and Astronautics at MIT. The ratio of the width of the channel W, to the channel height H is $W/H = 0.9$, which is considered sufficiently large that the results can be considered close to for an 'infinite' planar channel.

Eddy promoters are made out of brass rods, and are not heated. They effect the heat transfer only through flow modification. The micro-grooves are machined on the aluminum plates to high precision using a shaper. In the design of micro-cylinders plastic pieces of a certain height, depending on the desired b, and a width of $0.250''$ are glued on the aluminum surface first (at the edges and the middle) and then micro-cylinders are placed on these plastic surfaces. For micro-cylinders stainless steel piano wires are used and special care is given in order to avoid the vibration of micro-cylinders during the experiments.

3.3 Measurement Techniques

For the optimization studies of interest we require a set of Nu, f data for each Z_n. A single H is chosen, and the flow rate is varied to achieve

a desired range of Reynolds numbers. For each Reynolds number the pressure drop and fluid and wall temperatures are measured, thus allowing the $Nu(Re, Pr = 0.71; Z_n)$ and $f(Re; Z_n)$ curves to be constructed. Below we describe these measurement techniques and flow visualization techniques to gain a better understanding of destabilization of the eddy-promoter channel flows.

3.3.1 Flow Measurements

Velocity measurements in this study are performed by traversing a United Sensor pitot-static tube and a hot-wire probe across the channel height utilizing a vertical positioning system. These measurements allow for calculation of the flow rate and thus the flow Reynolds number. All velocity measurements to determine the flow rate are conducted in the smooth-entrance region of the test section (see Figures 13-15). Vertical level of the probe is determined by a precision potentiometer (it has a linearity of $\pm 0.25\%$ and is connected to a dc power supply) and a gear system connected to the vertical positioning system.

In pitot-static tube measurements the difference between the total and static pressure is measured using a MKS-398 Baratron pressure tranducer of 1-torr or 10-torr sensing head, depending on the magnitude of the difference, to which a MKS-270B high accuracy electronic display unit is connected. Mean

velocities are then obtained from this measured pressure difference using the incompressible Bernouilli's equation. MKS Baratron pressure transducers are high accuracy variable capacitance diaphragm pressure transducers and they have the capability of measuring 10^{-5}-10^{-6} torr with a 1-torr sensing head and 10^{-3}-10^{-4} torr for 100-torr sensing head.

A single sensor hot-wire probe (TSI model 1211-T1.5 used with a TSI model 1053 a constant temperature anemometer bridge and model 1051-2 monitor and power supply) is also used in velocity measurements. The hot wire system is calibrated against the pitot-static tube in the center of the tunnel exit. Special care is given to the calibration and operation temperature of the hot-wire.

The signals from the potentiometer and hot-wire or pitot-static tube are digitized and processed (e.g. integration of the profile to obtain the flow rate and Reynolds number) using a MetraByte DASH-8 analog-to-digital converter and an IBM PC/AT-339 personal computer. For data acquisition a software program written in BASIC is developed.

The pressure drop is also measured with the MKS-398 Baratron pressure transducers and it has been verified directly from the measurements that the time-averaged wall pressure vary linearly with x, consistent with fully developed

flow. This also illustrates that the length of the entrance region is long enough to obtain a hydraulically fully developed flow.

In Figure 16 we present a measured velocity profile $3d$ (d is the cylinder diameter, $d/H = 0.1$) behind a single cylinder placed in the center of a fully-developed plane Poiseuille flow ($x/H \simeq 60$). The hot-wire probe is used for the measurement. Although very low velocities are obtained at this Reynolds number, the experimental velocity measurements are in good agreement with numerical solution (Karniadakis [23]) indicating that the measurement techniques are verified and that the flow can be considered as an 'infinite' plane-channel flow. It is clear that this inflexional wake profile is created immediately downstream of the cylinder indicating that this steady flow corresponds to a plane Poiseuille flow locally perturbed in the vicinity of the cylinder. At high Reynolds numbers this steady flow becomes unstable as a result of this eddy-promoter perturbation (see Chapter 4).

3.3.2 Flow Visualizations

Flow visualization studies are performed only for the geometry Z_1 to gain better insight into the understanding of the stability characteristics of the eddy-promoter channel flows which play an important role in the analysis of

heat-transfer enhancement in laminar flows.

We first intended to conduct the flow visualizations in the wind tunnel using the smoke-wire visualization technique. However, low velocities associated with the Reynolds numbers of interest (about $0.25m/sec$) resulted in serious problems as a result of the gravitational effects. We then modified the test section using a 90° turn (pointing towards the ceiling of the laboratory) for which the 'unwanted' gravitational effects are eliminated. On the other hand, in this configuration it was not possible to obtain Reynolds numbers accurately by traversing the channel height with a pitot-static tube. Despite of all of these difficulties, we have conducted flow visualizations using the smoke-wire technique for the comparisons with other flow visualizations in the water channel as reported later.

For the purpose of the smoke-wire visualization technique, the interior of the channel, made of clear plexiglass, is painted with ultra-flat black paint to reduce light reflection except that we have a non-painted slide to illuminate the sheet of smoke with a strobe light, and a non-painted side wall for the photographic purposes, as shown in Figure 17. It is clear that lighting of the particular cross section of interest (in our case the middle cross section of the channel) from a direction normal to the viewing axis gives the best photographic

results (see Figure 17).

A Nichrome wire that has a diameter of 0.004″ is used at 45° angle to generate the required sheet of smoke. The use of angle is a requisite to wet the wire with smoke oil and also increased the number of generated smoke lines improving the quality of the visualizations. The wire is fixed on one side and a weight is hung on the other side to keep the wire under tension. The required voltage to produce a sheet of smoke is supplied using a dc power supply. The Lionel smoke oil, which has a long burning time providing a continuous smoke which is a requisite for a high quality visualization technique, is used in the experiments.

The photographs were taken in a dark environment using a strobe light to illuminate the sheet of smoke against the ultra-black painted side wall. The wire is wetted by the smoke oil injected from a syringe. Wetting of the wire and triggering of the power supply and camera were done manually. The resulting streakline patterns are photographed on a Kodak Tri-X 35*mm* 400 ASA black-white film with a Canon T70 35*mm* camera having a 75-300*mm* macro focusing zoom lens and an aperture setting of f11. The shutter is kept open during the photographing process and the strobe light was on for about 1/30 seconds. The results are presented in the next chapter.

Flow visualizations for the geometry Z_1 were also conducted in a water channel shown schematically in Figure 18. The water channel that has an aspect ratio of 11 was built by Greiner [17] in a previous study and the test section is modified for the geometry Z_1. This is a closed loop system that consists of a centrifugal steady-flow pump, a delivery pipe, a flow regulation valve, a flow rotameter, a test section containinig the channel geometry of interest and a temperature-controlled fluid reservoir. The further details on this facility is given by Greiner [17]. Distilled water is used as the working fluid in the experiments and flow rate is measured using calibrated rotameters.

For the flow visualizations water based rheoscopic fluid concentrations are used in the range of $0.03 - 0.05\%$. This rheoscopic fluid is produced by Kalliroscope Corporation (AQ-1000) and contains anisotropic flakes dispersed in water. Kalliroscope flakes are $6 \times 30 \times 0.07\ \mu m$ platelets made from guanine have a density of $1.62\ gr/cm^3$ (Matisse and Gorman [35]) and the flakes remain suspended in water for several days when used with the bacteriostatic stabilizer (ST-1000). They are easily visible even in very dilute concentrations due to their refractive index of 1.85. In the present study a sheet of Helium-Neon laser light is used to visualize a particular cross section of the flow in which the side wall effects are negligible. As reported by Matisse and Gorman [35] the effect of the flakes on the wave speeds in wavy flows is less that 0.1% indicating no problem

in studying the wavy flows of interest.

The resulting flow patterns as a function of Reynolds number are photographed on Kodak 6400 ASA (actually 3200 ASA pushed to 6400 ASA) $35mm$ black-white film with a CANON A-1 $35mm$ camera, 70-$210mm$ macro focusing lens and using a shutter speed of $1/15 - 1/30$, depending on the concentration, and an aperture setting of f4. The results of these flow visualization studies are presented in the next chapter.

3.3.3 Heat-Transfer Measurements

Heat-transfer measurements are made by dissipating a known uniform heat flux at the wall surface and measuring the resulting temperature difference between the wall temperature and mixed mean temperature of the fluid. Two different kind of electrical strip heaters are used in the present study; for the geometry Z_1 kapton insulated electrical strip heaters (Minco Inc. model HK10312), shown in Figure 19, are bonded on the top plexiglass wall (Figure 13), and for the geometries Z_2 and Z_3 the electrical strip heaters (custom-made by Thermal-Circuits Co. Salem, MA), shown in Figure 20, are bonded on the top/bottom aluminum walls (Figures 14-15). The required heat flux is produced by passing a known current through these resistance elements.

The wall and fluid bulk temperature measurements, that enables us to evaluate Nusselt number, are made using copper-constantan thermocouples. For the wall temperature measurements of the geometries Z_2 and Z_3 thermocouples are placed inside the wall as seen in Figures 14-15, whereas for the geometry Z_1 they were placed beneath the heaters (Figure 13).

We also note that the flow is allowed to become thermally fully developed in the streamwise direction x before any measurements are taken. All measurements are taken after a distance of roughly $65H$ from the inlet of the channel, and roughly $36H$ from the beginning of the heated region. The resulting entrance regions are sufficient to obtain hydraulically and thermally fully-developed flat-channel laminar flows for Reynolds numbers $Re < 800$, and fully-developed flat-channel turbulent flows for Reynolds numbers $Re > 5500$ (Schlichting [47]). The entrance length for the geometries Z_1, Z_2, and Z_3 are much shorter than for the smooth channel Z_0 as a result of destabilization as also found by Sparrow and Tao [48]. In addition to these theoretical considerations of entrance-length effects, it has also been verified directly from measurements that the wall temperature vary linearly with x, consistent with fully developed flow.

The thermocouple voltage signals are processed using an Omega ref-

erence junction (model CJ-T) and amplified using a MetraByte EXP-16 data acquisition board. The readings are then made using a MetraByte DASH-8 analog-to-digital converter and an IBM-PC/AT-339 personal computer. For data acquisition a software program written in BASIC is developed.

Chapter 4

Results of a Channel-Optimization Study of Heat Transfer

In this chapter the relationship between hydrodynamic stability and transport processes, the thermal-hydraulic data for the augmentation schemes of interest, and optimization results are presented. After reviewing the stability of plane-channel flows, the stability results are generalized for eddy-promoter channel flows based on our flow visualization studies. Results of a channel-optimization study for heat transfer based on the thermal-hydraulic data for several augmentation schemes are presented and the significant dissipation savings possible through *optimal* thermal-hydraulic design are demonstrated. The optimizing transport enhancement scheme is shown to proceed from macro-scale eddy promoters to micro-scale micro-groove/micro-cylinder roughness elements with increasing thermal load, thus verifying the validity of the scale-matched destabilization theory for optimal transport enhancement.

4.1 Hydrodynamic Stability and Transport Processes

In Chapter 2 it has been shown that the most effective heat-transfer enhancement technique to minimize the momentum-transport penalties in a thermal-hydraulic system is the one in which the *mixing* processes are intensified by the excitation of *hydrodynamic instabilities* in the region where the resistance to scalar transport is significant. The idea of flow destabilization is a new concept in heat-transfer enhancement and needs to be investigated in more detail (Ghaddar *et al.* [12]; Karniadakis [24]; Greiner [17]; Amon [1]).

The aim of the destabilization process is to excite the least stable modes which are found to be traveling waves in the flows of interest similar to those (Tollmien-Schlichting waves) found in smooth-channel flows (Ghaddar *et al.* [14]; Karniadakis, Mikić and Patera [25]). These modes are damped in subcritical flows and their growth rate increases with Reynolds number. The onset of natural oscillations, in which the least stable mode is no longer damped, occurs at a critical Reynolds number that depends on the perturbation method (e.g. eddy promoters, grooved channels etc.). It is at this Reynolds number that these flows become *effective* as regards transport enhancement and this effectiveness,

in general, continues for Reynolds numbers not much greater than the critical Reynolds number (it is clear that no destabilization scheme will be effective for all physically possible Reynolds numbers as naturally stable scales of motion becomes smaller and smaller with increasing Reynolds number).

In this section we briefly discuss the stability characteristics of plane Poiseuille flow and the eddy-promoter channel flows as they are related and we study the effect of destabilization on transport processes.

4.1.1 Linear Stability of Plane Poiseuille Flow

The linear stability analysis of plane Poiseuille flow is critical to a full understanding of the transition process and relevant to the stability of eddy-promoter channel flows. We therefore review the results briefly and then generalize the results to eddy-promoter channel flows based on our flow visualization studies and numerical studies performed by Karniadakis, Mikić and Patera [25].

The linear stability of the parabolic plane Poiseuille flow with respect to small disturbances is described by the Orr-Sommerfeld equation with Dirichlet boundary conditions (Drazin and Reid [9]; Kozlu and Patera [32]). The most general infinitesimal perturbation to the steady plane Poiseuille flow is a

superposition of traveling wave modes as

$$\mathbf{v}'(\mathbf{x},t) = \sum_{\alpha} \mathbf{v}'_{\alpha}(\mathbf{x},t) \tag{4.1}$$

where each mode has the form

$$\mathbf{v}'(\mathbf{x},t) = \exp(\sigma t)\ \mathrm{Real}\{\hat{\mathbf{v}}'(y)\ \exp[i(\alpha x - 2\pi\Omega t)]\}. \tag{4.2}$$

Here $\mathbf{v}'$ is the perturbation velocity, $\hat{\mathbf{v}}'$ the complex function of y, σ the non-dimensional[12] growth constant (hence, $\sigma > 0$ indicates a flow instability), α the non-dimensional wave number, Ω the non-dimensional frequency. Substituting this general form of the admissible modes into linearized equation of motion, we obtain the Orr-Sommerfeld equation subject to Dirichlet boundary conditions on both walls. The Orr-Sommerfeld equation leads to an eigenvalue problem with a characteristic equation of

$$\mathcal{F}(\alpha, \sigma, \Omega, ; Re) = 0. \tag{4.3}$$

A solution to the Orr-Sommerfeld equation by a Hermitian finite-element method is presented in Appendix A. The temporal stability analysis of plane Poiseuille flow gives the onset of instability at $Re_{cr} = 7{,}696$ and $\alpha_{cr} = 2.04$. As is well known, in most experiments the critical Reynolds number is found to be 1,300 although Re_{cr} can be larger than this value in quiet experiments. We then con-

[12]We again scale all length by H, and all velocities by V, the channel-average velocity.

clude that in the flows studied below, for $Re < 1,300$, in the absence of cylinders no channel instabilities or unsteadiness would occur.

4.1.2 Stability of Eddy-Promoter Channel Flows and Heat-Transfer Enhancement

We consider here the stability of eddy-promoter channel flows (the geometry Z_1) in which the plane Poiseuille flow is perturbed in the vicinity of the eddy promoters. This perturbation, depending on the flow Reynolds number, results in subcritical or supercritical flows; the latter plays an essential role in understanding the transport enhancement in laminar flows. Eddy promoters are chosen to be 'small' as we intend to minimize ϵ in equation (2.54).

Figure 21 shows the flow patterns obtained in flow visualization studies conducted in the water channel at $Re = 129$, whereas Figure 22 shows the streaklines obtained by the smoke-wire visualization of this stable steady flow. The flow is right to left. The isotherms ($Pr = 1.0$) of a two-dimensional numerical simulation in which flow field periodicity is imposed over the channel geometric periodicity L at $Re = 166.66$ is also shown in Figure 23 (Karniadakis, Mikić and Patera [25]). Both experimental and numerical results show that at this

Reynolds number, the flow is essentially parallel except in the small wake region behind the eddy promoter. The numerical studies of the linear stability analysis also illustrates that the eigenfunction is a traveling wave and closely resembles the Tollmien-Schlichting waves of smooth-channel Poiseuille flow. In particular, the eddy-promoter channel stability modes and smooth-channel stability modes are very similar in both form and frequency for this geometric configuration. These characteristics of eddy-promoter stability modes can be altered by changing the placement of eddy promoters as discussed by Karniadakis, Mikić and Patera [25].

Flow visualization studies clearly show that at this Reynolds number, the only heat-transfer mechanism is the molecular diffusion process as a result of mean-molecular temperature gradient as in the case of a laminar flow in the absence of eddy promoters. It thus follows that an increase in Nusselt number is not possible at this Reynolds number although the existence of eddy promoters unavoidably results in an increase in momentum-transport penalties. It is clear that the use of eddy promoters at this Reynolds number is not an *effective* solution for transport enhancement.

For Reynolds numbers greater than 200 the eddy-promoter steady flow becomes unstable in which the least stable modes are no longer damped. This is a

very important result as regards transport enhancement as the critical Reynolds number is decreased from $Re_{cr} = 1,300$ (linear theory predicts $Re_{cr} = 7,696$) to $Re_{cr} = 200$ resulting in drastic increases in Nusselt number for $Re > 200$. It is clear that this critical Reynolds number depends on the local variables such as the eddy-promoter diameter and local flow velocity (associated with the velocity profile) for the cylinder as well as the channel height H.

In Figures 24 and 25 we present the flow patterns for the supercritical eddy-promoter channel flows at $Re = 396$. All visualizations are performed for the seventh and eight cylinder after it has been verified directly from flow field that the visualization of successive periodicities shows the same structure. This is a steady-periodic flow and corresponds to nonlinear saturation of unstable Tollmien-Schlichting-like traveling waves. Note that the flow field is completely effected by the existence of eddy-promoters resulting in eddies on the order of channel height. Flow patterns clearly indicate that this is a two-wave flow (per geometric periodicity) with a wave number $\alpha = 2\pi n/L = 3.77$ $(n = 2)$ as also reported by Karniadakis [24] and is shown in Figure 26 for $Re = 400$.

The existence of finite-amplitude Tollmien-Schlichting waves in supercritical eddy-promoter channel flows subtantially alters the heat-transfer mechanism in these flows. The strong wavy structure associated with the 'small'

scale boundary layers on the top and bottom walls results in a Reynolds-flux dominated scalar transport in which high-heat-transfer-enhancement rates can be achieved. As a result of this 'universal' structure, it is shown by Karniadakis, Mikić and Patera [25] that the Reynolds analogy is valid in supercritical eddy-promoter flows. It is important to note that the similar flow structure on both walls indicates a similar heat-transfer enhancement rates on these surfaces as will be discussed in Chapter 5.

Figure 27 shows the flow patterns at $Re = 1132$ (Figure 28 shows the streakline patterns obtained by the smoke-wire visualization). As can be seen, the coherent structure of the wave pattern as in low-Reynolds-number flows does not exist at this Reynolds number which is close to the transition Reynolds number for smooth-channel flow. At this Reynolds number a 'better-mixed' core flow and a 'smaller-scale' near-wall structure compared to $Re = 396$ is obtained. This structure is very favorable as regards heat-transfer enhancement and results in drastic increases in Reynolds fluxes.

4.2 Thermal-Hydraulic Data

We plot in Figures 29 and 30 the $Nu(Re, Pr = 0.71; Z_n)$ and $f(Re; Z_n)$ curves for the geometries Z_0, Z_1, Z_2, Z_3 that will be used in optimization studies that follow. Since the friction factor data are obtained for finite aspect-ratio (9:1) channel, the friction factor data presented are further corrected by subtracting out the shear stress at the side walls to obtain the data for parallel plates.

We compare our flat-channel data for laminar flow with the exact solutions given in equations (2.15) and (2.16) (Kays and Crawford [27]), and for turbulent flow with existing previous smooth-channel correlations given in equations (2.19) and (2.21) (Kays and Crawford [27]; Hussain and Reynolds [20]). As can be seen from Figures 29 and 30, the heat-transfer data and friction factor data agree very well with the analytical solution and experimental correlations (the highest error in heat-transfer data is about 4% and in friction factor is about 2%). The present experimental heat-transfer data are also within the $\pm 6\%$ that is given as an error band for the Petukhov-Popov equation for $Pr = 0.71$ (Petukhov [44]). Note that we have extended the turbulent correlations for f and Nu down to transitional Reynolds number, $Re_{tr} = 1,300$, although it is clear that the correlations are strictly valid only at somewhat larger Re. The suspect region of the correlation is indicated by a dashed line.

We also supplement our data with numerical solutions for the geometry Z_1 (Karniadakis, Mikić and Patera [25]). The Nusselt number data obtained from $Pr = 1.0$ numerical solutions are corrected for the Prandtl number of interest here ($Pr = 0.71$) assuming a Prandtl number power law dependence on enhancement as given by Ghaddar *et al.* [15].

The experiments for the micro-grooved channel were, in fact, carried out for heating and micro-grooves, on *both* channel walls, as shown in Figure 14. To construct one-side heated/micro-grooved data from those experiments we assume that $Nu_{1-sided} \simeq Nu_{2-sided}$, and that $f_{1-sided} \simeq 1/2[f_{2-sided} + f(.; Z_0)]$, where $f(.; Z_0)$ refers to the friction factor in the smooth-channel geometry Z_0. This approximation appears reasonable for the small e/H considered here.

4.3 Optimization Results

We present here results of the optimization procedure developed in Chapter 2 based on the above thermal-hydraulic data. In Figure 31 we plot $\overline{\Psi}(\mu, Z_n)$ for a fixed $\Lambda = 800$ and Z_0, Z_1, Z_2, while in Figure 32 we plot $\overline{\Psi}_n^*$ for the geometries Z_0, Z_1, Z_2, Z_3. Figure 31 demonstrates how Figure 32 is constructed; the minimum of each Z_n curve in Figure 31 results in one point (at

$\Lambda = 800$) on Figure 32, as described by the optimization procedure outlined in Section 2.2.2.

We construct Figure 31 as follows: for each Reynolds number we calculate the non-dimensional inverse velocity μ for $\Lambda = 800$ from equation (2.24) and then we find the non-dimensional dissipation parameter $\overline{\Psi}$ using equation (2.28). It can be seen from Figure 31 that for a given geometry Z_n, operating at a non-optimal μ can significantly increase the dissipation; this clearly illustrates the importance of optimization even for the case of 'unenhanced' heat-transfer design. These findings are consistent with the results obtained in Section 2.1. Figure 31 also shows that heat-transfer enhancement leads to significant savings in dissipation in a properly designed heat-transfer system.

Figure 32 demonstrates that the scale-matched flow destabilization theory for transport enhancement proposed in Chapter 2 is, indeed, valid. Note that the actual smooth-channel minimization summarized in Figure 32 represents the minimum over both laminar and turbulent flows, with endpoint extrema taken into account as presented in Chapter 2. First, it is seen from Figure 32 that for very low Λ, Z_0 laminar flow performs the best. Note that dissipation depends on the thermal-hydraulic data as well as the dimensionless inverse velocity μ imposed by thermal constraint as seen from equation (2.28). For very low Λ,

a decrease in the ratio ($\frac{f}{Nu^3}$) associated with heat-transfer enhancement always dominated by the increase in $\frac{1}{\mu^3(1-\mu)^3}$ (see equation (2.28)) resulting in an increase in dissipation. On the other hand, the existence of eddy promoters does not result in an increase in Nusselt number at the *optimal* laminar Reynolds number to overcome laminar flow as discussed in Section 4.1.2. It thus follows that laminar flow is the best choice for very low Λ.

Second, as Λ increases, the macro-scale eddy promoters Z_1 becomes relatively more efficient than flat channels Z_0; this is due to the fact that the eddy promoters destabilize the flow and increase the Nusselt number, thereby decreasing dissipation by equation (2.28). The fact that ϵ in equation (2.54) is small for these flows despite significant destabilization is due to the fact that channel flows are only viscously (slightly) stable, as described in detail by Karniadakis [24]. At these thermal load parameters, for physically plausible Reynolds numbers, that satisfy the energy balance equation, the ratio $\frac{f}{Nu^3}$ becomes the dominating term over the $\frac{1}{\mu^3(1-\mu)^3}$ in equation (2.28).

It appears that laminar eddy promoters are never selected, as they are bettered at low Λ by laminar Z_0 flow, and at higher Λ by transitional eddy promoters. These observations are consistent with the behavior of the thermal-hydraulic data for eddy promoter flows; Based on our flow visualization studies

we expect no increase in Nusselt number for $Re < 200$ although dissipation increases as found in numerical solutions of Karniadakis, Mikić and Patera [25]. As we increase the Reynolds number, eddy promoters become *effective* in destabilizing this slightly stable channel flow, thereby increasing Nusselt number as seen in Figure 29. For transitional Reynolds numbers, the increase in Nusselt number reaches a maximum level when it is compared to smooth-channel flow at the same Reynolds numbers, and a 'premature' cylinder-drag crisis occurs. This thermal-hydraulic behavior of the transitional eddy-promoter flows results in significant reduction in momentum-transport penalties; it thus follows that these transitional flows are *optimal* for a broad range of the thermal load Λ. However, as we continue to increase thermal load (hence, corresponding Reynolds number), a non-linear saturation occurs for $Re \gg Re_{cr}$; the relative increase in Nusselt number decreases and non-analogous drag dominates as seen in Figure 29. It is at this point that eddy promoters are no longer efficient at destabilizing the flow at these Reynolds numbers as the flow in the core region is naturally is unstable. Note that for these thermal load parameters the use of eddy promoters results in an increase in dissipation as a result of dominating non-analagous drag as seen in Figure 32.

This analysis suggests that as Λ increases further, there is a need for a new enhancement scheme to destabilize the 'stable' part of the flow, the viscous

sublayer (Tennekes and Lumley [52]). As a result of a geometric matching between the sublayer scale and micro-groove and micro-cylinder dimensions, the micro-grooves and micro-cylinders become important at $Re \simeq 16,666$ and thus $\Lambda \simeq 1,400$. The micro-disturbances become important at $u_* e(b)/\nu \simeq 20 - 30$ consistent with past studies on the effect of roughness in transport processes. Here u_* is the friction velocity, which is defined as $u_* = \sqrt{\tau/\rho}$, where τ_w is the shear stress at the wall. Note that the savings due to flow destabilization at low Λ appear to be larger than those at high Λ reflecting the intrinsic instability of turbulent flows. It is important to note that micro-grooves perform efficiently for a wider range of thermal load than micro-cylinders due to the fact that the matching of geometric perturbation and sublayer scale is less sensitive to Reynolds number. Details of the physics of micro-cylinder and micro-groove destabilized turbulent flows will be presented in Chapter 5.

There is a great deal of information in Figure 32 as regards the scaling of minimum dissipation with thermal load. For instance, if Λ is increased from 10^2 to 10^3 (due to, say, a decrease in the allowable δT by a factor of 10), the dimensional minimum dissipation $\{\Delta P\, V\, H\}^* \sim \overline{\Psi}^*$ increases by roughly a factor of 10^3; this illustrates the rather severe penalty associated with stringent thermal load requirements. If we assume that $Nu \sim Re^{\beta}$, it follows from Reynolds' analogy argument and upper bound result (Section 2.3.3) that the minimum

dissipation $\overline{\Psi}^*$ scales as $\overline{\Psi}^* \sim \Lambda^{5-2\beta}$, which is consistent with the data of Figure 32 for a (physically plausible) value of β slightly less than unity.

Chapter 5

Turbulent Heat-Transfer Augmentation

The theory of scale-matched flow destabilization for optimal transport enhancement has been succesfully applied to laminar and turbulent flows in the previous chapters. Intensification of turbulent heat transfer plays a significant role in technological applications since most engineering systems operate under the turbulent-flow conditions. In this chapter turbulent heat-transfer enhancement strategies based on the near-wall mixing processes induced in the viscous sublayer through appropriate wall and near-wall streamwise-periodic disturbances are studied. These hardware modifications in the viscous sublayer correspond to the addition of a) two-dimensional periodic micro-grooves on the wall, and b) two-dimensional periodic micro-cylinders in the immediate vicinity of the wall, respectively. It has been shown in the previous chapter that the excitation of local instabilities in the viscous sublayer by the existence of these micro-disturbances induces *favorable* heat transport augmentation with respect to smooth-wall case.

Work to date on turbulent heat-transfer augmentation has focused on the enhancement of heat-transfer coefficient and the associated unavoidable increase in the friction factor with respect to smooth-channel flow. Increases in the heat-transfer coefficient as high as 400% were achieved with accompanying changes in the friction factor rising as much as 58 times over the smooth wall case at the same Reynolds number (Bergles [5]). However, in these studies effect of destabilization of the viscous sublayer on the thermal-hydraulic behavior of these flows is not adequately explained in terms of governing variables, such as the placement and spacing of hardware modifications as a function of roughness Reynolds number. As a result no general results as regards the optimal heat-transfer design for turbulent flows are available.

The aim of the present chapter is to investigate heat and momentum transfer in turbulent flows under the presence of controlled wall and near-wall disturbances. To gain a better understanding of scalar transport phenomena in turbulent flows, a parametric study for micro-cylinders is conducted by changing the distance between successive micro-cylinders, the diameter of micro-cylinders, and the distance of micro-cylinders from the heated wall. The primary purpose of the current chapter is to present a basic understanding of the underlying turbulent physical transport phenomena which permits choice of proper enhancement scheme for turbulent flows at a given thermal load.

In Section 5.1 we briefly discuss the existing work on turbulent transport phenomena. In Section 5.2 we present the geometric characteristics of the micro-disturbances employed. In Section 5.3 we present and analyze the thermal-hydraulic data for the turbulent augmentation schemes of interest. In Section 5.4 we compare micro-groove and micro-cylinder equipped turbulent-channel flows with respect to minimum-dissipation heat removal.

5.1 Background

There are a large number of studies on turbulent heat-transfer augmentation employing the intensification of the near-wall mixing processes induced in the viscous sublayer through controllable wall and near-wall streamwise-periodic disturbances. Although they are geometrically different, in all systems the common physical phenomenon is a change in the structure of the viscous sublayer that results in a *favorable* increase of scalar transport rates. Below we cite the most relevant work on turbulent heat-transfer augmentation.

Brouillette *et al.* [6] studied the thermal-hydraulic behavior of internally grooved tubes. The 60-degree V-shape grooves were machined on the inner surface of tubes. The effects of groove-height and the distance between the

grooves on heat transfer and pressure drop were studied. The measured values of heat-transfer coefficients and friction factors were 10-100% and 15-400% higher than those of smooth channels for $Pr \simeq 7$, respectively. They found that the heat-transfer coefficient is greatly influenced by the groove depth rather than the groove spacing.

Fortescue and Hall [10] conducted experiments on the longitudinal-finned and transverse-finned fuel elements placed in a bigger circular smooth channel for the design of the Calder Hall nuclear reactor. The fluid was a gas with a Prandtl number of 0.71. Their heat-transfer and pressure-drop measurements for transverse-finned fuel rods indicated that fins should be closely placed to achieve a better reduction in momentum-transport penalties. They also found that the increase in the heat-transfer coefficient was higher than the increase in the friction factor for the closely spaced grooves.

Dipprey and Sabersky [8] experimentally investigated the heat and momentum transfer in smooth and rough tubes at several Prandtl numbers using water as the working fluid. Their three-dimensional roughness was formed by sand grains. Increases in Nusselt number due to roughness of as high as 270% were obtained. These increases were, in general, associated with larger increases in the friction factor except that the increase in the heat-transfer coefficient was

more than the increase in the friction factor at the high Prandtl numbers. Their data mostly covered the 'fully-rough' flow regime.

Zajic [61] reported a study of turbulent heat-transfer augmentation from roughened surfaces. The rough surfaces were obtained by a metric profile thread of 60-degree angle with a lead of $1.25mm$ and a depth of $0.06mm$ on the inner surface of the tube and a depth of $0.10mm$ on the outer surface of the tube. He conducted the measurements in both circular and annular channels. For the inside roughened tube in the 'fully-rough' flow regime they obtained a 25% increase in the heat-transfer coefficient and for small Reynolds numbers ($Re \simeq 10,000 - 20,000$) this increase was more than the increase in the friction factor. He then extended his study to the case of surface boiling phenomena at high-heat-flux rates.

Han, Glicksman and Rohsenow [18] investigated the heat transfer and friction characteristics of the rib-roughened surfaces in an air channel. They studied the effects of rib shape, angle of attack and pitch to height ratio on friction factor and heat transfer. A general correlation using the surface roughness parameters was developed to predict the thermal-hydraulic behavior of these flows. Ribs at a 45-degree angle of attack were found to have a favorable heat transfer and friction factor behavior compared to ribs at 90-degree angle of at-

tack and to sand grain roughness.

Sparrow and Tao [48] performed a study in a flat channel having streamwise-periodic cylinders attached to the wall. They obtained highly detailed axial distributions of the local mass-transfer coefficient using naphthalene sublimation. They studied the effect of the pitch-to-height ratio of the disturbance elements and the effect of the ratio of the disturbance height to the duct height on thermal-hydraulic data as well as the effect of these micro-disturbances on the opposite smooth wall. Air was the working fluid. They obtained enhancements in the average Sherwood number as high as 90% associated with larger increases in the friction factor. They also correlated the heat-transfer and friction-factor data using the surface roughness parameters.

Kawaguchi, Suzuki and Sato [26] studied the heat-transfer phenomena in a turbulent boundary layer having a cylinder array located near the wall. Measurements of the heat-transfer coefficient were performed to determine the optimum value for the cylinder pitch and spacing between the cylinders and the flat plate surface to enhance the flat plate heat transfer. They found that the performance of the cylinders in improving heat-transfer enhancement is better when they are placed closer to the wall indicating that a critical scaling of micro-disturbances in order to excite the local instabilities in the viscous sublayer is

essential.

Most of the work above were conducted on the 'fully-rough' flow regime, and they typically presented the performance of heat-transfer augmentation as a ratio between enhanced and base case heat-transfer coefficients, together with corresponding changes in the friction factor, all at the same Reynolds number. On the other hand, the idea of generalizing the previous results covering both 'transitional' and 'fully-developed' flow regimes was not adequate (Norris [41]) without an understanding the underlying physical phenomena of turbulent heat-transfer enhancement (it is clear that the turbulent transport phenomena in augmented transport systems is different in the 'transitional' flow regime than in the 'fully-rough' flow regime and that a Prandtl number dependence of augmentation rates is obvious). As a result no general procedures have been presented for selecting an *effective* augmentation scheme at a given thermal load.

5.2 Experimental Apparatus

We shall consider two heat-transfer augmentation schemes of (a) streamwise-periodic micro-grooves, and (b) streamwise-periodic micro-cylinders in a flat channel as shown schematically in Figures 7b and 7c. We again denote the

Geometry	d/H	b/H	l/H	Micro-cylinder equipped wall	Heated wall
Z_3^1	0.015	0.025	9.33	bottom	bottom
Z_3^2	0.015	0.025	18.66	bottom	bottom
Z_3^3	0.015	0.025	26.00	bottom	bottom
Z_3^4	0.032	0.060	4.13	bottom	bottom
Z_3^5	0.015	0.025	26.00	bottom+top	bottom
Z_3^6	0.015	0.025	26.00	top	bottom
Z_3^7	0.049	0.059	8.65	top	bottom

Table 5.1: Characteristics of micro-cylinder geometries

base geometry as Z_0, and we consider one micro-groove geometry (denoted by $Z_2 = \{e/H = 0.025, a/H = 0.035, c/H = 0.015\}$) and seven different micro-cylinder geometries (denoted by Z_3^m, $m = 1, ..., 7$) as given in Table 5.1. The geometries Z_2 and Z_3^1 are previously studied as regards the optimal thermal-hydraulic design in Chapter 4. We perform the experiments in the channel as shown schematically in Figures 14 and 15. Measurements techiques employed are also the same as presented in Chapter 3.

For the augmentation schemes of interest we require a set of Nu, f for each Z_n. Reynolds number, Nusselt number, and friction factor are defined in

the conventional way as $Re = \frac{VD_H}{\nu}$, $Nu = \frac{hD_H}{k}$ and $f = \frac{\Delta P}{L}\frac{D_H}{4}\frac{2}{\rho V^2}$, respectively. Here D_H is the hydraulic diameter for the channel ($D_H = \frac{4WH}{2(W+H)}$ see Figures 7b and 7c), $\frac{\Delta P}{L}$ pressure gradient, ρ the fluid density, V the average velocity; h is the heat-transfer coefficient , k the fluid thermal conductivity. Flow rate is varied to achieve a range of Reynolds numbers. For each Reynolds number the pressure drop and wall and fluid temperatures are measured, thus allowing the evaluation of $Nu(Re, Pr = 0.71; Z_n)$ and $f(Re; Z_n)$.

5.3 Results and Discussion

We plot in Figures 33 and 34 the $Nu(Re, Pr = 0.71; Z_n)$ and $f(Re; Z_n)$ curves for the flat-channel flow and augmentation schemes of interest. For micro-groove equipped flat-channel flows (Z_2), micro-grooves have negligible effect on transport augmentation for the roughness Reynolds numbers smaller than about 10 as seen in Figures 33 and 34. We define the roughness Reynolds number as $Re_k = u_* e/\nu$, where u_* is the friction velocity ($u_* = \sqrt{\tau_w/\rho}$, where τ_w is the shear stress at the wall) and ν the kinematic viscosity of the fluid. For τ_w we use the value for smooth-channel flow at the same Reynolds number; this is a lower bound for the roughness Reynolds number and is a reasonable assumption (particularly for micro-cylinders) since we do not measure the wall shear

stress directly. When we increase the Reynolds number (or roughness Reynolds number) the effect of micro-grooves become significant on scalar transport phenomena, as they geometrically scale with the 'stable ' part of the flow, the viscous sublayer. These observations are consistent with past studies on the effect of roughness in the transport processes (Tennekes and Lumley [52]).

We now plot the modified j-factor (defined as $j = \frac{f}{2}\frac{Re}{Nu}Pr^{\frac{1}{3}}$ using equation (2.53) with $\gamma = Pr^{-\frac{1}{3}}$ (Colburn [7])) as a function of roughness Reynolds number, as shown in Figure 35. For flows in which analogous heat and momentum transfer are preserved, the modified Colburn analogy [7] factor has a value of 1 (see Section 2.3.3). Figure 35 shows that for micro-grooves a roughly equal relative increase in heat and momentum transfer is obtained for $Re_k \leq 80$. As we continue to increase the Reynolds number ($Re_k \geq 80$), the micro-grooves cease to match the sublayer scale, and the non-analogous form drag starts dominating in the ensuing 'fully-rough' regime. Thus, the relative increase in pressure drop is larger than the increase in heat transfer; this reconfirms the fact that the roughness Reynolds number is the critical parameter parameter governing the flow (Townes and Sabersky [55]), and that there is an optimal placement of micro-disturbances which requires a matching of geometric perturbation with the viscous-sublayer scale.

For micro-cylinders, we obtain the following results from comparisons of four different data sets ($Z_3^1 - Z_3^4$). First, as seen in Figures 33 and 34, l/d has a small effect for the values b and d studied until $l/d = 18.66$. It is observed that the results of $l/d = 9.33$ and $l/d = 18.66$ are almost the same, whereas for $l/d = 26.00$ we see a decrease in heat and momentum transfer compared to the previous case. This is consistent with the expected trend of diminished transport augmentation as $l/d \to \infty$. As we decrease the distance between the micro-cylinders and increase the diameter of micro-cylinders, an increase in the transport rates is observed.

Referring to our plot of the modified j-factor as a function of the roughness Reynolds number[13] in Figure 35, in which we see that all the data similar behavior, and that the effectiveness of micro-cylinders (in enhancing heat transfer without generating an unduly high friction loss) is increased when placed inside $y^+ = \frac{u_* y}{\nu} \simeq 20$. This is the reason that Z_3^4 is not favorable compared to other geometric configurations, Z_3^1 and Z_3^2, since the micro-cylinders in the former case were outside the sublayer for the whole range of tested Reynolds numbers, thereby contributing to form drag and non-analogous dissipation.

These results can also be seen from Figure 36 in which we plot the

[13]For micro-cylinders we define the roughness Reynold number based on b, $Re_k = \frac{u_* b}{\nu}$.

Nusselt number enhancement ($E = Nu_{enhanced}/Nu_{smooth}$) as a function of the roughness Reynolds number. Figure 36 also shows that the favorable heat-transfer enhancement performance increases with increasing d/H and $(l/H)^{-1}$; however, a geometric matching for effective destabilization is still required.

The internal micro-disturbances cause an increase in scalar transport rates through local effects in the viscous sublayer. The external disturbances from the outer layer are still required to drive the instabilities in the sublayer and hence maintain the turbulent nature of the flow (Mikić [37]). The response of the viscous sublayer to both these disturbances is manifested through the following flow features. First is the apperance of a destabilized wavy structure of the viscous sublayer through a 'vortex shedding' phenomenon induced by micro-disturbances. This could be interpreted as the scaled-down version of the eddy-promoter caused instability in laminar flows to the viscous sublayer scale although the structure of the viscous sublayer in the presence of micro-disturbances is very complicated and needs to be investigated in detail (Grass [16], Bandyopadhyay [2], Tani [50]). Second is the existence of bursting events (perhaps secondary instabilities) whose frequency is controlled by wall-flow parameters. Lastly, there will be a relatively small gross flow displacement (that is, a redistribution of the mean velocity profile caused by the modified near-wall momentum transport characteristics, and mainly depends on the cylinder

diameter).

The wavy structure of the viscous sublayer due to the 'vortex shedding' phenomenon requires a cylinder Reynolds number of roughly 40, indicating a dependence of this phenomenon on the micro-cylinder diameter d, and the local velocity V_{cyl} (which is a function of l, d and flow Reynolds number). This wavy structure is responsible for enhancing scalar transport rates and also increasing the bursting frequency. Achievement of favorable heat-transfer augmentation by matching the geometric scale of the augmentation hardware modification to that of the viscous sublayer reconfirms the theory of scale-matched destabilization for optimal scalar transport enhancement described in the previous chapters: micro-cylinders placed inside the viscous sublayer achieve the requisite destabilization in the 'laminar-like' wall region while simultaneously controlling the increase of non-analogous drag.

To show the effect of micro-disturbances on the opposite from the heated wall, we conducted three different sets of experiments. Thermal-hydraulic data of these tests are presented in Figures 37 and 38. First, for the geometry Z_3^3 we use micro-cylinders at both the heated bottom wall and unheated top wall (geometry Z_3^5). Figure 37 illustrates that there is no change in the heat-transfer coefficient compared to the geometry Z_3^3, indicating that although micro-disturbances

effect the flow locally, they have no effect on the core flow, and hence no effect on the opposite wall (it is clear that an increase in the friction factor is inevitable). To support this conjecture, we have also conducted an experiment with the geometry Z_3^6 in which only the top unheated wall is equipped with micro-cylinders, whereas the bottom heated wall is smooth. As can be seen from Figure 37, the experimental heat-transfer data, strenghtening the above explanation. This results are consistent with findings of Sparrow and Tao [48].

When we considerably increased the opposite-wall micro-cylinder diameter (about three times compared to Z_3^5) in geometry Z_3^7, we see no effect at higher Reynolds numbers. However, for low Reynolds numbers an increase in heat transfer up to 10% compared to the flat-channel flow is observed. This is due to the fact that an increase in micro-cylinder diameter causes an asymmetry in the flow which is responsible for altering the transport characteristics of smooth wall for low Reynolds numbers. If we continue to increase the cylinder diameter to the order of channel height, it is clear that transport rates for both walls will be effected by the existence of wavy unsteady secondary flows as in the case of eddy-promoter channel flows seen in Figures 21-28; similar flow structure on both walls associated with a wavy core flow is the reason for achieving the similar enhancement rates for these surfaces indicating that an effect on the core-flow structure by the existence of disturbance elements is re-

quired to enhance the heat transfer simultaneously on both walls. This again confirms the scale-matched hypothesis for optimal transport enhancement. The extend to which micro-cylinder high-Reynolds-number and macro-cylinder low-Reynolds-number flows are 'self similar' as regards scalar transport remains to be determined.

5.4 Minimum-Dissipation Heat Removal Considerations

In Figure 39 we plot the nondimensional minimum-dissipation parameter $\overline{\Psi}_n^*$ as a function of the thermal load Λ for the geometries Z_2, Z_3^1, Z_3^3, Z_3^4. Figure 39 is constructed using the procedure outlined in Figure 32. Figure 39 illustrates the significant (almost order-of-magnitude) savings in dissipation compared to smooth-channel flows as a result of properly designed micro-disturbances. It is important to note that micro-grooves perform efficiently for a wider range thermal load than micro-cylinders due to the fact that matching of geometric perturbation and sublayer scale is less sensitive to Reynolds number. For micro-cylinders placed outside $y^+ \simeq 20$, the relative savings tend to decrease strongly (see Figure 35), implying a significant Reynolds number dependence on

position and size of near-wall micro-disturbances. This analysis indicates that a careful design of micro-cylinder geometry is essential in order to match the geometric scale of micro-disturbances with the viscous sublayer scale and hence to achieve the desired dissipation savings for a given thermal load.

Chapter 6

Conclusions

The optimal heat-transfer design in a plane channel is considered. The optimization problem is stated as the one that corresponds to maintaining a fixed thermal load while minimizing either one of the following hydrodynamic penalties: shear stress, pressure drop or viscous dissipation (pumping power). The main conclusions of this optimal thermal-hydraulic-design study can be briefly summarized as follows.

The optimization problem is reduced to a 'universal' form by introducing a nondimensionalization in which only fixed constraint variables are used to scale length, time and temperature. The minimum-dissipation optimization problem is solved in a formal sense for a smooth-channel flow to determine the required system design parameters (Reynolds number and channel height) in order to minimize the pumping power at a given thermal load. Results demonstrate that the significant dissipation (or pressure drop/shear stress) savings are

possible through the optimal design procedure even for the unenhanced transport systems. It is shown that results can be easily extended to plane-channel flows that have different thermal constraints.

The thermodynamic analysis of the optimal heat-transfer design illustrates that the minimum-dissipation-optimization problem is equivalent to the minimum-entropy-generation-optimization problem under the assumption of $\overline{\Delta T}/T \ll 1$.

The results of the minimum-dissipation optimization problem in a flat channel, via Reynolds' analogy, leads to the scale-matched flow destabilization theory for optimal transport enhancement; the destabilization of the flow at naturally stable scales of motion is required to achieve the optimal heat-transfer enhancement in which momentum-transport penalties are minimized.

The theory of scale-matched flow destabilization for optimal transport is applied by considering the following enhancement schemes: (a) laminar heat-transfer enhancement by macro-scale destabilization of laminar channel flows by eddy promoters, and (b) turbulent heat-transfer enhancement by micro-scale destabilization of the viscous sublayer by micro-grooves and micro-cylinders. A sample optimization study of heat transfer in a channel based on the experimental data of these augmentation techniques verifies the theory of scale-

matched destabilization, and quantifies that the significant dissipation savings (almost order-of-magnitude) are possible through optimal heat-transfer design in augmented transport systems. The optimizing tranport enhancement scheme is shown to proceed from macro-scale eddy promoters to micro-scale micro-groove/micro-cylinder roughness elements with increasing thermal load.

Hydrodynamic stability analysis of eddy promoter channel flows based on flow visualization studies demonstrates that Tollmien-Schlichting waves are activated at relatively low Reynolds number via a shear layer destabilization mechanism which is responsible for intensifying the heat-transfer rates in laminar flows and hence resulting in a reduction in momentum-transport penalties.

A parametric study conducted for micro-scale destabilized turbulent flow using micro-cylinders shows that the optimal placement of micro-disturbances requires a matching of geometric perturbation and the viscous sublayer scale, implying a dependence of the optimal position and size on Reynolds number; the favorable performance of micro-cylinder-equipped channel flows is achieved for micro-cylinders placed inside $y^+ \simeq 20$; for micro-grooved channel flows favorable augmentation is obtained for a wider range of Reynolds number, however optimal enhancement still requires a matching of geometric pertubation with sublayer scale. It is also shown that micro-disturbances effect the flow locally in

the viscous sublayer; they have no effect on the core flow, and hence no effect on scalar transport behavior of the opposite wall.

Appendix A

Solution to the Orr-Sommerfeld Equation by a Hermitian Finite-Element Method

An analysis of the linear stability of a flow is critical to a full understanding of the transition process that leads to turbulent flow. Parallel shear flows are of particular interest not only as regards the subtlety of the stability mechanism, but also in that appear in a broad range of engineering applications as demonstrated in the previous chapters. The linear stability of the parabolic plane Poiseuille flow profile with respect to small disturbances is described by the Orr-Sommerfeld equation with Dirichlet boundary conditions. Although the singular nature of plane Poiseuille flow stability renders analytical progress difficult (Drazin and Reid [9]), numerous numerical methods have been applied with success to this problem (Drazin and Reid [9]).

Particular relevant to the current solution method are the matrix-eigenvalue methods based on a finite-difference (Thomas [54]; Gary and Helgason [11]) and spectral spatial discretizations (Orszag [42]). It is clear that methods developed for plane Poiseuille flow are directly applicable to other parallel plane flows, such as Couette flow, and with minor modification, pipe Poiseuille flow as well. The linear stability of falling liquid film is also characterized by a parabolic profile and the Orr-Sommerfeld equation, however, the boundary conditions are significantly more complicated at the free surface. Extension of the present method to these flows is given by Kozlu and Patera [32]. The essential feature of the present approach for plane Poiseuille flow is the choice of Hermitian finite elements for derivative boundary conditions (Strang [49]). Although previous investigators achieved accurate results with other methods, it is our claim that the generality, rigor, and efficiency provided by the Hermitian formulation all allow for easier extension to more complex physics, such as the analysis of free-surface flows, two-fluid layers or condensate flows (Kozlu and Patera [32]).

A.1 The Hydrodynamic Stability Problem

A.1.1 Linearization

We consider two-dimensional, incompressible plane Poiseuille flow. The flow field is described by the velocity $(u, v) = (u(x, y, t),\ v(x, y, t))$, and pressure $p(x, y, t)$, where u and v are the streamwise (x) velocity, and the cross-stream (y) velocity, and t is time. The flow domain is defined by a cross-stream length scale H (channel height), and an unbounded (ultimately assumed periodic) spatial scale domain in x. The fluid is assumed to be characterized by constant properties given by the density ρ, the dynamic viscosity μ, and the kinematic viscosity ν. The basic parallel flow solution is given by $(\overline{U} = U_{cl}\ \left[4\,\frac{y}{H} - 4\,(\frac{y}{H})^2\right],\ \overline{V} = 0.0,\ \frac{d\overline{P}}{dx} = const,\ U_{cl} = -\frac{H^2}{8\mu}\ \frac{d\overline{P}}{dx})$. We now scale all length by H, all velocity by U_{cl}, all time by $\frac{H}{U_{cl}}$, and define Reynolds number as $Re = \frac{U_{cl}H}{\nu}$. We then write (henceforth all variables are nondimensionalized)

$$u = \overline{U} + u', \quad v = v' \quad p = \overline{P} + p', \tag{A.1}$$

insert (A.1) into the Navier-Stokes and continuity equations, and linearize, we arrive at the equations governing the behavior of small disturbances

$$\frac{\partial u'}{\partial t} + \overline{U}\frac{\partial u'}{\partial x} + v'\frac{\partial \overline{U}}{\partial y} = -\frac{\partial p'}{\partial x} + \frac{1}{Re}(\frac{\partial^2 u'}{\partial x^2} + \frac{\partial^2 u'}{\partial y^2}), \tag{A.2}$$

$$\frac{\partial v'}{\partial t} + \overline{U}\frac{\partial v'}{\partial x} = -\frac{\partial p'}{\partial y} + \frac{1}{Re}(\frac{\partial^2 v'}{\partial x^2} + \frac{\partial^2 v'}{\partial y^2}), \tag{A.3}$$

$$\frac{\partial u'}{\partial x} + \frac{\partial v'}{\partial y} = 0, \tag{A.4}$$

subject to the following boundary conditions

$$u' = 0, \quad v' = 0, \quad \text{at} \quad y = 0 \quad \text{and} \quad y = 1. \tag{A.5}$$

The boundary conditions given by equation (A.5) correspond to no-slip (zero velocity) on the rigid wall.

A.1.2 The Orr-Sommerfeld Operator

As the coefficients in equations (A.2-A.4) depend only on y, linearity, homogeneity, and separability allow us to consider solutions of the simple form

$$u' = \hat{u}(y) \exp[i(\alpha x - \omega t)], \tag{A.6}$$

$$v' = \hat{v}(y) \exp[i(\alpha x - \omega t)], \tag{A.7}$$

$$p' = \hat{p}(y) \exp[i(\alpha x - \omega t)], \tag{A.8}$$

where α is the non-dimensional wavenumber of the disturbance and ω is the non-dimensional frequency of the disturbance. We only consider two-dimensional disturbances since Squire's theorem (Drazin and Reid [9]) holds for plane Poiseuille

flow. Substituting the above expressions into the linearized equations of motion and performing the usual manipulations we obtain the Orr-Sommerfeld equation

$$\left(D^2 - \alpha^2\right)^2 \hat{v} = iRe \left((\alpha\overline{U} - \omega)(D^2 - \alpha^2) - \alpha D^2\overline{U}\right) \hat{v}, \qquad \text{(A.9)}$$

where $D = d/dy$.

The Orr-Sommerfeld equation, in terms of the $\hat{v}$ variable, is subject to the following boundary conditions

$$\hat{v} = 0 \quad \text{and} \quad D\hat{v} = 0 \quad \text{at} \quad y = 0 \quad \text{and} \quad y = 1. \qquad \text{(A.10)}$$

The Orr-Sommerfeld equation subject to the stated boundary conditions (equation (A.10)) for plane Poiseuille leads to an eigenvalue problem with a characteristic equation of

$$\mathcal{F}(\alpha, \omega;\, Re) = 0. \qquad \text{(A.11)}$$

In the following we investigate the temporal stability (search $\omega = w_r + iw_i$ for a given real α) of plane Poiseuille flow in a channel based on the solution of the Orr-Sommerfeld equation by the Hermitian finite element method.

A.2 Finite-Element Formulation of the Orr- Sommerfeld Equation

A.2.1 Weak Form

The weak form for the Orr-Sommerfeld equation and boundary conditions (equations (A.9) and (A.10)) is:

Find $(\hat{v},\ \omega) \in (X,\ C)$ such that

$$\int_0^1 [D^2\hat{v}\, D^2\phi + (2\alpha^2 + iRe\alpha\overline{U})D\hat{v}\, D\phi + (\alpha^4 + iRe\alpha^3\overline{U} + iRe\alpha D^2\overline{U})\,\hat{v}\phi + iRe\, D\overline{U}\, D\hat{v}\phi]\, dy = iRe\omega \int_0^1 [\alpha^2\hat{v}\phi + D\hat{v}\, D\phi]\, dy \quad \forall \phi \in X \quad \text{(A.12)}$$

where X is given by

$$X = \{\hat{v} \in \mathcal{H}^2(\Lambda =]0,1[);\ \hat{v}(0) = D\hat{v}(0) = \hat{v}(1) = D\hat{v}(1) = 0\}, \quad \text{(A.13)}$$

A.2.2 The Finite-Element Method

We first start breaking up the domain $\Lambda =]0,1[$ into the subdomains (elements)

$$\Lambda = \bigcup_{k=1}^{K} \Lambda_k, \tag{A.14}$$

where we choose the elements to be equal length of $| \Lambda_k | = h$ and denote the number of elements by K. The space of approximation of the solution $\hat{v}$ is then taken to be a subspace X_h of X

$$X_h = \{\hat{v}_h \in \mathcal{H}^2(\Lambda),\ \hat{v}_h |_{\Lambda_k} \in \mathcal{P}_3(\Lambda_k)\} \cap X. \tag{A.15}$$

The finite element method discretization corresponds to numerical quadrature of the variational form (equation (A.12)) restricted to the subspace X_h. Our problem then becomes: find $(\hat{v}_h,\ \omega_h) \in X_h$ such that

$$\sum_{k=1}^{K} \sum_{m=0}^{M} \{\rho_m \frac{h}{2} (D^2\hat{v}_h(\xi_{m,k})D^2\phi_h(\xi_{m,k}) + (2\alpha^2 + iRe\alpha\overline{U}(\xi_{m,k}))D\hat{v}_h(\xi_{m,k})D\phi_h(\xi_{m,k}) +$$
$$\{(\alpha^4 + iRe\alpha^3\overline{U}(\xi_{m,k}) + iRe\alpha D^2\overline{U}(\xi_{m,k}))\hat{v}_h(\xi_{m,k}) + iRe\, D\overline{U}(\xi_{m,k})D\hat{v}_h(\xi_{m,k})\}\phi_h(\xi_{m,k}))\} =$$
$$iRe\omega_h \sum_{k=1}^{K} \sum_{m=0}^{M} \rho_m \frac{h}{2} \left[\alpha^2\hat{v}_h(\xi_{m,k})\phi_h(\xi_{m,k}) + D\hat{v}_h(\xi_{m,k})D\phi_h(\xi_{m,k})\right]. \tag{A.16}$$

Here $\xi_{m,k} = h(k-1) + (\xi_m + 1)\frac{h}{2}$, $0 \le m \le M$, $1 \le k \le K$ are the locations of the local quadrature coordinates $\{m,k\}$, and ξ_m, ρ_m $0 \le m \le M$ are the Gauss-Legendre quadrature points and weights, respectively. We require M unequally spaced points to integrate exactly a polynomial of order of $(2M-1)$ (Bathe [3]).

In order to implement the finite element method it is necessary to choose a basis for the polynomial space X_h. We choose Hermite cubics to represent $\hat{v}_h, \phi_h \in X_h$

$$\hat{v}_h(y) = \bigcup_{k=1}^{K} \sum_{j=0}^{N=3} \hat{v}_j^k h_j(r), \tag{A.17}$$

$$\phi_h(y) = \bigcup_{k=1}^{K} \sum_{j=0}^{N=3} \phi_j^k h_j(r), \tag{A.18}$$

where $\hat{v}_j^k$ and ϕ_j^k are the values of $\hat{v}_h$ and ϕ_h at local node, respectively and r is the local coordinate ($r \in (]-1,1[)$). Equations (A.17) and (A.18) are the expressions for the solution and test functions in terms of the nodal basis. Explicit expressions for Hermite cubics are given in (Strang [49]). Hermite cubics interpolate both function and its derivative; therefore, we have a double unknown at each node. We proceed by choosing ϕ_0 and ϕ_2 to be unity at only one node and zero at other node, and ϕ_1 and ϕ_3 such that their first derivatives are unity at only one node (corresponding to previous nodes) and zero at other node.

We obtain the final discrete matrix statement of the eigenvalue problem

$$\sum_{k=1}^{K}{}' \sum_{i=0,j=0}^{N=3} A_{ij}^k \hat{v}_j^k = \omega \sum_{k=1}^{K}{}' \sum_{i=0,j=0}^{N=3} B_{ij}^k \hat{v}_j^k \tag{A.19}$$

where

$$A_{ij}^k = C_{ij}^k + D_{ij}^k + E_{ij}^k + F_{ij}^k, \tag{A.20}$$

$$C_{ij}^{k} = \left(\frac{2}{h}\right)^{3} \sum_{m=0}^{M} \rho_m \, D^2 h_j(\xi_m) \, D^2 h_i(\xi_m), \tag{A.21}$$

$$D_{ij}^{k} = \frac{2}{h} \sum_{m=0}^{M} \rho_m \left(2\alpha^2 + iRe\alpha \overline{U}(\xi_{m,k})\right) \, Dh_j(\xi_m) \, Dh_i(\xi_m), \tag{A.22}$$

$$E_{ij}^{k} = \frac{h}{2} \sum_{m=0}^{M} \rho_m \left(\alpha^4 + iRe\alpha^3 \overline{U}(\xi_{m,k}) + iRe\alpha \, D^2\overline{U}(\xi_{m,k})\right) h_j(\xi_m) \, h_i(\xi_m), \tag{A.23}$$

$$F_{ij}^{k} = \sum_{m=0}^{M} \rho_m iRe \, \alpha \, D\overline{U}(\xi_{m,k}) \, Dh_j(\xi_m) \, h_i(\xi_m), \tag{A.24}$$

$$B_{ij}^{k} = iRe \sum_{m=0}^{M} \rho_m \left(\frac{h}{2}\alpha^2 h_j(\xi_m) h_i(\xi_m) + \frac{2}{h} \, Dh_j(\xi_m) \, Dh_i(\xi_m)\right). \tag{A.25}$$

Here $\sum'$ denotes *direct stiffness* summation. In terms of the global representation we can write equation (A.19) in matrix form

$$\underline{A} \, \underline{\hat{v}} = \omega \, \underline{B} \, \underline{\hat{v}}, \tag{A.26}$$

where $\underline{\hat{v}}$ is a vector of nodal unknowns. The matrices A and B have a dimension of $((K+1) * 2) * ((K+1) * 2)$. Equation (A.26) is then solved using double precision arithmetic and the complex eigenvalue solver EISPACK on a Vax 750.

Below we present our result for the least stable mode with previous work for the Reynolds number of 20,000 and $\alpha = 2$. The utility and expansion of the method is given in Kozlu and Patera [32].

Author	Method	Least Stable Mode	# of nodes
Orszag [42]	Cheby. Poly.	0.2375265+i0.0037397	50
Thomas [54]	Finite Diff.	0.2375006+i0.0035925	50
Thomas [54]	Finite Diff.	0.2375243+i0.0037312	100
Gary and Helgason [11]	Finite Diff.	0.2375265+i0.0037397	100
Present work	Finite Elem.	0.2374832+i0.0037452	80

Table A.1: **The least stable mode** $(\frac{w}{\alpha})$ **for** $\alpha = 2$ **and** $Re = 20,000$.

Bibliography

[1] C. H. Amon. *Heat transfer enhancement and three-dimensional transitional flows by a spectral element-Fourier method.* PhD thesis, MIT, 1988.

[2] P. R. Bandyopadhyay. Rough-wall turbulent boundary layers in the transition regime. *J. Fluid Mech.*, 180:231, 1987.

[3] K. J. Bathe. *Finite element procedures in engineering analysis.* Prentice-Hall, New Jersey, 1982.

[4] B. J. Belhouse, F. H. Belhouse, C. M. Curl, T. I. Macmillan, A. J. Gunning, E. H. Spratt, S. B. MacMurray, and J. M. Nelems. A high efficiency membrane oxygenerator and pulsative pumping system, and its applications to animal trials. *Trans. Am. Soc. Artif. Internal Organs*, 19:77, 1973.

[5] A. E. Bergles. Techniques to augment heat transfer. In J. P. Hartnett W. M. Rohsenow and E. N. Ganic, editors, *Handbook of Heat Transfer Applications*, chapter 3, McGraw-Hill, New York, 1986.

[6] E. C. Brouillette, T. R. Mifflin, and J. E. Myers. Heat-transfer and pressure-

drop characteristics of internal finned tubes. *ASME*, Paper No: 57-A-47, 1957.

[7] A. P. Colburn. A method of correlating forced convection heat transfer data and a comparison with fluid friction. *Trans. Am. Ins. Chem. Engng.*, 29:174, 1933.

[8] D. F. Dipprey and R. H. Sabersky. Heat and momentum transfer in smooth and rough tubes at various Prandtl numbers. *Int. J. Heat Mass Transfer*, 14:601, 1963.

[9] P. G. Drazin and W. H. Reid. ***Hydrodynamic stability.*** Cambridge University Press, New York, 1981.

[10] P. Fortescue and W. B. Hall. Heat-transfer experiments on the fuel elements. *J. Brit. Nucl. Energy Conf.*, Session 2:83, 1957.

[11] J. Gary and R. Helgason. A matrix method for ordinary differential eigenvalue problems. *J. Comp. Phys.*, 5:169, 1970.

[12] N. K. Ghaddar, A. T. Patera, and B. B. Mikić. Heat transfer enhancement in oscillatory flow in a grooved channel. *AIAA Paper No.* 84-0495, 1984.

[13] N. K. Ghaddar, G. E. Karniadakis, and A. T. Patera. A conservative isoparametric spectral element method for forced convection; application to fully developed flow in periodic geometries. *Numer. Heat Transfer*, 9:277, 1986.

[14] N. K. Ghaddar, K. Z. Korczak, B. B. Mikić, and A. T. Patera. Numerical investigation of incompressible flow in grooved channels. Part 1: stability and self-sustained oscillations. *J. Fluid Mech.*, 163:99, 1986.

[15] N. K. Ghaddar, M. Magen, B. B. Mikić, and A. T. Patera. Numerical investigation of incompressible flow in grooved channels. Part 2: resonance and oscillatory heat transfer. *J. Fluid Mech.*, 168:541, 1986.

[16] A. J. Grass. Structural features of turbulent flow over smooth and rough boundaries. *J. Fluid Mech.*, 50:233, 1971.

[17] M. Greiner. *Experimental investigation of resonance and heat transfer enhancement in grooved channels.* PhD thesis, MIT, 1986.

[18] J. C. Han, L. R. Glicksman, and W. M. Rohsenow. An investigation of heat transfer and friction for rib-roughened surfaces. *Int. J. Heat Mass Transfer*, 21:1143, 1978.

[19] F. F. Huang. *Engineering Thermodynamics.* Macmillan Publishing Co., Inc., New York, 1976.

[20] A. K. M. F. Hussain and W. C. Reynolds. Measurements in fully developed turbulent channel flow. *J. Fluids Engng*, 97:567, 1975.

[21] M. S. Isaacson and A. A. Sonin. Sherwood number and friction factor correlations for electrodialysis systems, with application to process optimization. *I&EC Process Des. Dev.*, 15:313, 1976.

[22] T. Von Karman. The analogy between fluid friction and heat transfer. *Trans. ASME*, 705, 1939.

[23] G. E. Karniadakis. *Private Communication.* 1987.

[24] G. E. Karniadakis. *The spectral elements method applied to heat transport enhancement by flow destabilization.* PhD thesis, MIT, 1987.

[25] G. E. Karniadakis, B. B. Mikić, and A. T. Patera. Minimum dissipation transport enhancement by flow destabilization: Reynolds' analogy revisited. *J. Fluid Mech.*, 192:365, 1988.

[26] Y. Kawaguchi, K. Suzuki, and T. Sato. Heat transfer promotion with a cylinder array located near the wall. *Int. J. Heat Fluid Flow*, 6:249, 1985.

[27] W. M. Kays and M. E. Crawford. *Convective Heat and Mass Transfer.* McGraw-Hill, New York, 1980.

[28] W. M. Kays and A. L. London. *Compact Heat Exchangers.* McGraw-Hill, New York, 1964.

[29] W. M. Kays and H. C. Perkins. Forced convection internal flow in ducts. In J. P. Hartnett W. M. Rohsenow and E. N. Ganic, editors, *Handbook of Heat Transfer Fundamentals*, chapter 6, McGraw-Hill, New York, 1985.

[30] R. W. Keyes. Physical limits in digital electronics. *Proc. IEEE*, 63:740, 1975.

[31] S. J. Kline, C. A. Moore, and D. L. Cochran. Wide-angle diffusers of high performance and diffuser flow mechanism. *ASME J. Aero. Sci.*, 24(6):469, 1957.

[32] H. Kozlu and A. T. Patera. Solution of the free-surface Orr-Sommerfeld equation of hydrodynamic stability theory by a Hermitian finite element method. *Comm. Appl. Numer. Methods*, to appear, 1989.

[33] R. I. Loehrke and H. M. Nagib. Control of free-stream turbulence by means of honeycombs: a balance between suppression and generation. *J. Fluids Engineering*, 98:342, 1976.

[34] M. Magen, B. B. Mikić, and A. T. Patera. Bounds for conduction and forced convection heat transfer. *Int. J. Heat Mass Transfer*, 31(9):1747, 1988.

[35] P. Matisse and M. Gorman. Neutrally buoyant anisotropic particles for flow visualization. *Phys. Fluids*, 27(4):759, 1984.

[36] B. B. Mikić. A model for turbulent transport near a wall. In *Proc. Congr. for Theoretical and Applied Mechanics*, page 119, Kupari, Yugoslavia, 1981.

[37] B. B. Mikić. On destabilization of shear flows: concept of admissible system perturbations. *Int. Comm. Heat Mass Transfer*, 15:799, 1988.

[38] B. B. Mikić, H. Kozlu, and A. T. Patera. A methodology for optimization of convective cooling systems for electronic devices. *submitted to ICHMT XXth International Symposium, Yugoslavia*, 1988.

[39] T. Morel. Comprehensive design of axisymmetric wind tunnel contractions. *J. Fluids Engineering*, 97:225, 1975.

[40] W. Nakayama. Thermal management of electronic equipment: a review of technology and research topics. *Appl. Mech. Rev.*, 39(12):1847, 1986.

[41] R. H. Norris. Some simple approximate heat-transfer correlations for turbulent flow in ducts with rough surfaces. In A. E. Bergles and R. L. Webb, editors, *Augmentation of Convective Heat and Mass Transfer*, ASME, New York, 1970.

[42] S. A. Orszag. Accurate solution of the Orr-Sommerfeld stability equation.

J. Fluid Mech., 50:689, 1971.

[43] S. V. Patankar, C. H. Liu, and E. M. Sparrow. Fully developed flow and heat transfer in ducts having streamwise-periodic variations of cross-sectional area. *J. Heat Transfer*, 99:180, 1977.

[44] B. S. Petukhov. Heat transfer and friction in turbulent pipe flow with variable physical properties. In *Advances in Heat Transfer*, page 503, Academic Press, New York, 1970.

[45] L. Prandtl. Bemerkung uber den warme ubergang im rohr. *Physikalische Zeitschrift*, 29:487, 1928.

[46] O. Reynolds. On the extent and action of the heating surface for steam boilers. *Proc. Manchr Lit. Phil. Soc.*, 14:7, 1874.

[47] H. Schlichting. *Boundary Layer Theory.* McGraw-Hill, New York, 1968.

[48] E. M. Sparrow and W. Q. Tao. Enhanced heat transfer in a rectangular duct with streamwise-periodic disturbances at one principal wall. *J. Heat Transfer*, 105:851, 1983.

[49] G. Strang and G. J. Fix. *An analysis of the finite element method.* Prentice-Hall, New Jersey, 1973.

[50] I. Tani. Turbulent boundary layer development over rough surfaces. In H. U. Meier and P. Bradshaw, editors, *Perspectives in Turbulence Studies*, page 223, Springer-Verlag, New York, 1987.

[51] G. I. Taylor. The application of Osborne Reynolds's theory of heat transfer to flow through a pipe. *Proc. R. Soc. A.*, CXXIX:25, 1930.

[52] H. Tennekes and J. L. Lumley. *A First Course in Turbulence.* MIT Press, Cambridge, Massachusetts, 1972.

[53] L. C. Thomas. Turbulent burst phenomenon. In *Turbulent Forced Convection in Channels and Bundles*, page 491, Hemisphere, 1979.

[54] L. H. Thomas. The stability theory of the plane Poiseuille flow. *Phys. Rev.*, 91:780, 1953.

[55] H. W. Townes and R. H. Sabersky. Experiments on the flow over a rough surface. *Int. J. Heat Mass Transfer*, 9:729, 1966.

[56] D. B. Tuckerman. *Heat transfer microstructures for integrated circuits.* PhD thesis, Stanford University, 1984.

[57] D. B. Tuckerman and R. F. W. Pease. High performance heat sinking for VLSI. *IEEE Electron Device lett.*, EDL-2(5):126, 1981.

[58] R. L. Webb and A. E. Bergles. Performance evaluation criteria for selection of heat transfer surface geometries used in low Reynolds number heat exchangers. In R. K. Shah S. Kakac and A. E. Bergles, editors, *Low Reynolds Number Flow Heat Exchangers*, page 735, Hemisphere, Washington, DC, 1983.

[59] R. L. Webb and M. J. Scott. A parametric analysis of the performance of internally finned tubes for heat exchanger application. In J. W. Michel J. M. Chenoweth, J. Kaellis and S. Shenkman, editors, *Advances in Heat Transfer*, page 61, ASME, New York, 1979.

[60] A. M. Wo. *A comparison of three methods in improving the performance of a very wide angle diffuser.* Master's thesis, MIT, 1982.

[61] V. Zajic. Some results on research of intensified water cooling by roughened surfaces and surface boiling at high heat flux rates. *ACTA TECHNICA CSAV*, 5:602, 1965.

Figure Captions

Figure 1. Basic channel geometry for the optimization study. The channel is of length L, and height H, with uniform heat flux q'' imposed on the top wall, ∂D_T, and an adiabatic bottom surface, ∂D_B.

Figure 2. Thermal behavior of plane Poiseuille flow with uniform heat flux q'' imposed on the wall.

Figure 3. A plot of dimensionless channel height versus thermal load for the plane Poiseuille flow shown in Figure 1 at fixed Reynolds numbers and pumping powers. Air is the working fluid (Pr=0.71).

Figure 4. A plot of dimensionless channel height versus thermal load for circular channels with uniform wall-heat flux at fixed Reynolds numbers and pumping powers. Air is the working fluid (Pr=0.71).

Figure 5. The function $g(\mu)$ as a function of μ. Note that drastic changes occur outside the range $0.3 < \mu < 0.5$.

Figure 6. A plot of optimum pumping power versus thermal load for laminar and turbulent smooth-channel flows. – – laminar flow. —— turbulent flow. Air is the working fluid (Pr=0.71).

Figure 7a. The geometry of the periodic eddy-promoter channel is described by the distance between successive eddy-promoter cylinders, L, the diameter of the eddy-promoters, D, and the distance of the eddy-promoters from the wall, B.

Figure 7b. The geometry of the periodic micro-grooved channel is described by the depth of the groove, e, the groove length, a, and the groove dwell, c. The vertical scale of the grooves is greatly exaggerated for clarity.

Figure 7c. The geometry of the periodic micro-cylindered channel is described by the distance between successive micro-cylinders, l, the diameter of the micro-cylinder, d, and the distance of the micro-cylinders from the wall, b. The scale of the cylinders is greatly exaggerated for clarity.

Figure 8. Basic channel geometry for the optimization study with constant wall temperature. The channel is of length L, and height H, with constant temperature T_w imposed on the top wall, ∂D_T, and an adiabatic bottom surface, ∂D_B.

Figure 9. Thermal behavior of plane Poiseuille flow with uniform wall temperature.

Figure 10. A plot of dimensionless channel height versus thermal load for the

for the plane Poiseuille flow shown in Figure 8 at fixed Reynolds numbers and pumping powers. Air is the working fluid (Pr=0.71).

Figure 11. The function $g_T(\mu)$ as a function of μ. Note that drastic changes occur outside the range $0.5 < \mu < 0.7$.

Figure 12. A schematic of the open-circuit double-contraction wind tunnel. Note that the wind tunnel is bolted to the laboratory floor and it is free of any appreciable vibration. The experimental test sections are connected to the exit of the wind tunnel.

Figure 13. Details of the test section for the geometry Z_1. For the geometry Z_0 (laminar flows) the same test section is used with the micro-cylinders removed. All units are in meters.

Figure 14. Details of the test section for the geometry Z_2. The inner walls in the heated region are made of high conductivity aluminum to insure that the temperature difference between thermocouples and the grooved surface is small. All units are in meters.

Figure 15. Details of the test section for the geometry Z_3. For micro-cylinders stainless steel piano wires are used. For the geometry Z_0 (turbulent flows) the same test section is used with the micro-cylinders removed. All units are in

meters.

Figure 16. A measured velocity profile (■) $3d$ (d is the cylinder diameter, $d/H = 0.1$) behind a single cylinder placed in the center of a fully-developed plane Poiseuille flow. The hot-wire probe is used for the measurement. Solid line is the numerical solution by Karniadakis [23].

Figure 17. A schematic of the test section used for the smoke-wire technique in which 'unwanted' gravitational effects due to low velocities are eliminated.

Figure 18. A schematic of the water-channel facility. The test section has the dimensions as given for Figure 7a.

Figure 19. Minco electrical strip heater strand pattern. These heaters are bonded on the top plexiglass wall in the geometry Z_1 (Figure 13). The actual dimensions are $0.75'' \times 8''$.

Figure 20. Thermal-Circuits Co. electrical strip heater strand pattern. These heaters are used for the geometries Z_2 and Z_3 and are bonded on the top/bottom aluminum walls (Figures 14-15). The actual dimensions are $4\frac{3}{8}'' \times 12''$.

Figure 21. The flow patterns obtained in the water-channel flow visualizations at $Re = 129$. The flow is right to left.

Figure 22. The smoke-wire visualization of a stable steady eddy-promoter flow. The flow is right to left.

Figure 23. A plot of the isotherms of the steady subcritical flow at $Re = 166.66$ for $Pr = 1.0$ (Karniadakis, Mikić and Patera [25]). The temperature distribution differs only slightly from that for fully-developed plane channel flow.

Figure 24. The flow patterns obtained in the water-channel flow visualizations at $Re = 396$. The flow is right to left. The picture clearly indicates that this is a two-wave flow.

Figure 25. The flow patterns obtained in the water-channel flow visualizations at $Re = 396$. The flow is right to left. The picture clearly indicates that this is a two-wave flow.

Figure 26. A plot of unsteady isotherms at one instant in time of the steady-periodic supercritical channel flow at $Re = 400$ for $Pr = 1.0$. Figure clearly supports the two-wave flow as found in the experimental studies (Karniadakis, Mikić and Patera [25]).

Figure 27. The flow patterns obtained in the water-channel flow visualizations at $Re = 1132$. The flow is right to left. A mixed core flow and a 'smaller-scale' (compared to the previous observations) near-wall structure is obtained.

Figure 28. The smoke-wire visualization of a transitional-Reynolds-number flow. The flow is right to left.

Figure 29. Heat transfer data for $Pr = 0.71$. Z_0 (smooth channel): ○, experiment; –·–, laminar analytical solution; ——, turbulent correlation (Kays and Crawford [27]) (the dashed line indicates the Reynolds number range for which the correlation is somewhat suspect). Z_1 (eddy promoters): □, experiment; ◒, numerical (▬ indicates transitional flows). Z_2 (micro-grooves): △, experiment. Z_3 (micro-cylinders): ◇, experiment. In all cases solid symbols (together with ◒) refer to laminar (steady or unsteady) flows, and the open symbols refer to turbulent flows.

Figure 30. Friction factor data. Z_0 (smooth channel): ○, experiment; –·–, laminar analytical solution; ——, turbulent correlation (Kays and Crawford [27]) (the dashed line indicates the Reynolds number range for which the correlation is somewhat suspect). Z_1 (eddy promoters): □, experiment; ◒, numerical (▬ indicates transitional flows). Z_2 (micro-grooves): △, experiment. Z_3 (micro-cylinders): ◇, experiment. In all cases solid symbols (together with ◒) refer to laminar (steady or unsteady) flows, and the open symbols refer to turbulent flows.

Figure 31. A plot of $\overline{\Psi}(\mu, Z_n)$ for a fixed thermal load of $\Lambda = 800$ based on

the data sets of Figures 29 and 30. The minimum of $\overline{\Psi}(\mu, Z_n)$ for each Z_n curve gives one point $\overline{\Psi}^*(\Lambda = 800)$ in Figure 32. Note that from μ_n^* we can find the optimizaing channel height H and flow velocity V.

Figure 32. A plot of $\overline{\Psi}_n^*$ for Z_0, Z_1, Z_2, and Z_3 based on the data sets of Figures 29 and 30. Z_0 (smooth channel); $-\cdot-$, global optimum corresponds to laminar flow; ——, global optimum corresponds to turbulent flow. Z_1 (eddy promoters): □, experiment (⬒ indicates transitional flows). Z_2 (micro-grooves): △, experiment. Z_3 (micro-cylinders): ◇, experiment.

Figure 33. Heat transfer data for $Pr = 0.71$. Z_0 (smooth channel): □, experiment; ——, turbulent correlation (Kays and Crawford [27]). Z_2 (micro-grooves): △. Z_3^m, $m = 1, 2, 3, 4$ (micro-cylinders, see Table 5.1): ◇, Z_3^1; ▼, Z_3^2; ○, Z_3^3; ■, Z_3^4.

Figure 34. Friction coefficient data. Z_0 (smooth channel): □, experiment; ——, turbulent correlation (Kays and Crawford [27]). Z_2 (micro-grooves): △. Z_3^m, $m = 1, 2, 3, 4$ (micro-cylinders, see Table 5.1): ◇, Z_3^1; ▼, Z_3^2; ○, Z_3^3; ■, Z_3^4.

Figure 35. Modified Colburn analogy factor as a function of roughness Reynolds number. Z_2 (micro-grooves): △. Z_3^m, $m = 1, 2, 3, 4$ (micro-cylinders, see Table

5.1): $\diamond$, Z_3^1; $\blacktriangledown$, Z_3^2; $\bigcirc$, Z_3^3; $\blacksquare$, Z_3^4.

Figure 36. Nusselt number enhancement ratio ($E = Nu_{enhanced}/Nu_{smooth}$) as a function of the roughness Reynolds number. Z_3^m, $m = 1,2,3,4,5$ (micro-cylinders, see Table 5.1): $\diamond$, Z_3^1; $\blacktriangledown$, Z_3^2; $\bigcirc$, Z_3^3; $\blacksquare$, Z_3^4; $\bullet$, Z_3^5.

Figure 37. Heat transfer data for $Pr = 0.71$. Z_0 (smooth channel): $\square$, experiment; ——, turbulent correlation (Kays and Crawford [27]). Z_3^m, $m = 3,5,6,7$ (micro-cylinders, see Table 5.1); $\bigcirc$, Z_3^3; $\bullet$, Z_3^5; $\oplus$, Z_3^6; $\odot$, Z_3^7.

Figure 38. Friction coefficient data. Z_0 (smooth channel): $\square$, experiment; ——, turbulent correlation (Kays and Crawford [27]). Z_3^m, $m = 3,5,6,7$ (micro-cylinders, see Table 5.1): $\bigcirc$, Z_3^3; $\bullet$, Z_3^5; $\oplus$, Z_3^6; $\odot$, Z_3^7.

Figure 39. A plot of minimum dissipation as a function of thermal load. The plot is based on the data sets of Figures 33 and 34. Z_0 (smooth channel): ——. Z_2 (micro-grooves): $\triangle$. Z_3^m, $m = 1,3,4$ (micro-cylinders, see Table 5.1): $\diamond$, Z_3^1; $\bigcirc$, Z_3^3; $\blacksquare$, Z_3^4.

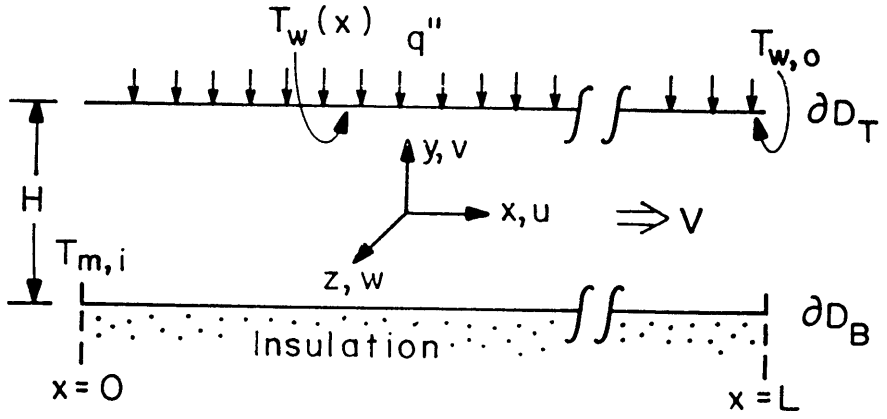

$T_w(x)$
q"
$T_{w,o}$
∂D_T
y, v
x, u
$\Rightarrow V$
H
$T_{m,i}$
z, w
∂D_B
Insulation
x = 0
x = L

Figure 1

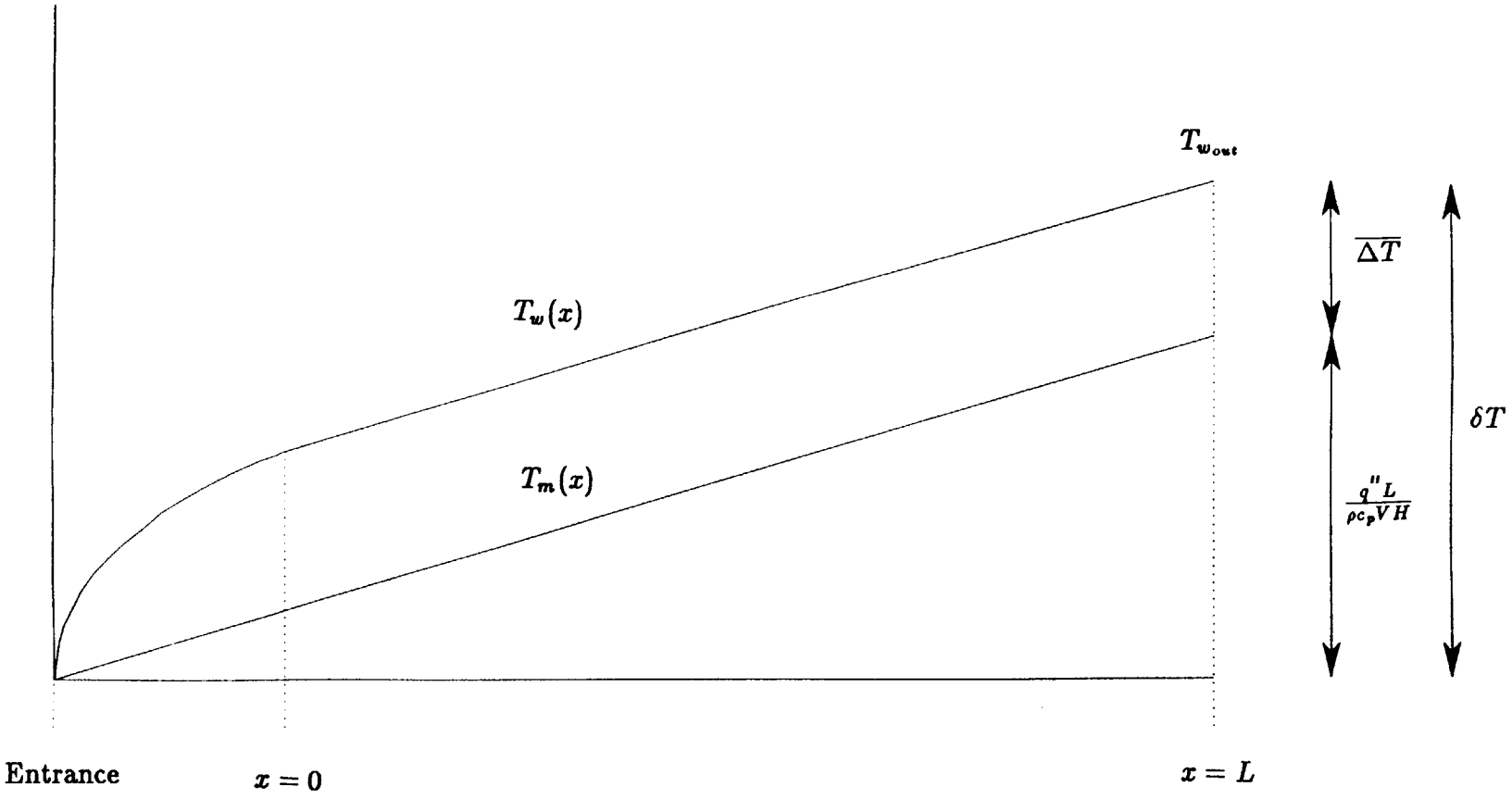

$T_{w_{out}}$
$T_w(x)$
$T_m(x)$
$\overline{\Delta T}$
δT
$\frac{q''L}{\rho c_p V H}$
Entrance
$x = 0$
$x = L$

Figure 2

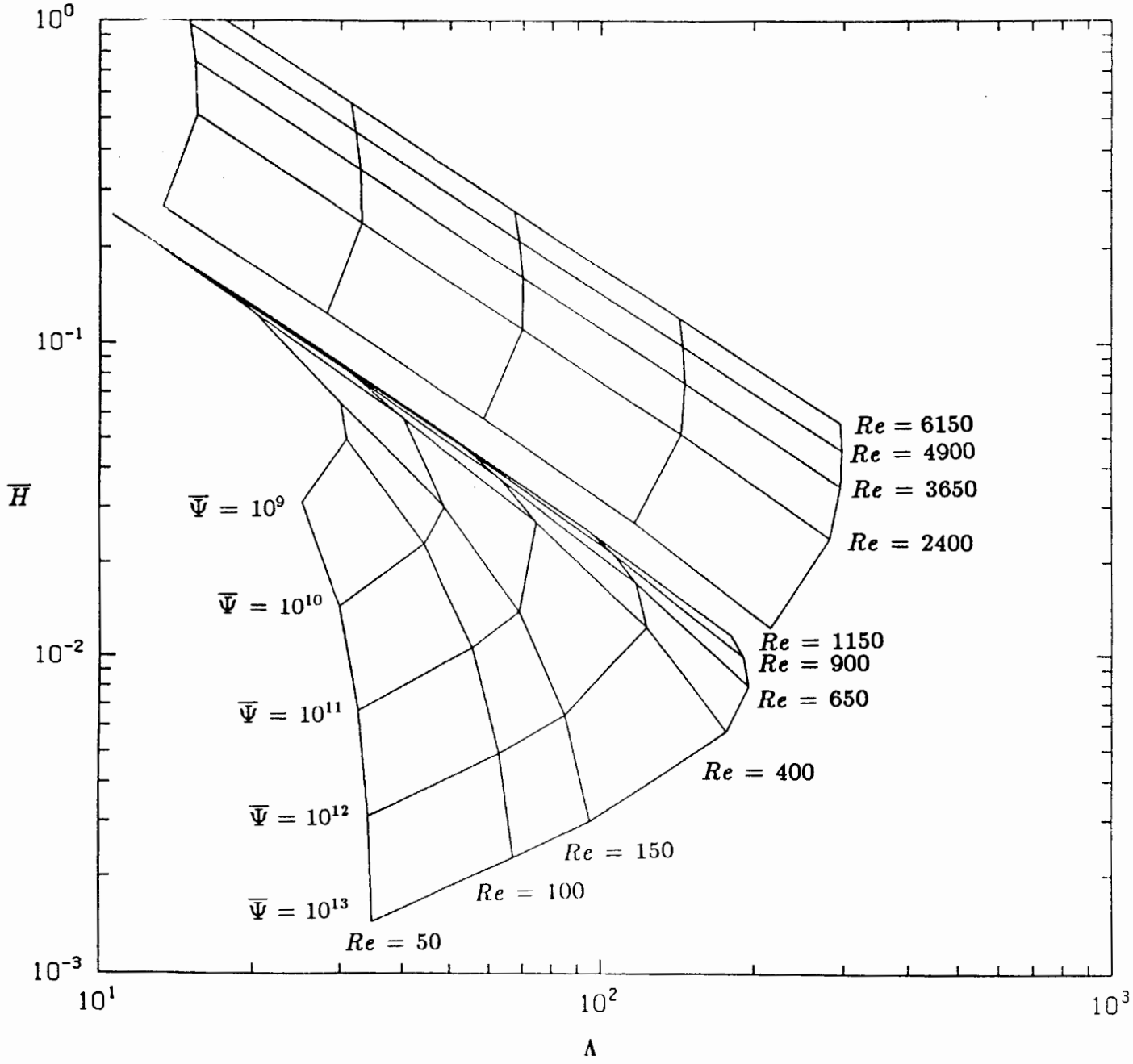

10^0
10^{-1}
10^{-2}
10^{-3}
10^1
10^2
10^3
$\overline{H}$
Λ
$\overline{\Psi} = 10^9$
$\overline{\Psi} = 10^{10}$
$\overline{\Psi} = 10^{11}$
$\overline{\Psi} = 10^{12}$
$\overline{\Psi} = 10^{13}$
$Re = 6150$
$Re = 4900$
$Re = 3650$
$Re = 2400$
$Re = 1150$
$Re = 900$
$Re = 650$
$Re = 400$
$Re = 150$
$Re = 100$
$Re = 50$

Figure 3

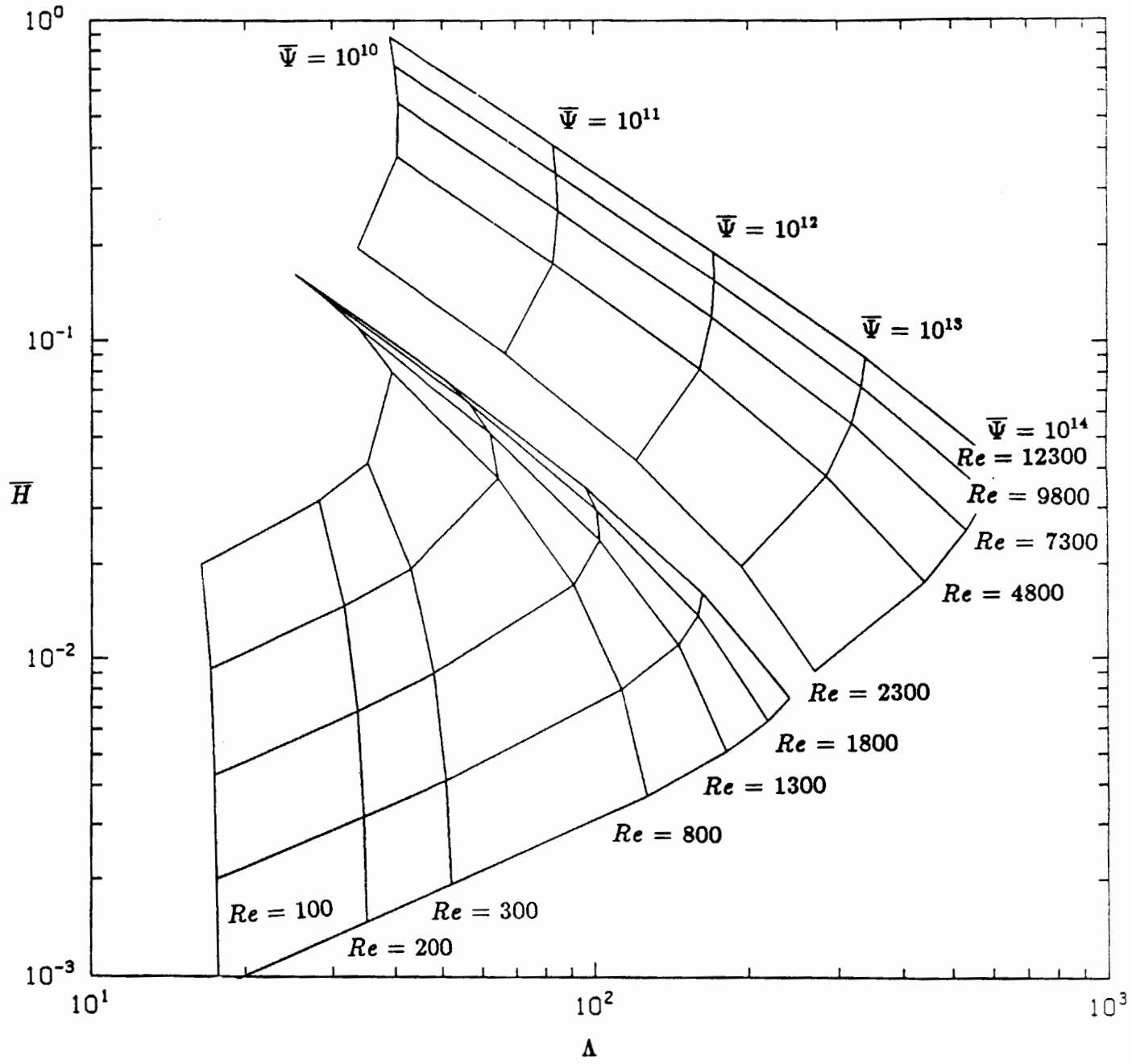

10^0
10^{-1}
10^{-2}
10^{-3}
10^1
10^2
10^3
$\overline{H}$
Λ
$\overline{\Psi} = 10^{10}$
$\overline{\Psi} = 10^{11}$
$\overline{\Psi} = 10^{12}$
$\overline{\Psi} = 10^{13}$
$\overline{\Psi} = 10^{14}$
$Re = 12300$
$Re = 9800$
$Re = 7300$
$Re = 4800$
$Re = 2300$
$Re = 1800$
$Re = 1300$
$Re = 800$
$Re = 300$
$Re = 200$
$Re = 100$

Figure 4

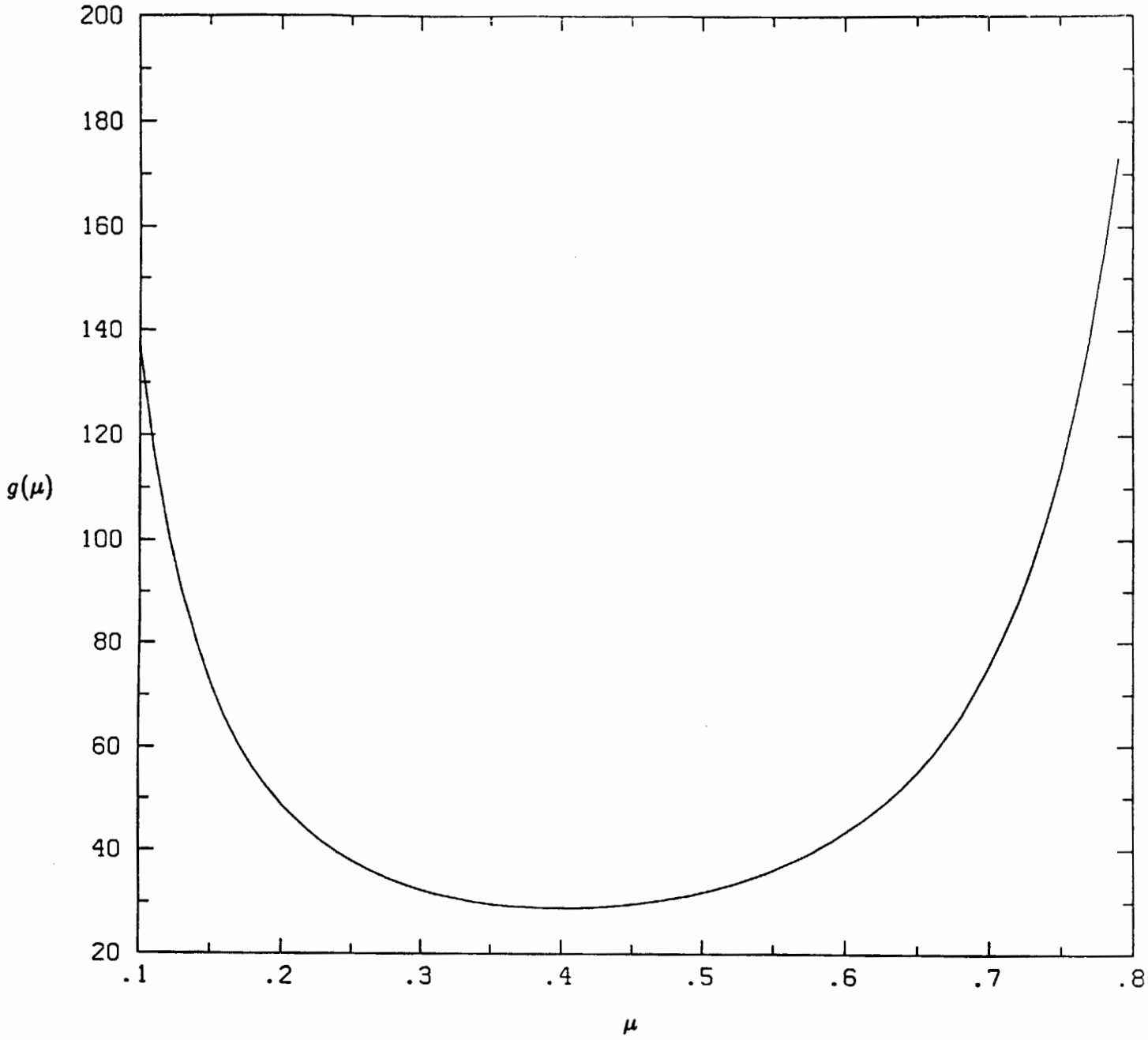


Figure 5

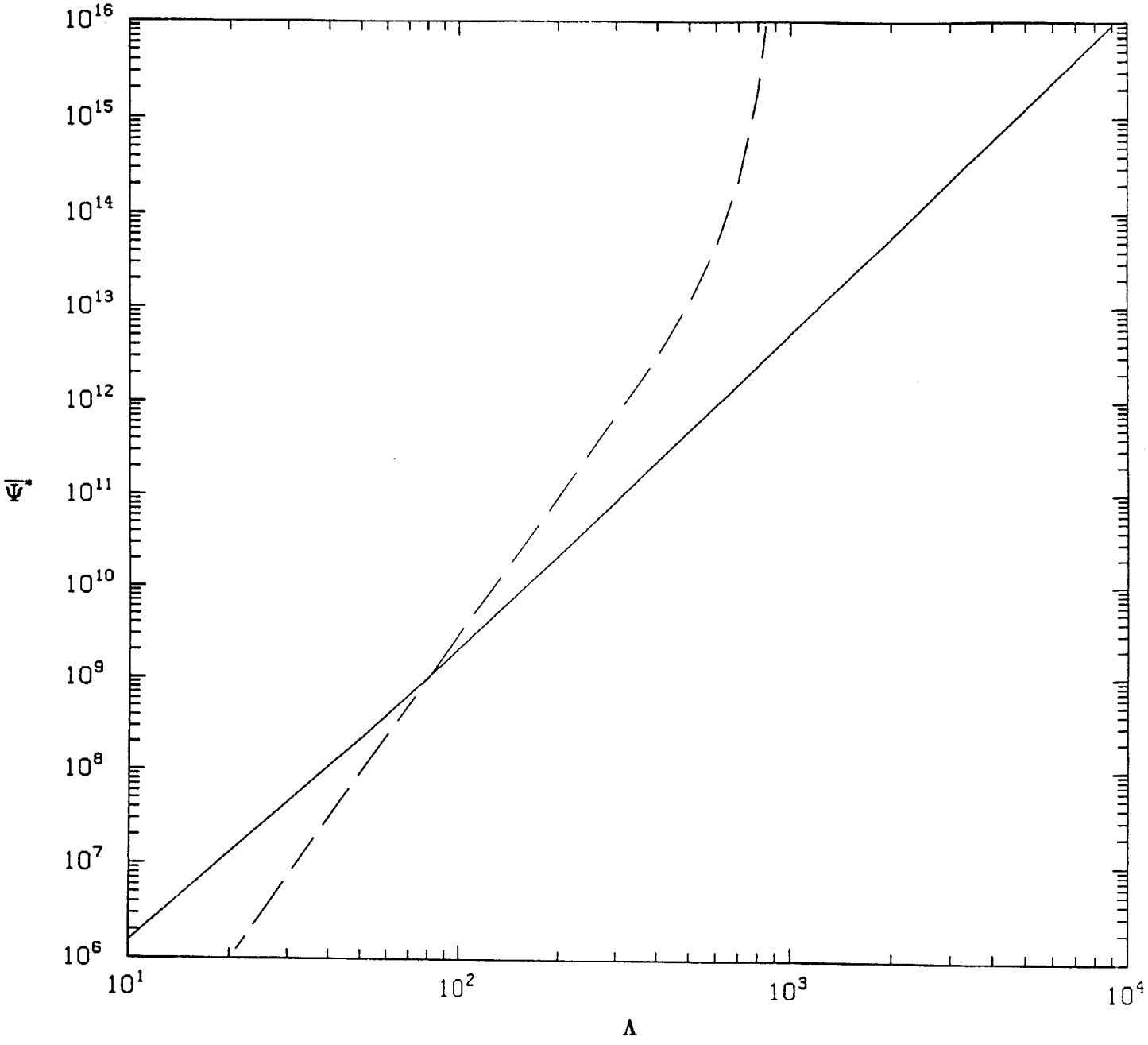

10^{16}
10^{15}
10^{14}
10^{13}
10^{12}
10^{11}
10^{10}
10^{9}
10^{8}
10^{7}
10^{6}
Ψ^*
10^{1}
10^{2}
10^{3}
10^{4}
Λ

Figure 6

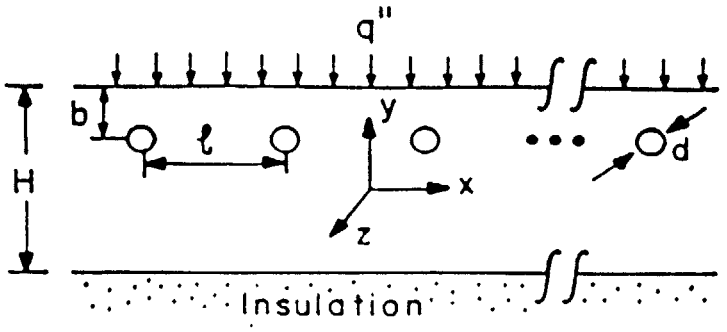


Figure 7a

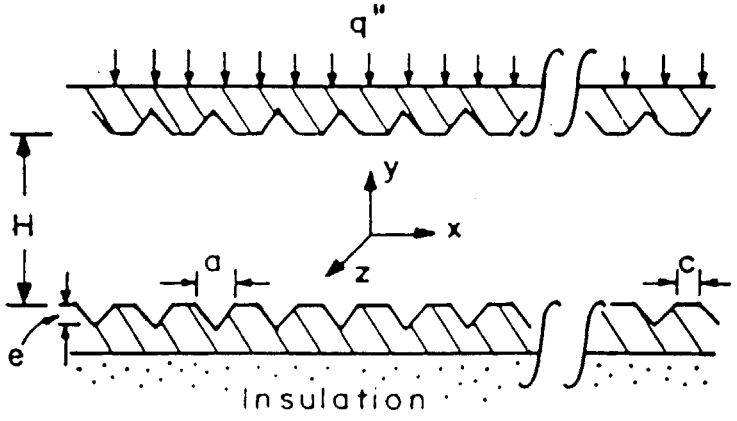


Figure 7b

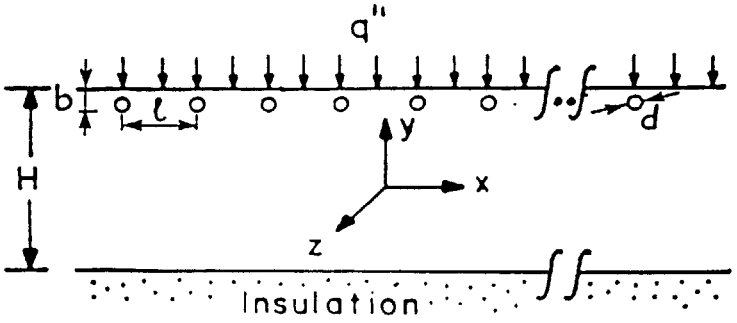


Figure 7c

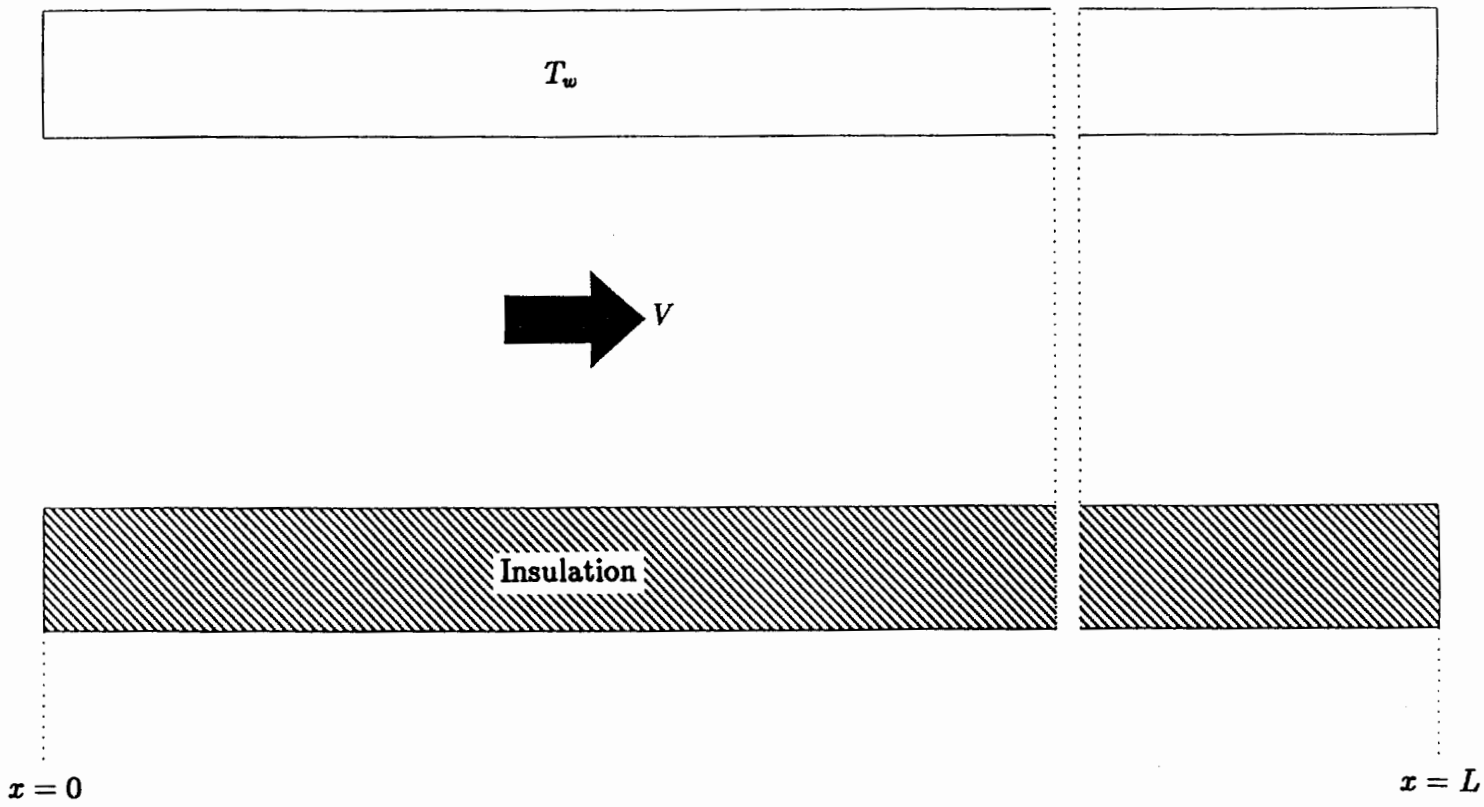


Figure 8

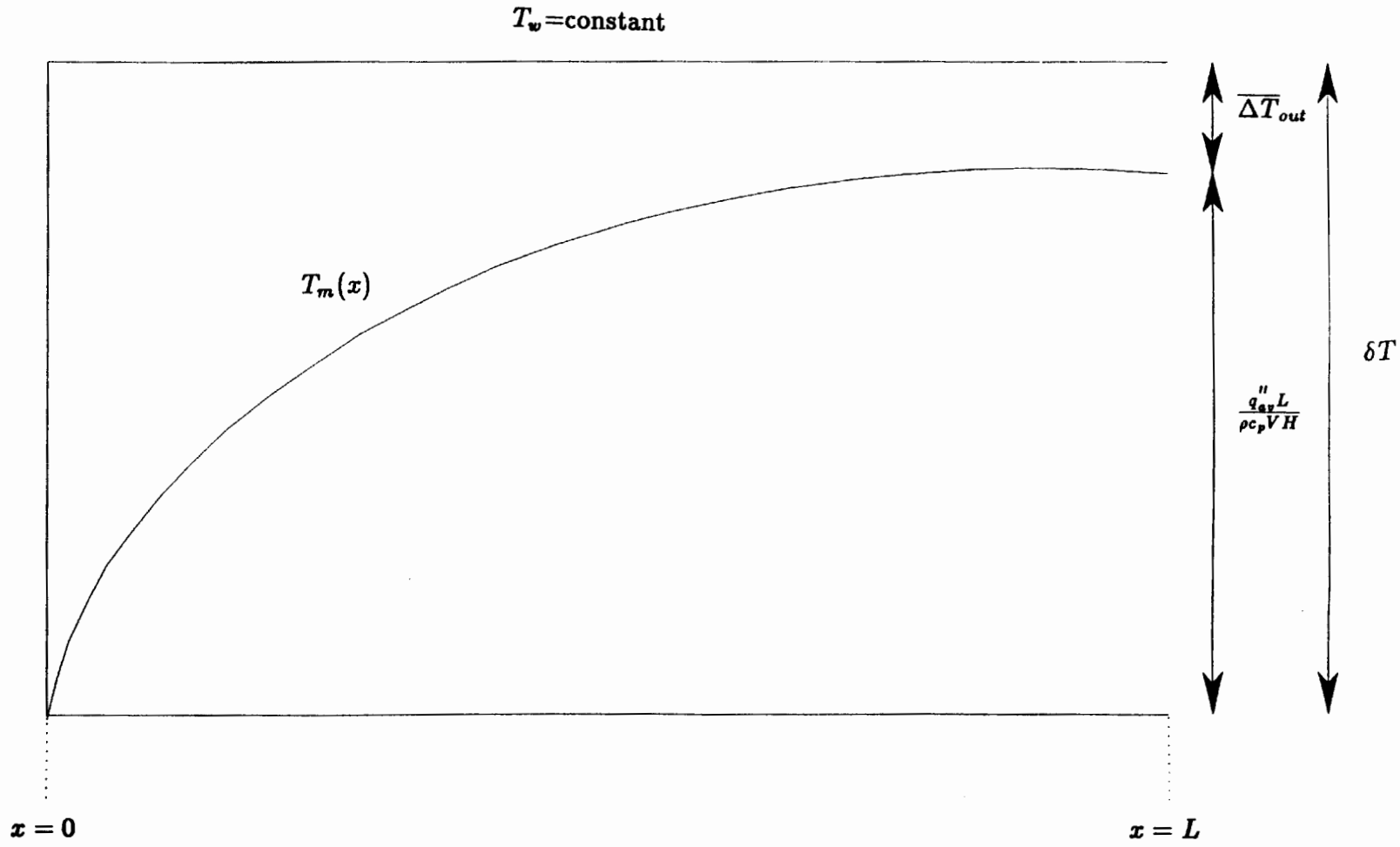

T_w=constant
$T_m(x)$
$\overline{\Delta T}_{out}$
$\frac{q''_{sy}L}{\rho c_p V H}$
δT
$x = 0$
$x = L$

Figure 9

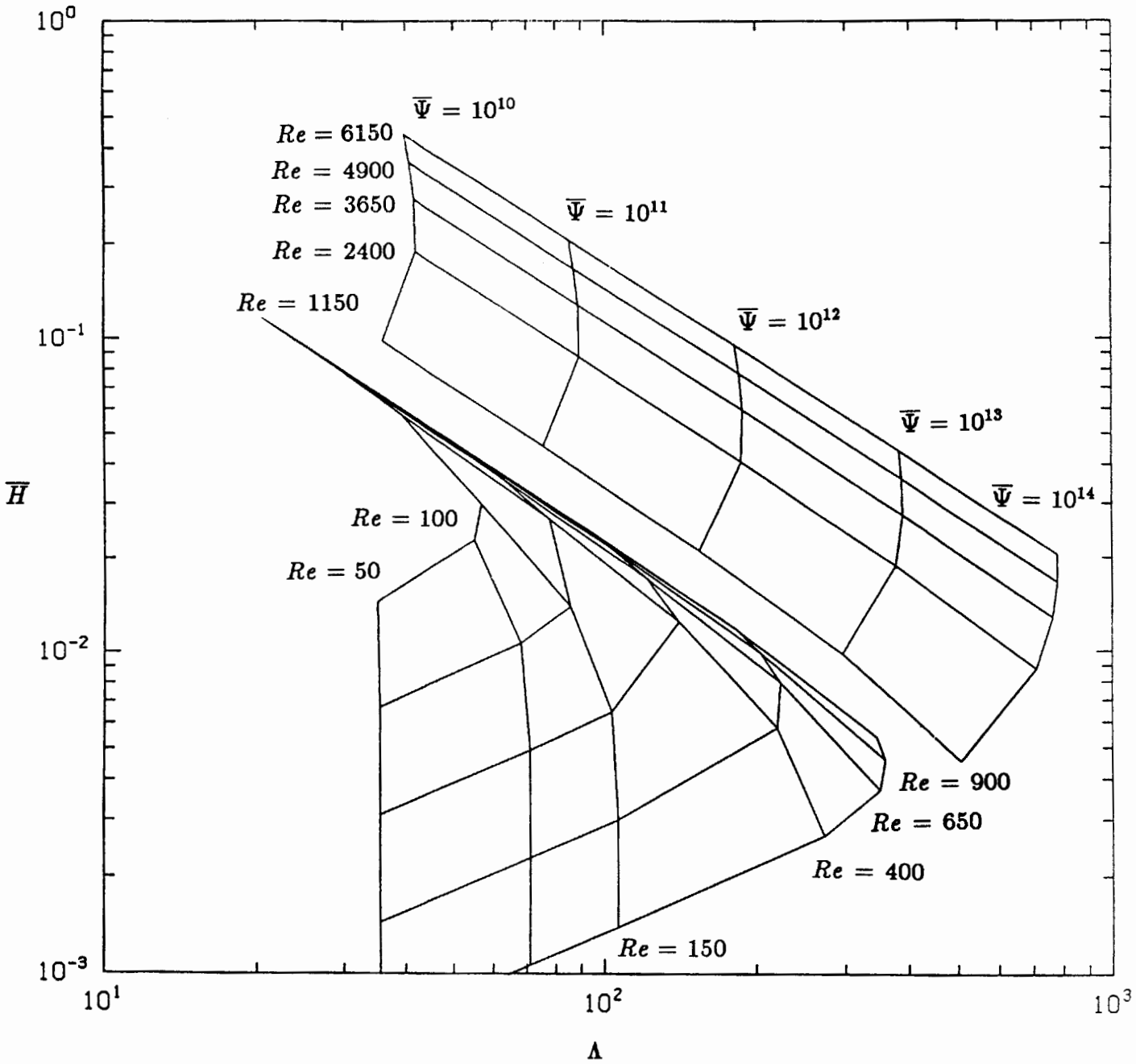

10^0
10^{-1}
10^{-2}
10^{-3}
$\overline{H}$
10^1
10^2
10^3
Λ
$\overline{\Psi} = 10^{10}$
$\overline{\Psi} = 10^{11}$
$\overline{\Psi} = 10^{12}$
$\overline{\Psi} = 10^{13}$
$\overline{\Psi} = 10^{14}$
$Re = 6150$
$Re = 4900$
$Re = 3650$
$Re = 2400$
$Re = 1150$
$Re = 900$
$Re = 650$
$Re = 400$
$Re = 150$
$Re = 100$
$Re = 50$

Figure 10

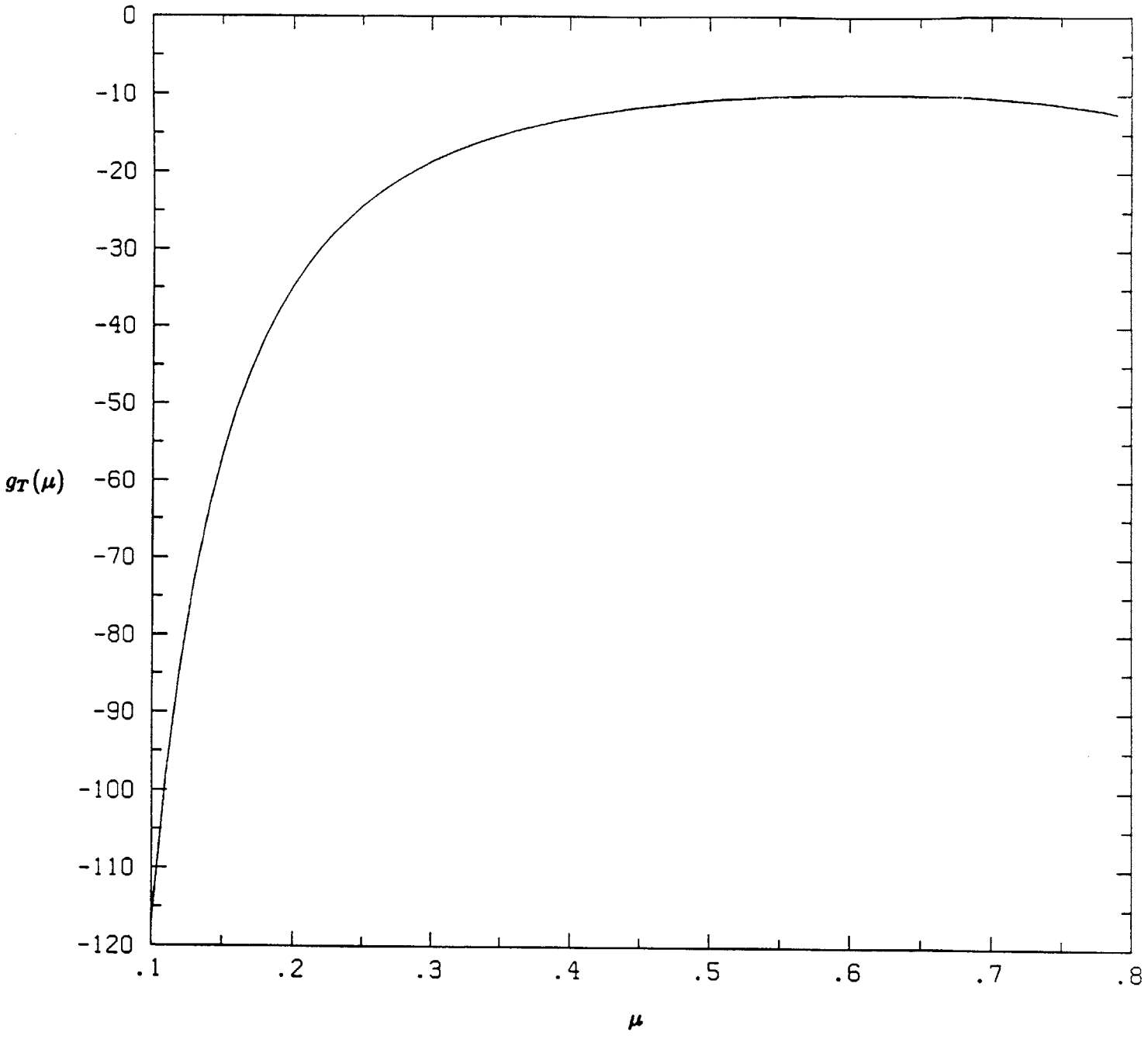


Figure 11

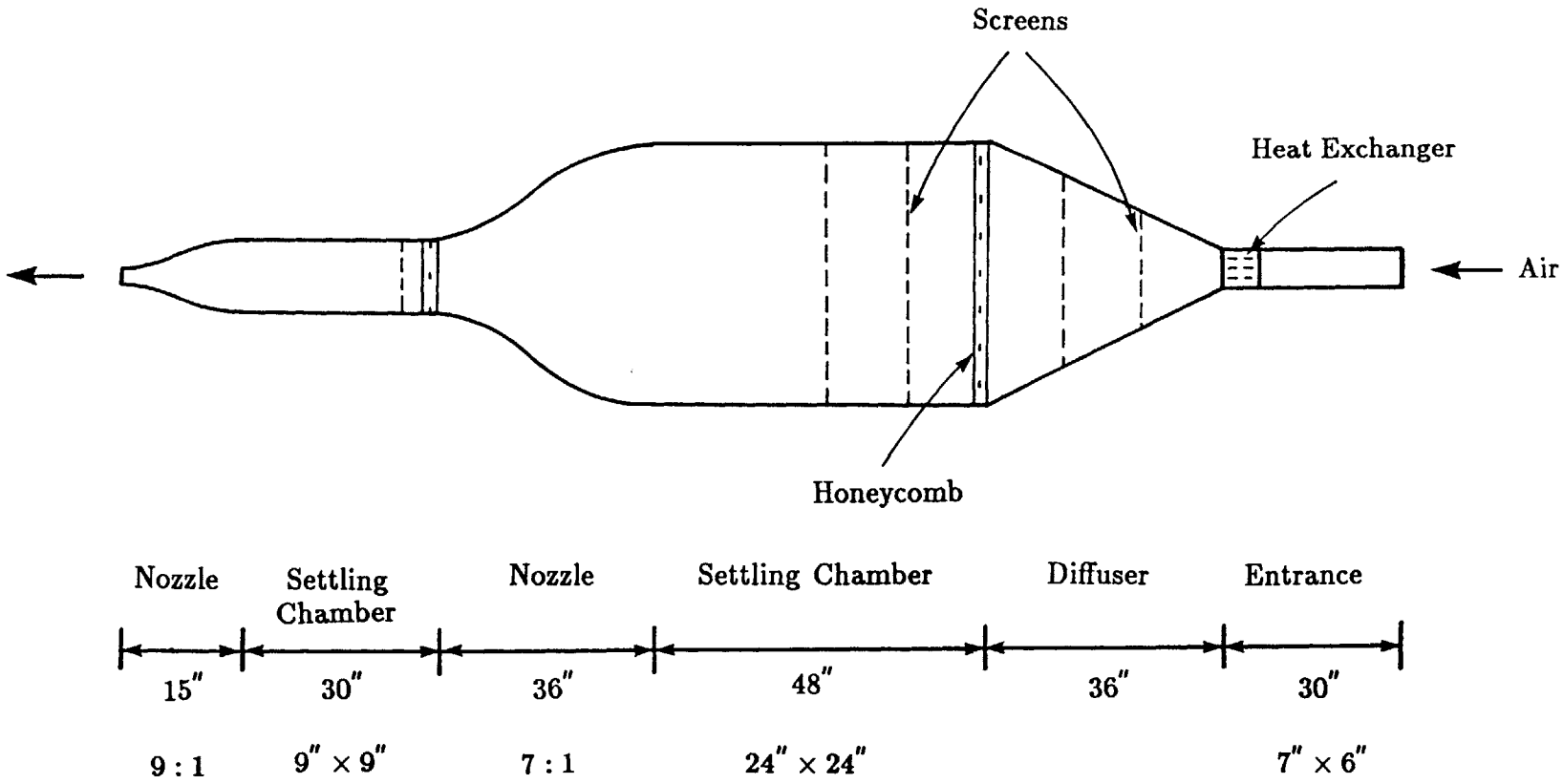

Screens
Heat Exchanger
Air
Honeycomb
Nozzle
Settling Chamber
Nozzle
Settling Chamber
Diffuser
Entrance
15"
30"
36"
48"
36"
30"
9 : 1
9" × 9"
7 : 1
24" × 24"
7" × 6"

Figure 12

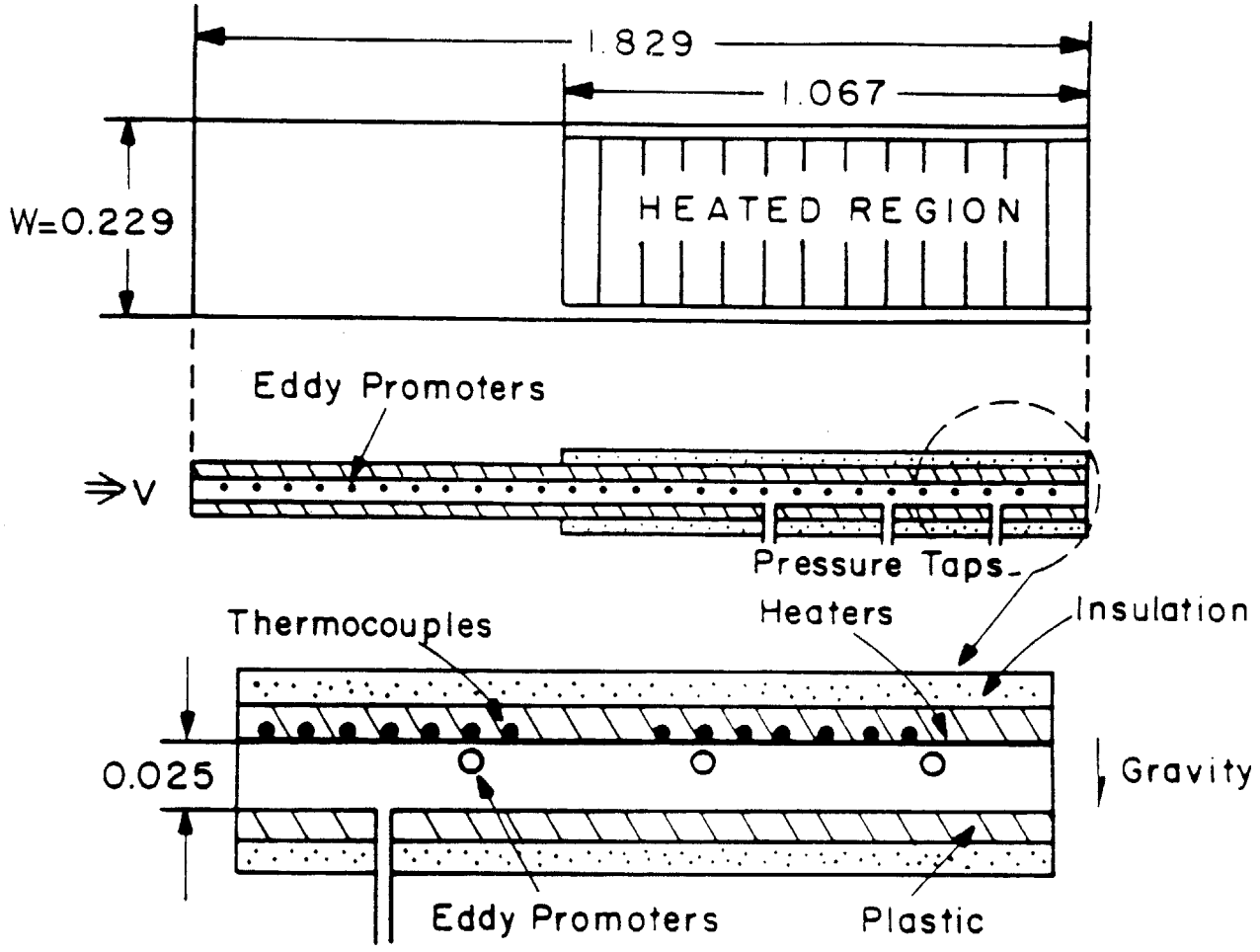

1.829
1.067
W=0.229
HEATED REGION
Eddy Promoters
⇒V
Pressure Taps
Thermocouples
Heaters
Insulation
0.025
Gravity
Eddy Promoters
Plastic

Figure 13

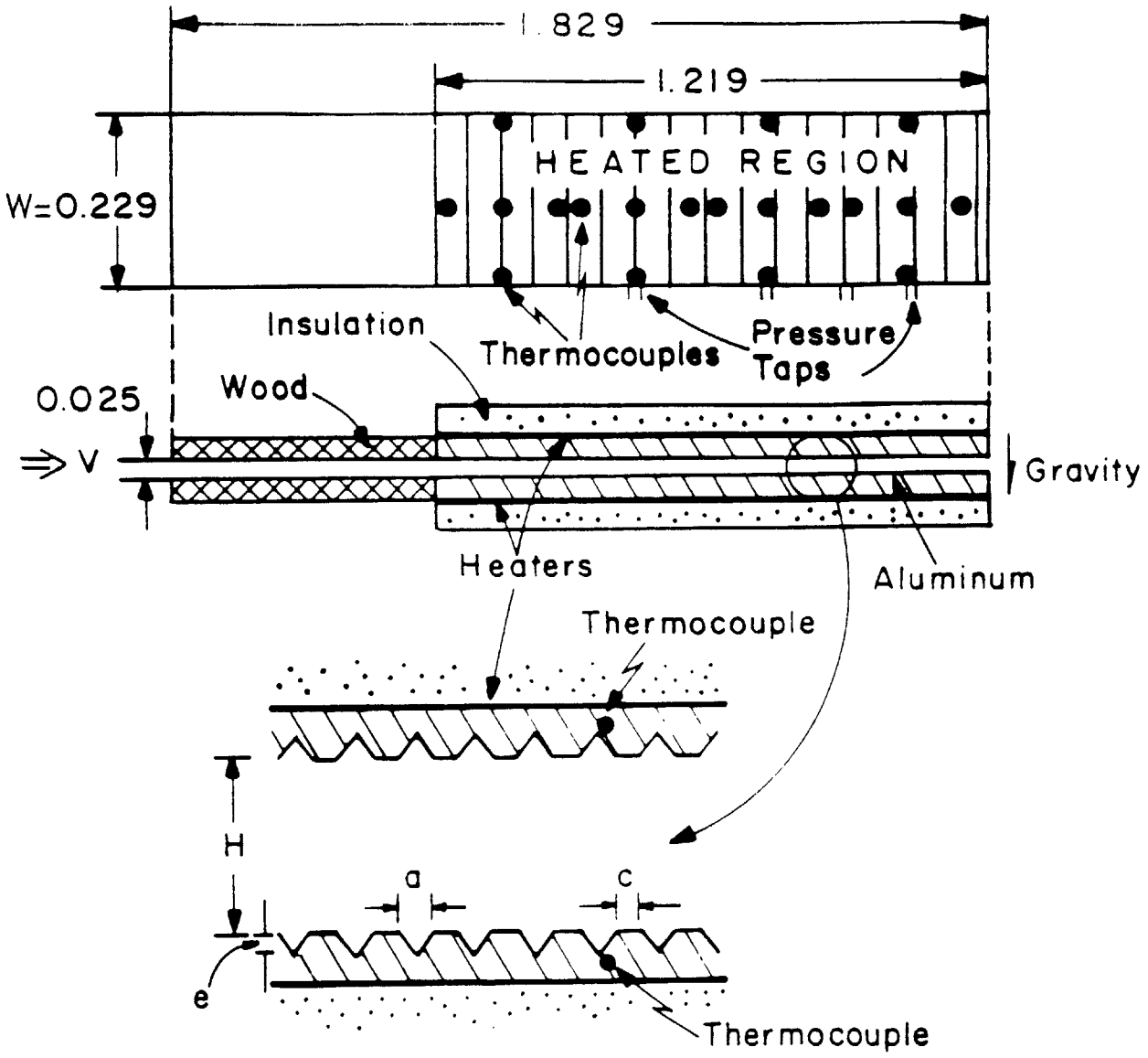

1.829
1.219
HEATED REGION
W=0.229
Insulation
Thermocouples
Pressure Taps
0.025
Wood
⇒ V
Gravity
Heaters
Aluminum
Thermocouple
H
a
c
e
Thermocouple

Figure 14

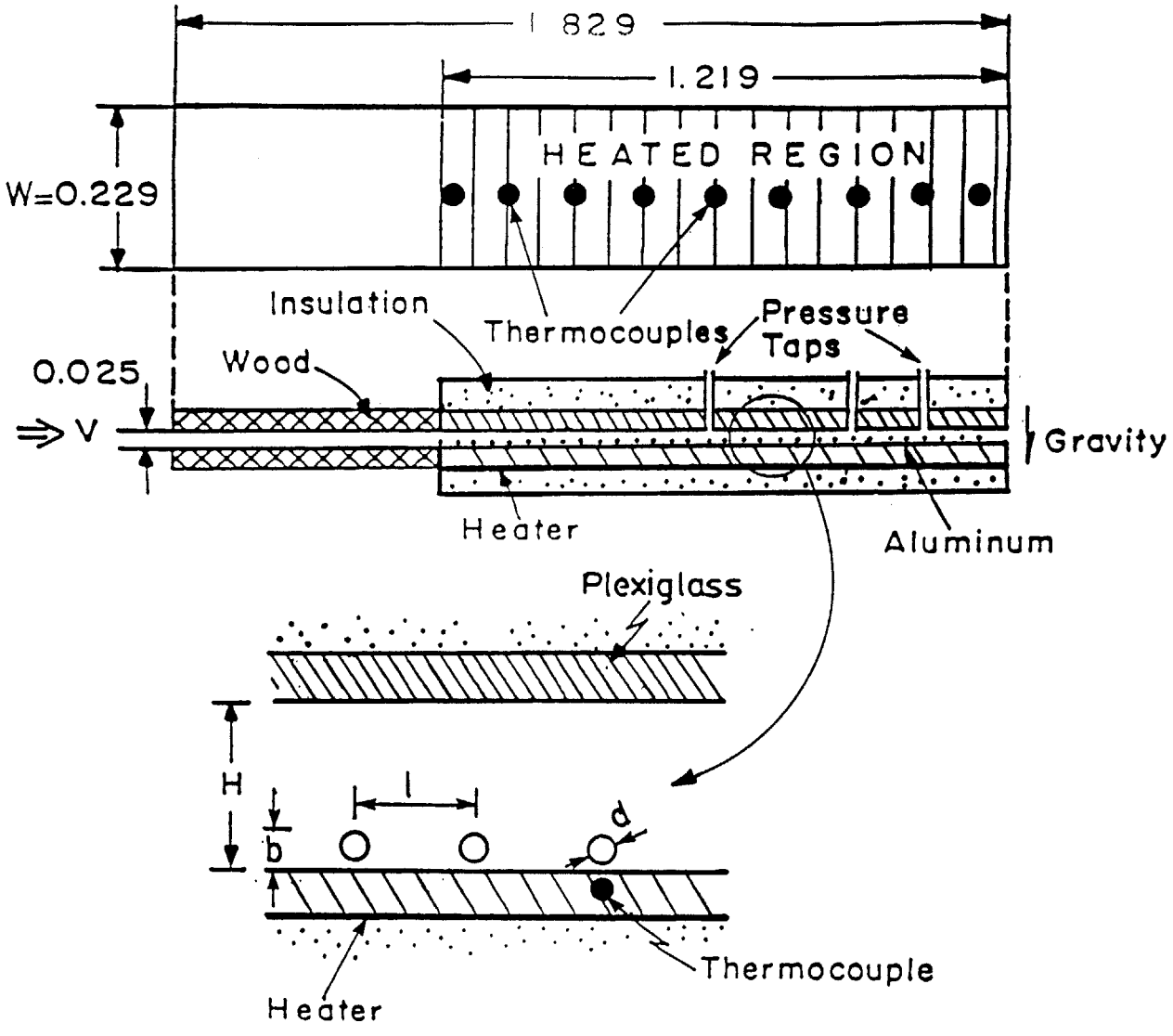

1.829
1.219
HEATED REGION
W=0.229
Insulation
Thermocouples
Pressure Taps
Wood
0.025
V
Gravity
Heater
Aluminum
Plexiglass
H
l
b
d
Thermocouple
Heater

Figure 15

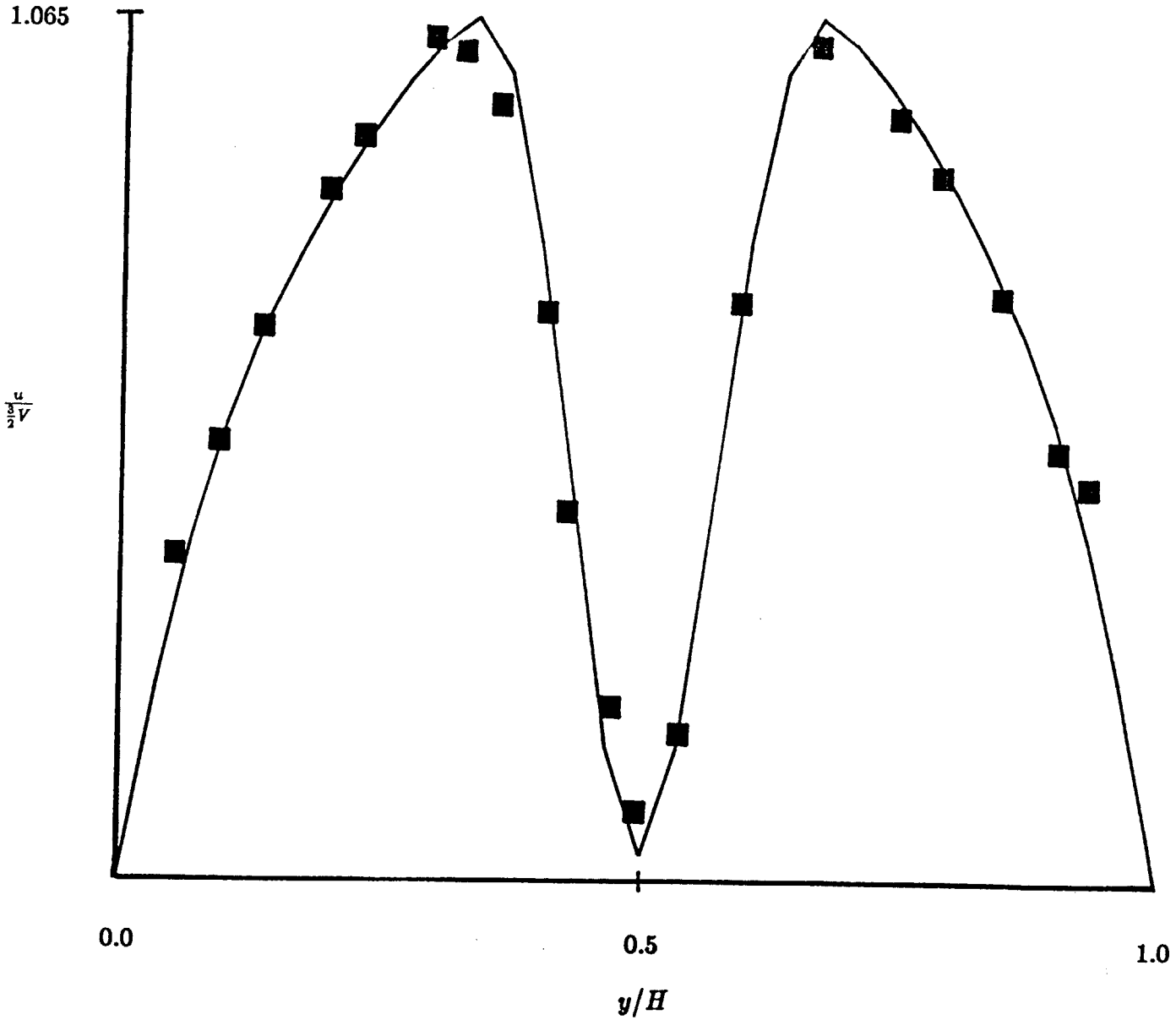


Figure 16

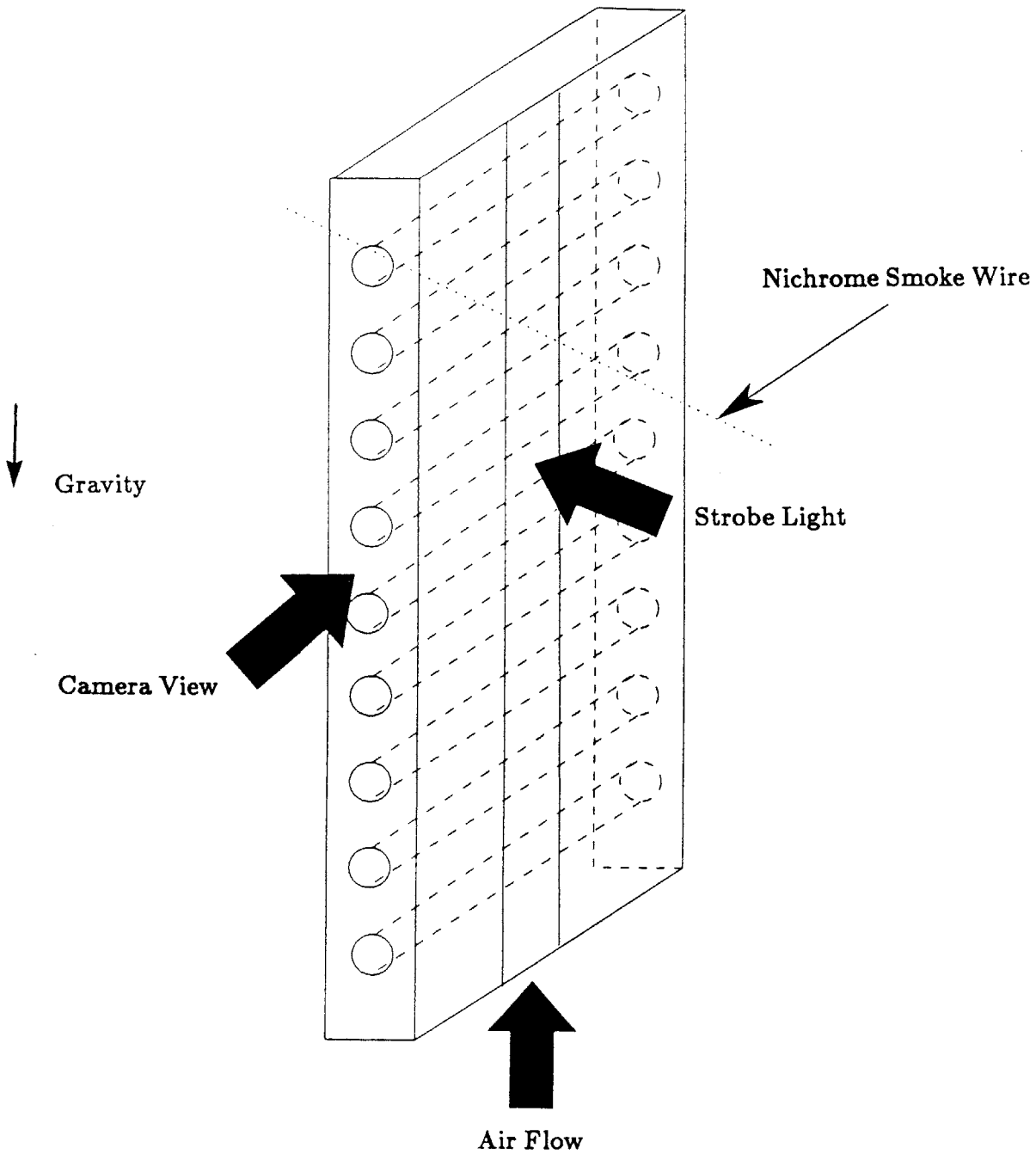

Nichrome Smoke Wire
Gravity
Strobe Light
Camera View
Air Flow

Figure 17

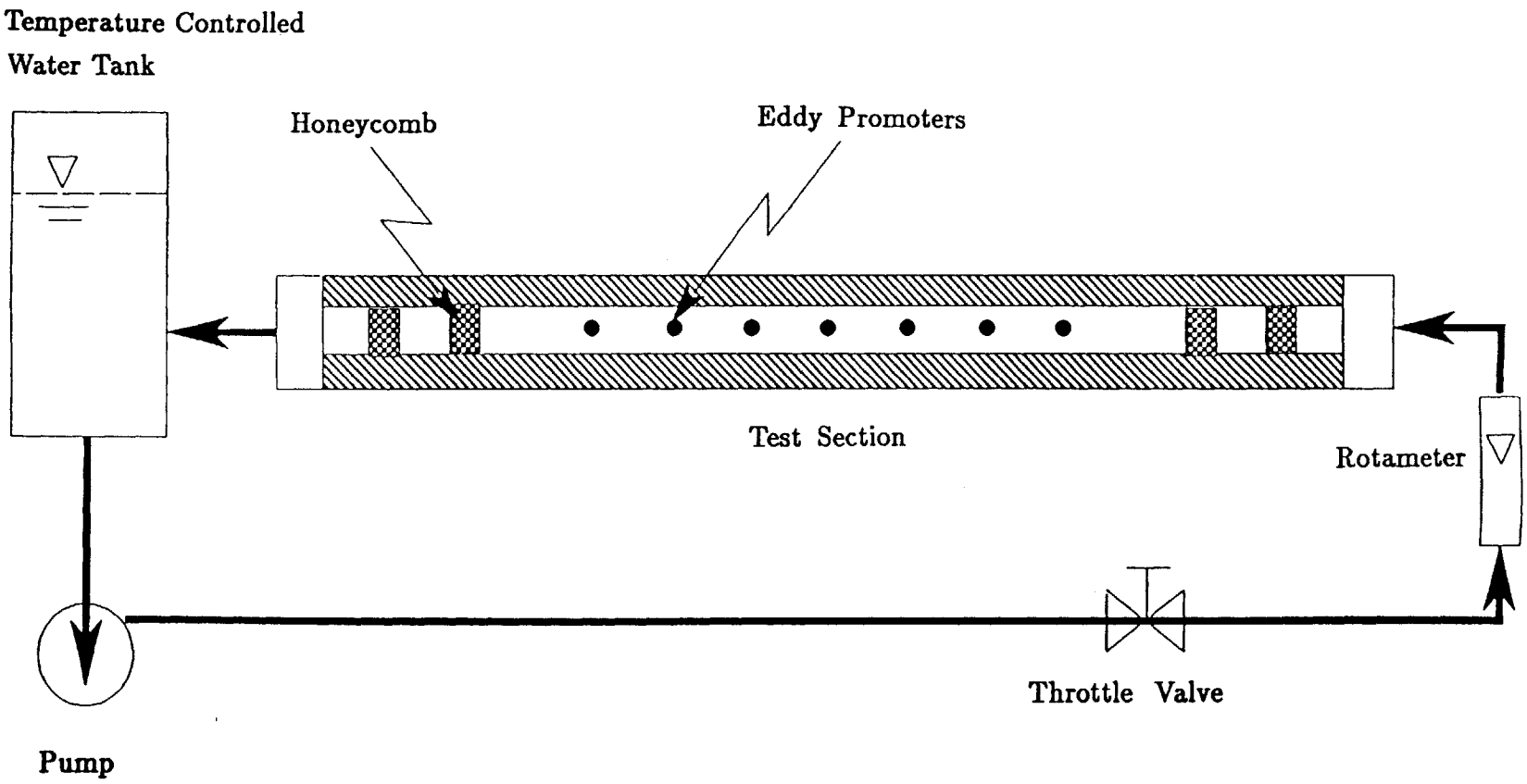

Temperature Controlled
Water Tank
Honeycomb
Eddy Promoters
Test Section
Rotameter
Throttle Valve
Pump

Figure 18

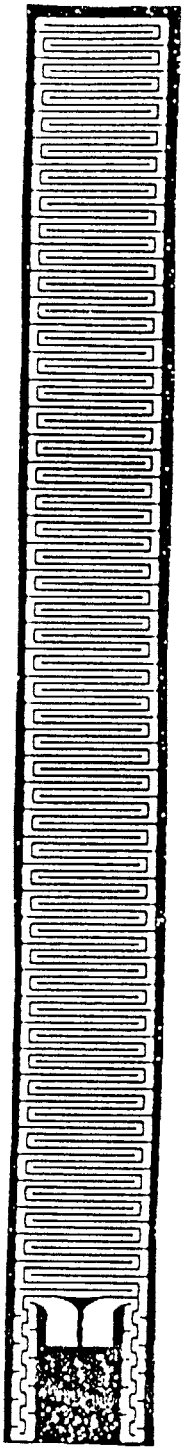


Figure 19

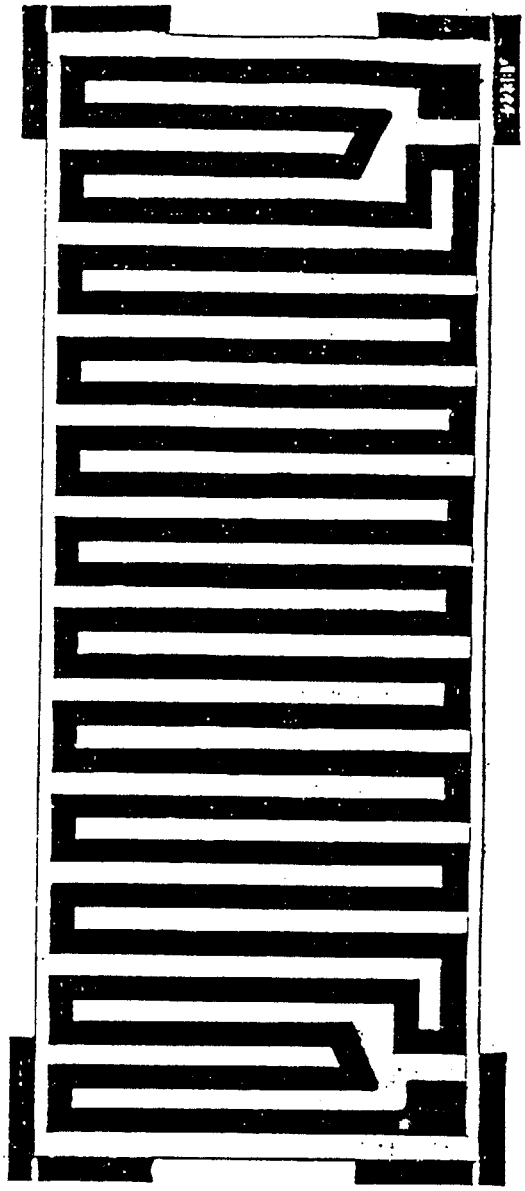


Figure 20

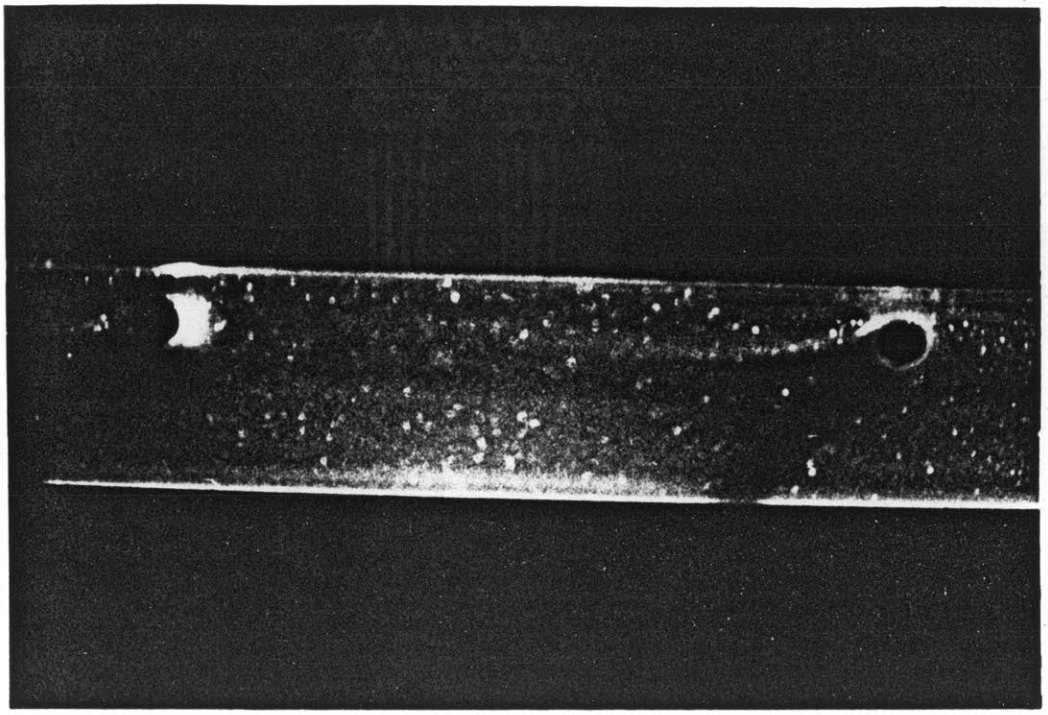


Figure 21

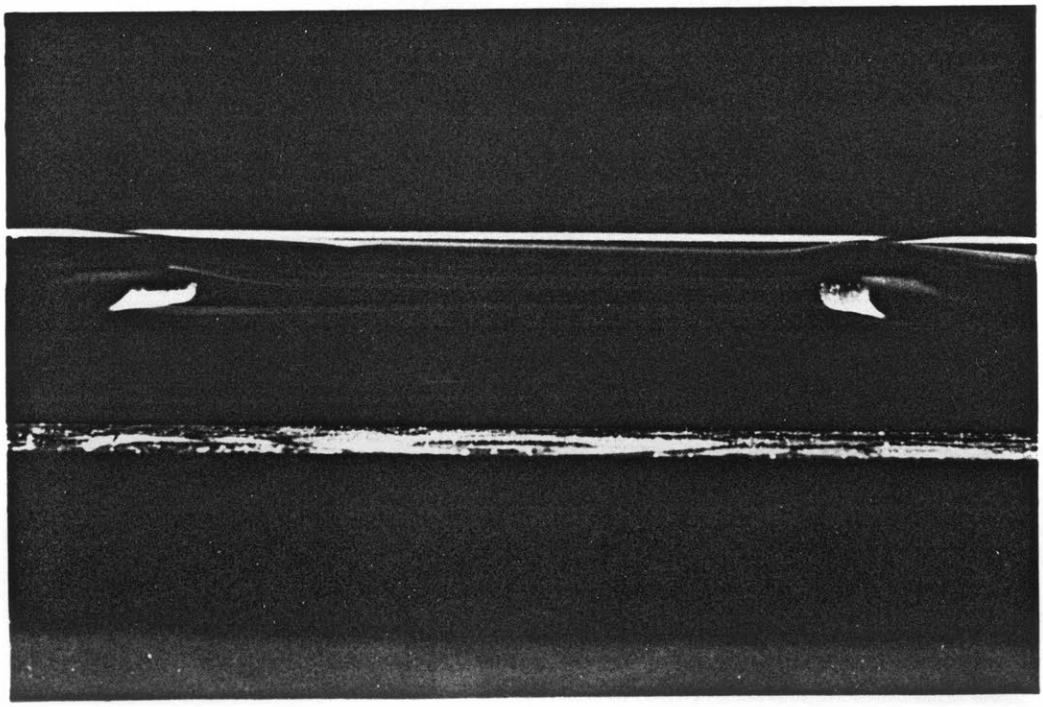


Figure 22

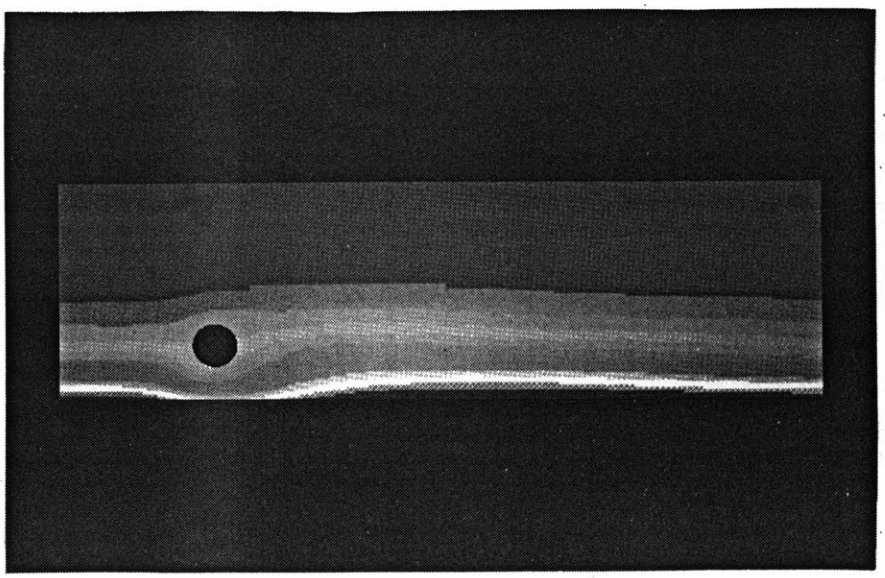


Figure 23

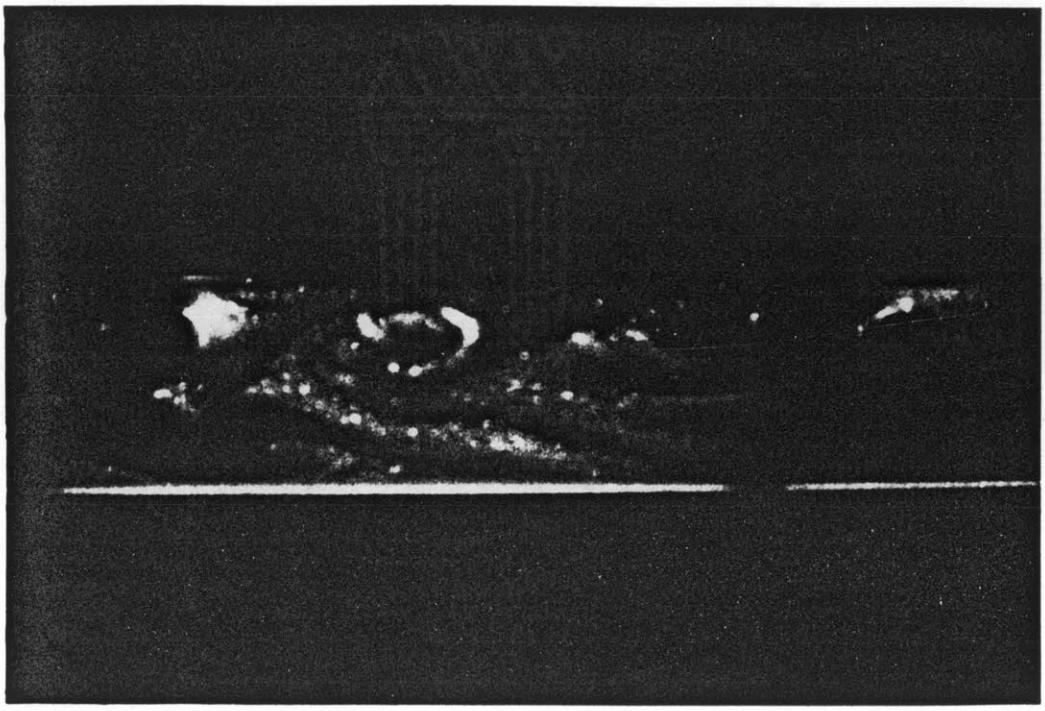


Figure 24

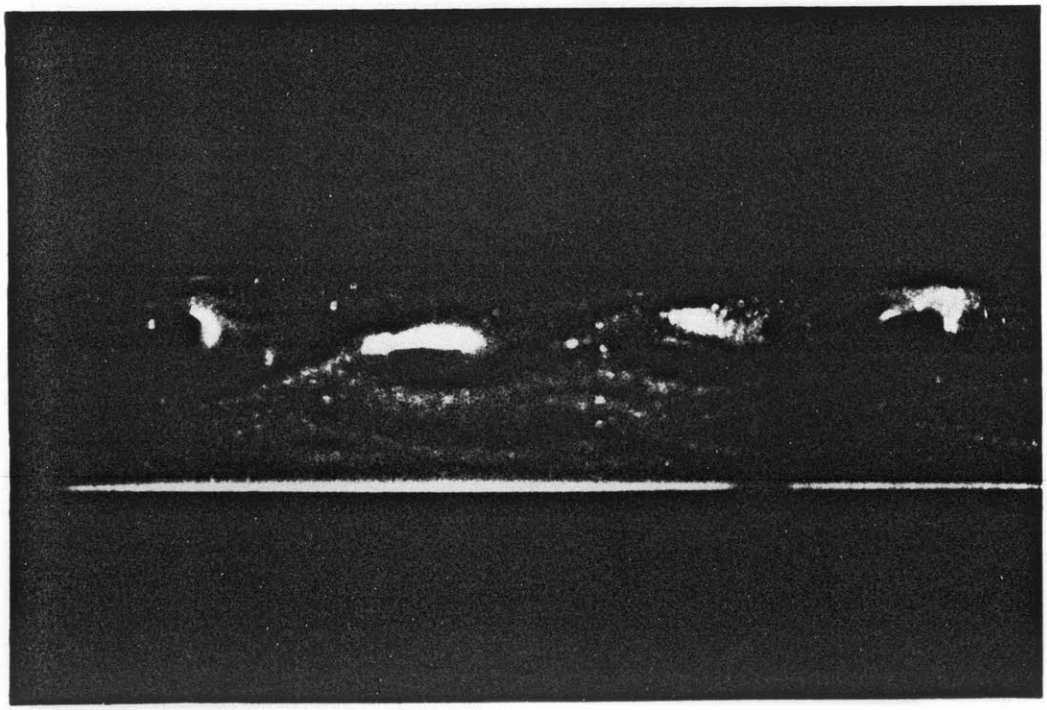


Figure 25

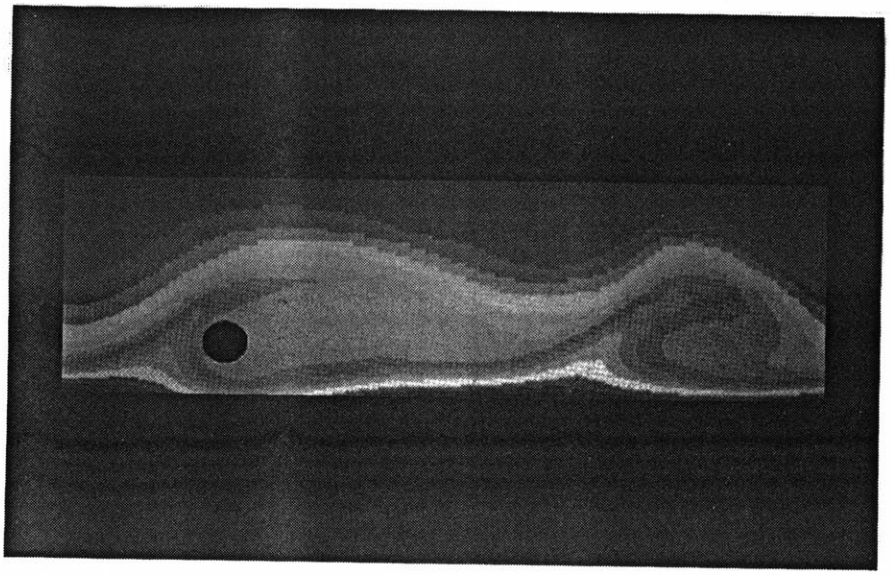


Figure 26

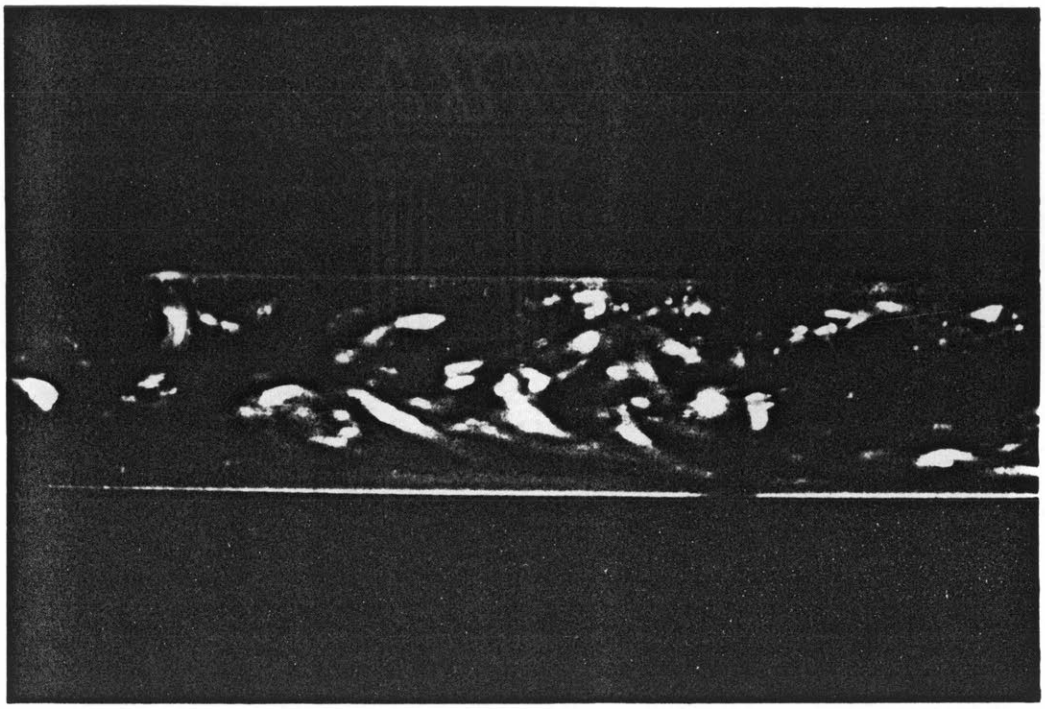


Figure 27

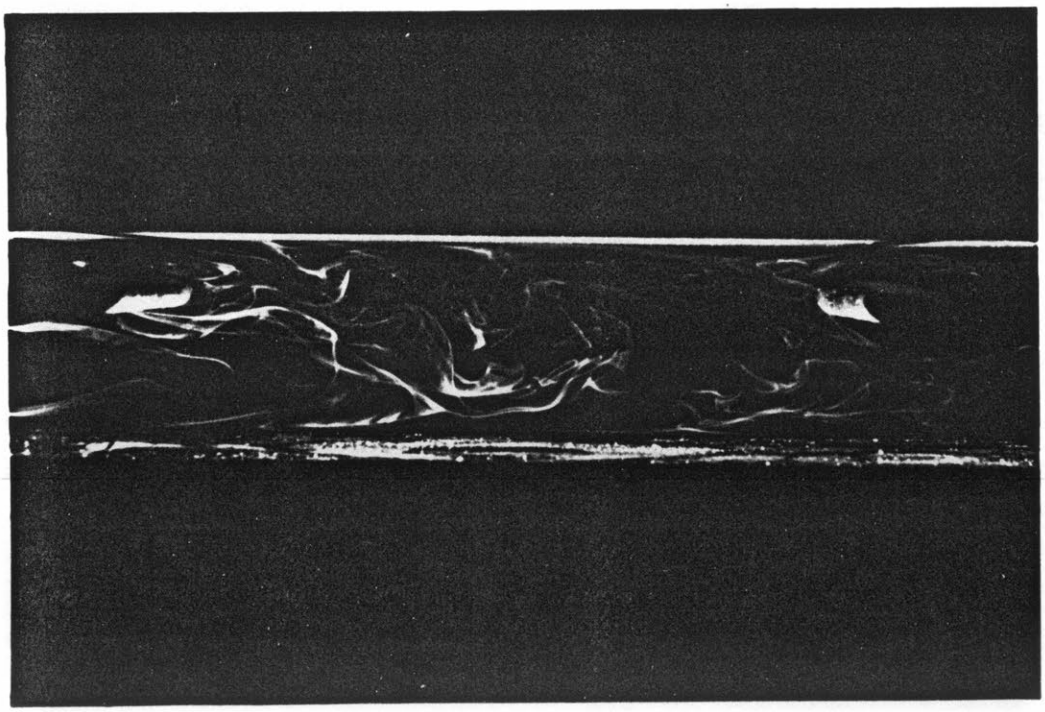


Figure 28

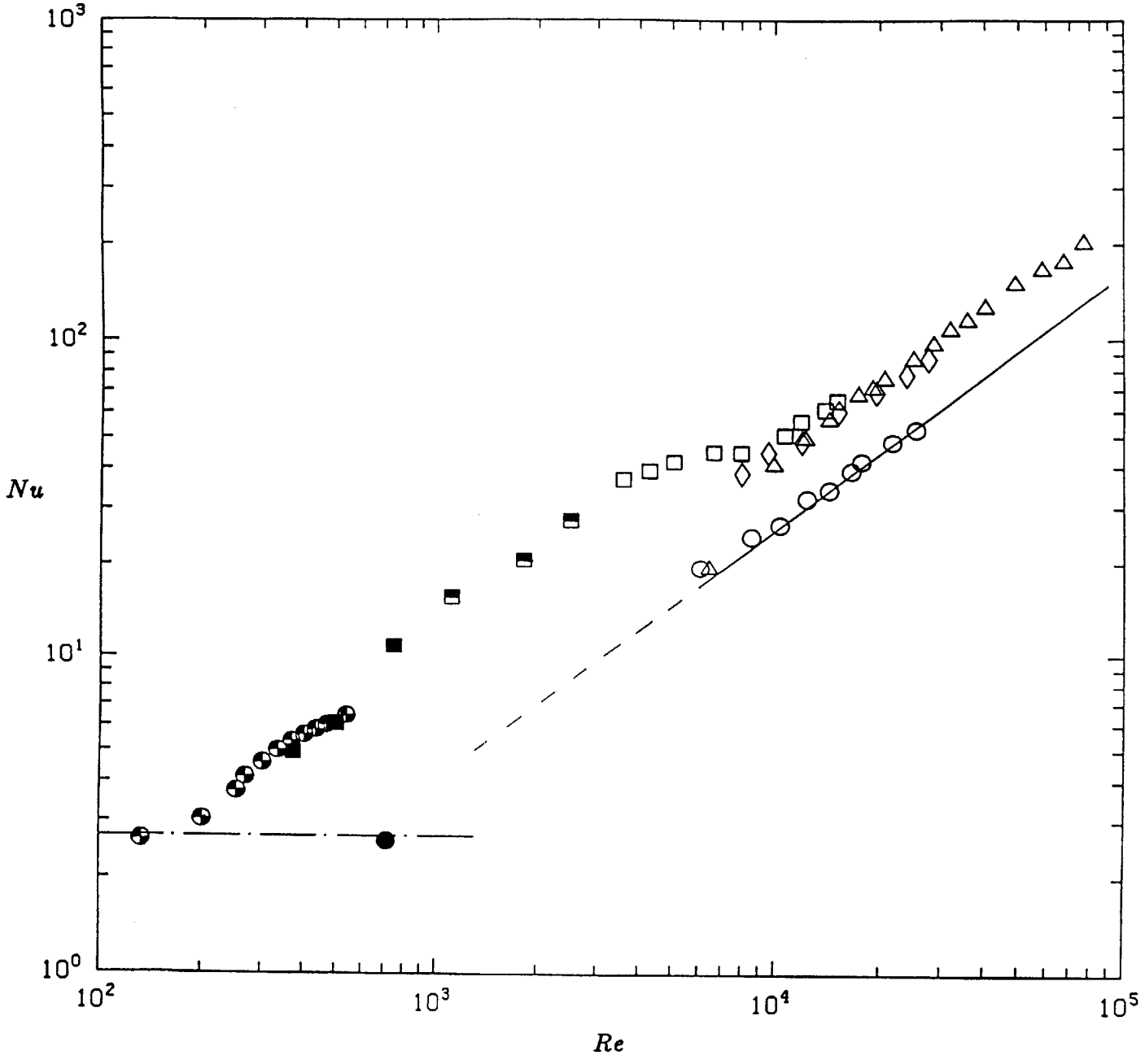


Figure 29

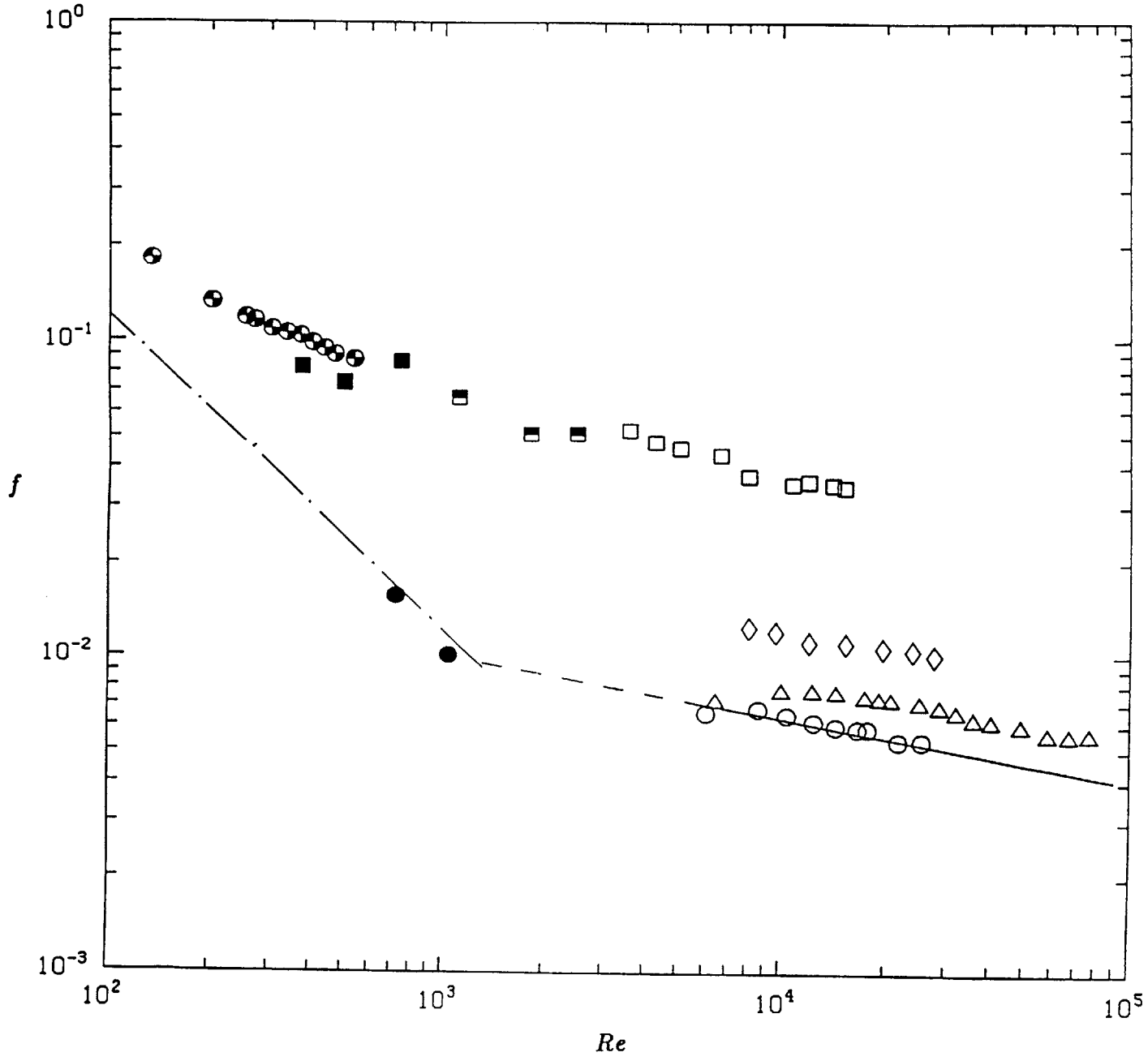


Figure 30

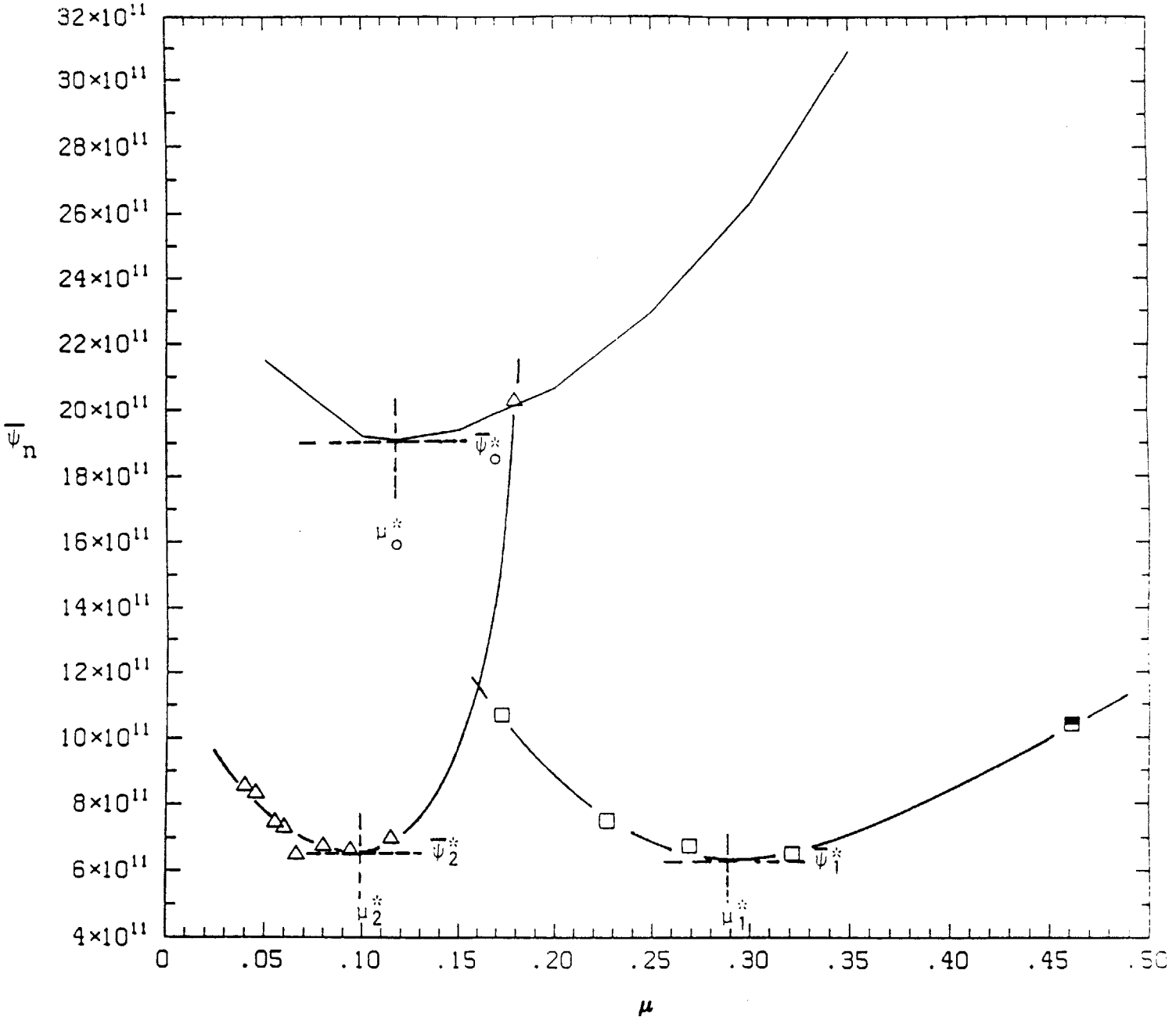

32×10^11
30×10^11
28×10^11
26×10^11
24×10^11
22×10^11
20×10^11
18×10^11
16×10^11
14×10^11
12×10^11
10×10^11
8×10^11
6×10^11
4×10^11
$\overline{\psi}_n$
0
.05
.10
.15
.20
.25
.30
.35
.40
.45
.50
μ
$\overline{\psi}_0^*$
μ_0^*
$\overline{\psi}_2^*$
μ_2^*
$\overline{\psi}_1^*$
μ_1^*

Figure 31

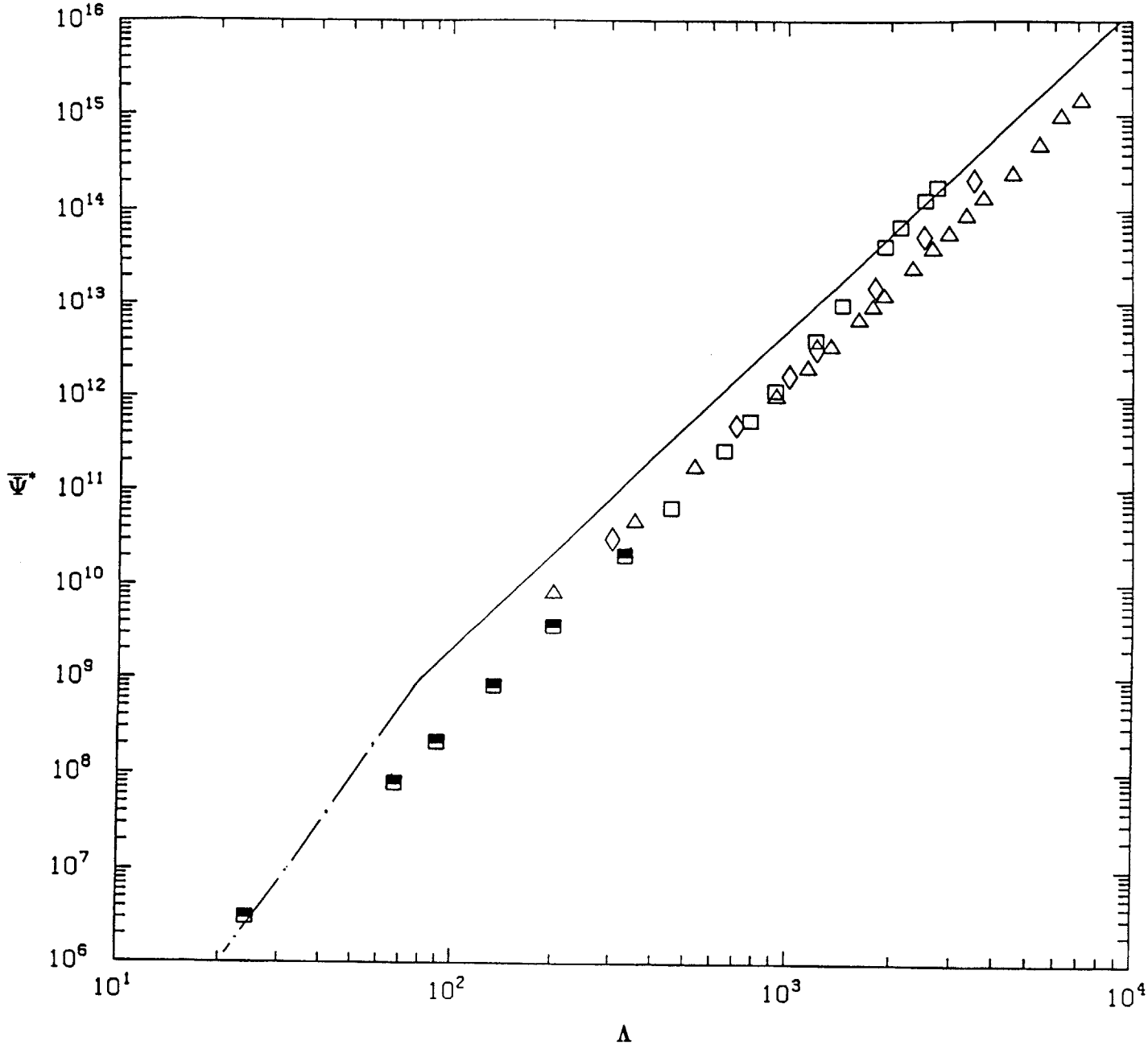

10^{16}
10^{15}
10^{14}
10^{13}
10^{12}
10^{11}
10^{10}
10^{9}
10^{8}
10^{7}
10^{6}
$\overline{\Psi}^*$
10^{1}
10^{2}
10^{3}
10^{4}
Λ

Figure 32

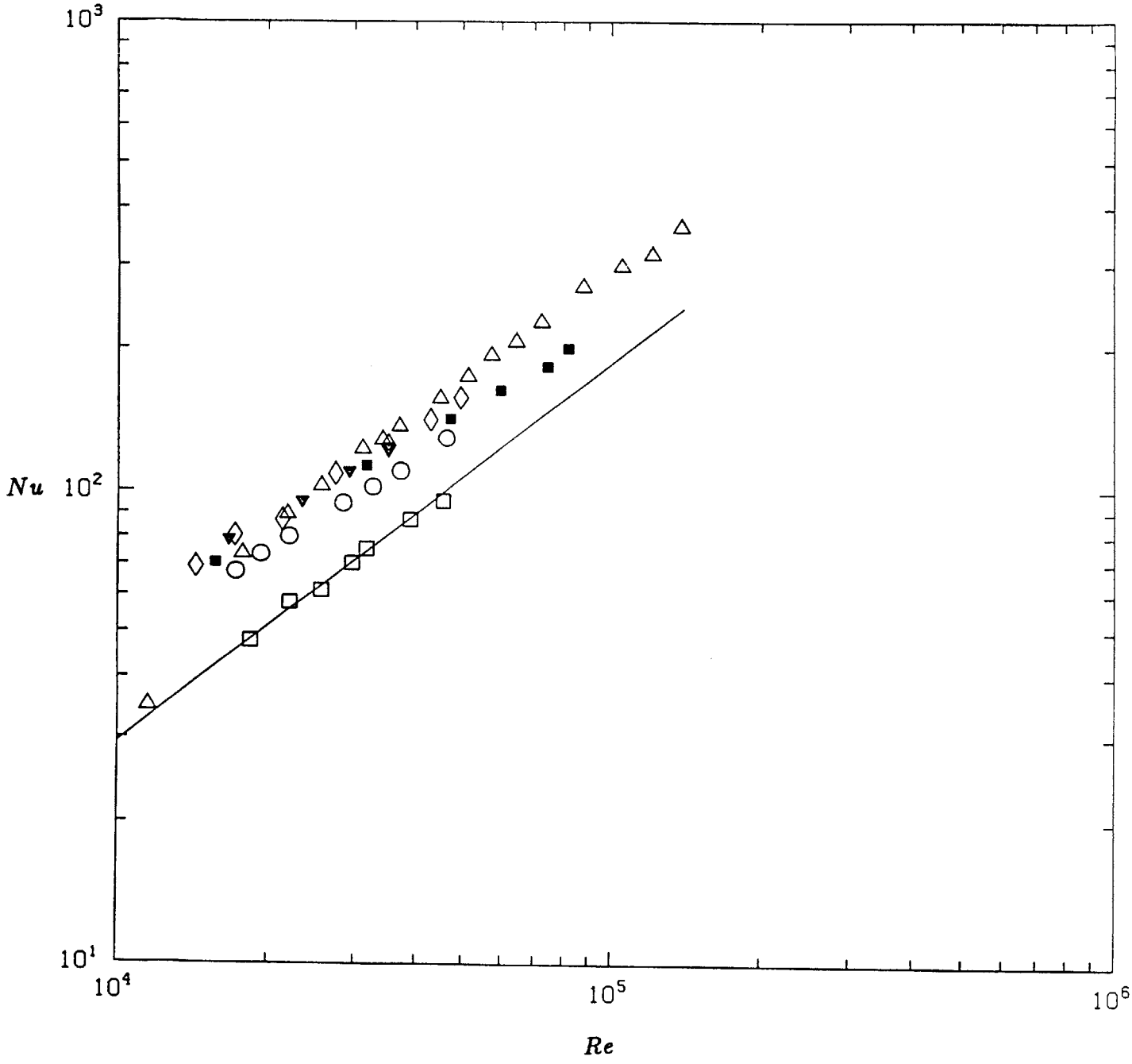


Figure 33

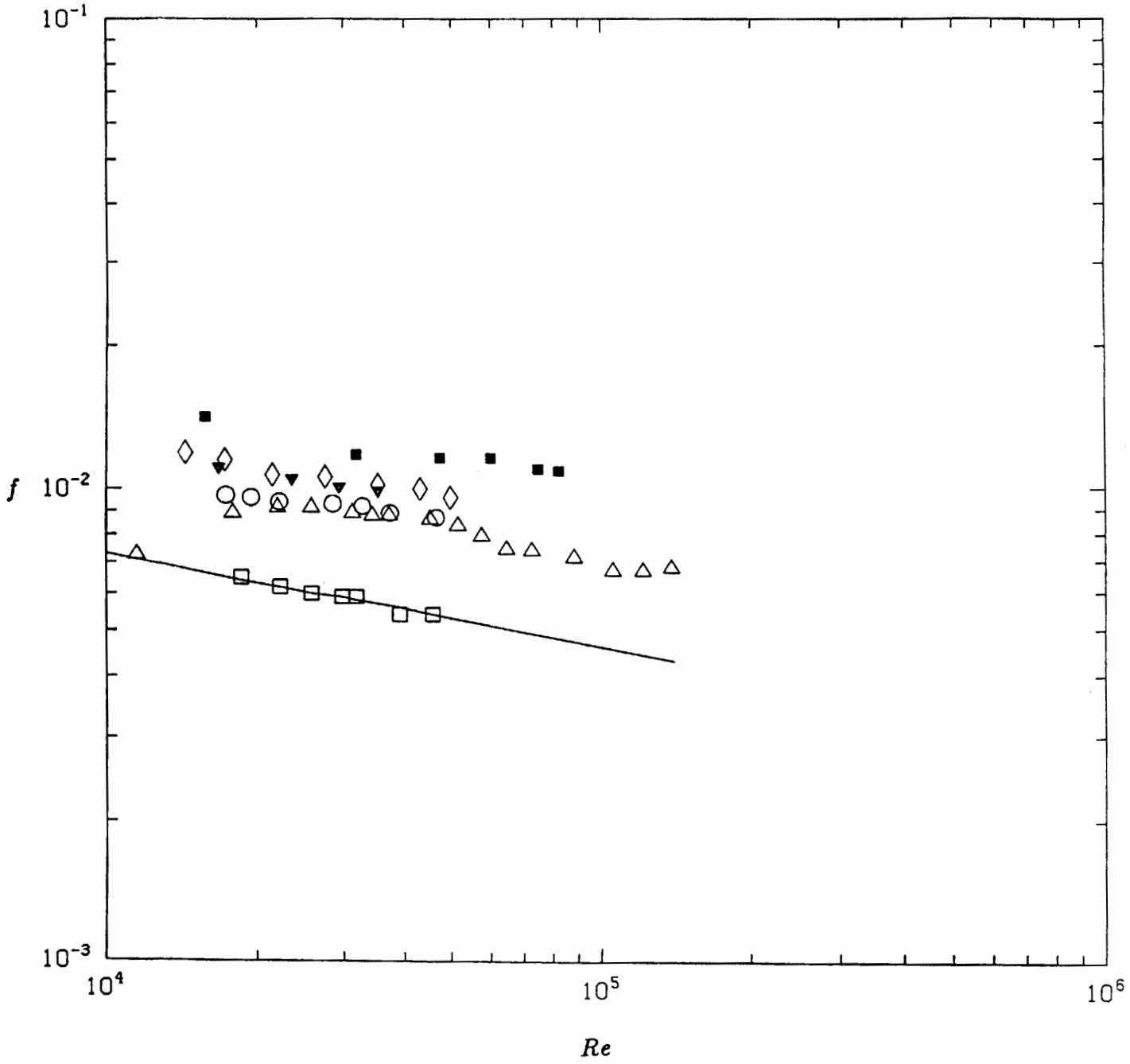


Figure 34

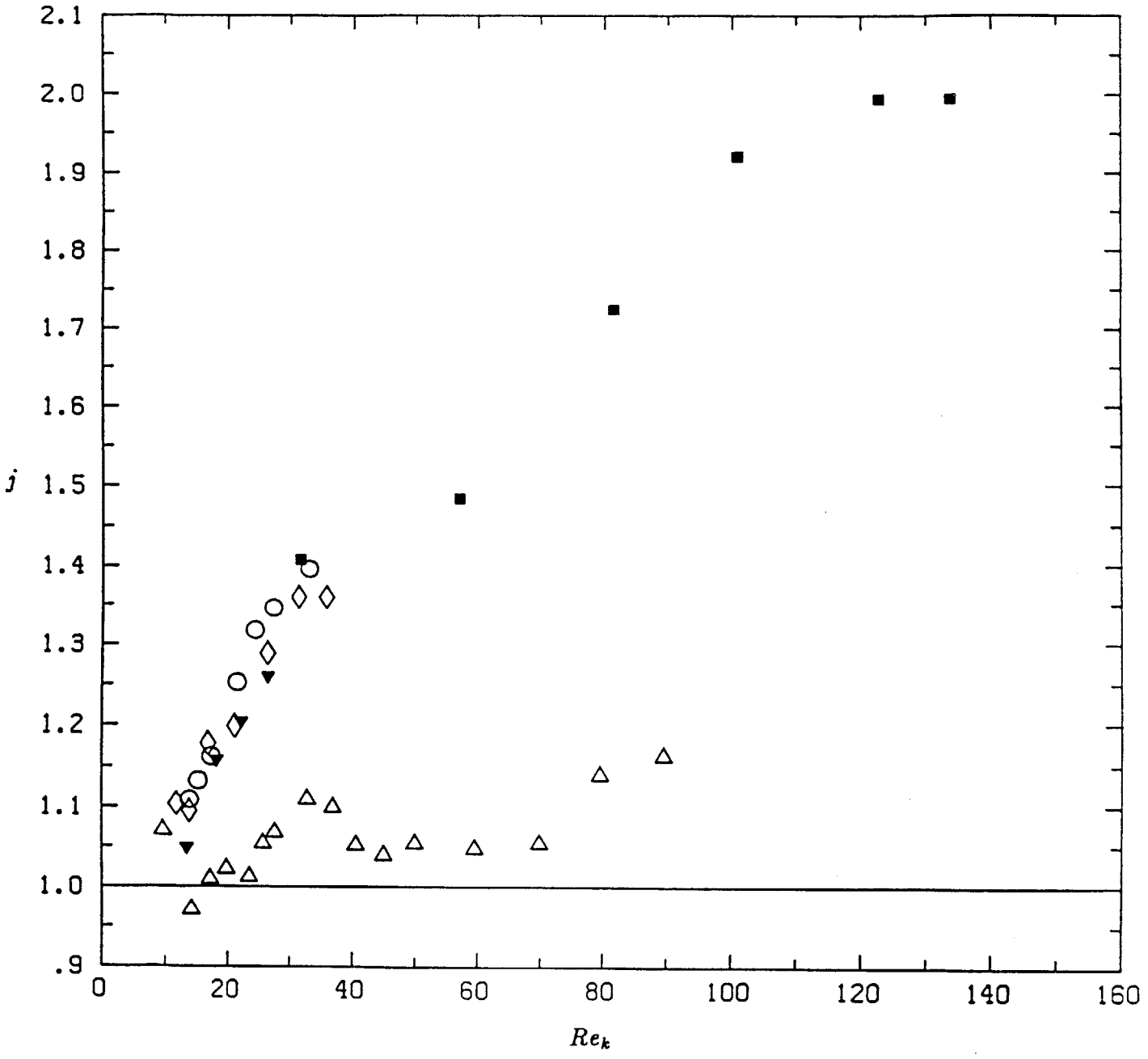

2.1
2.0
1.9
1.8
1.7
1.6
j
1.5
1.4
1.3
1.2
1.1
1.0
.9
0
20
40
60
80
100
120
140
160
Re_k

Figure 35

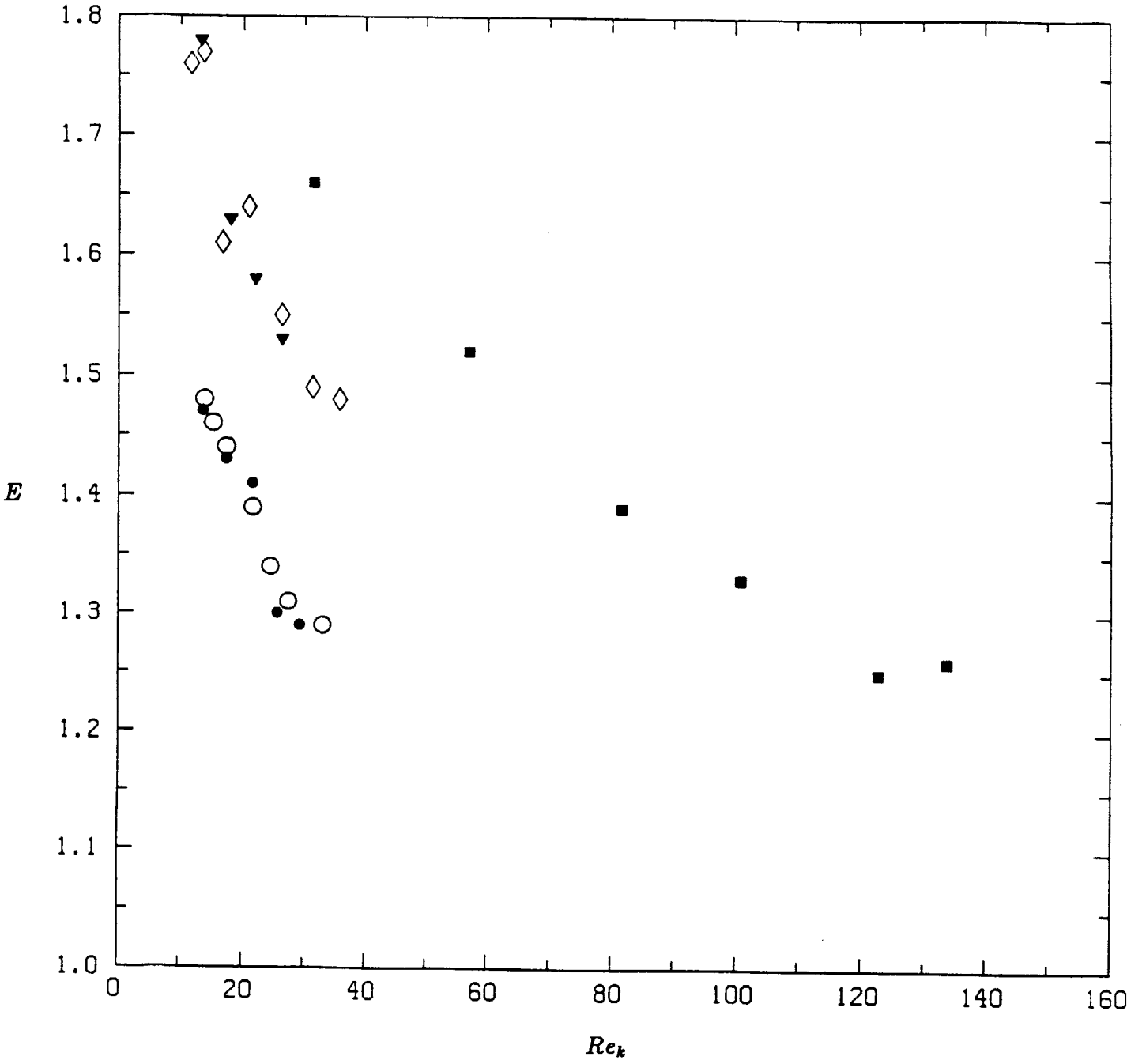


Figure 36

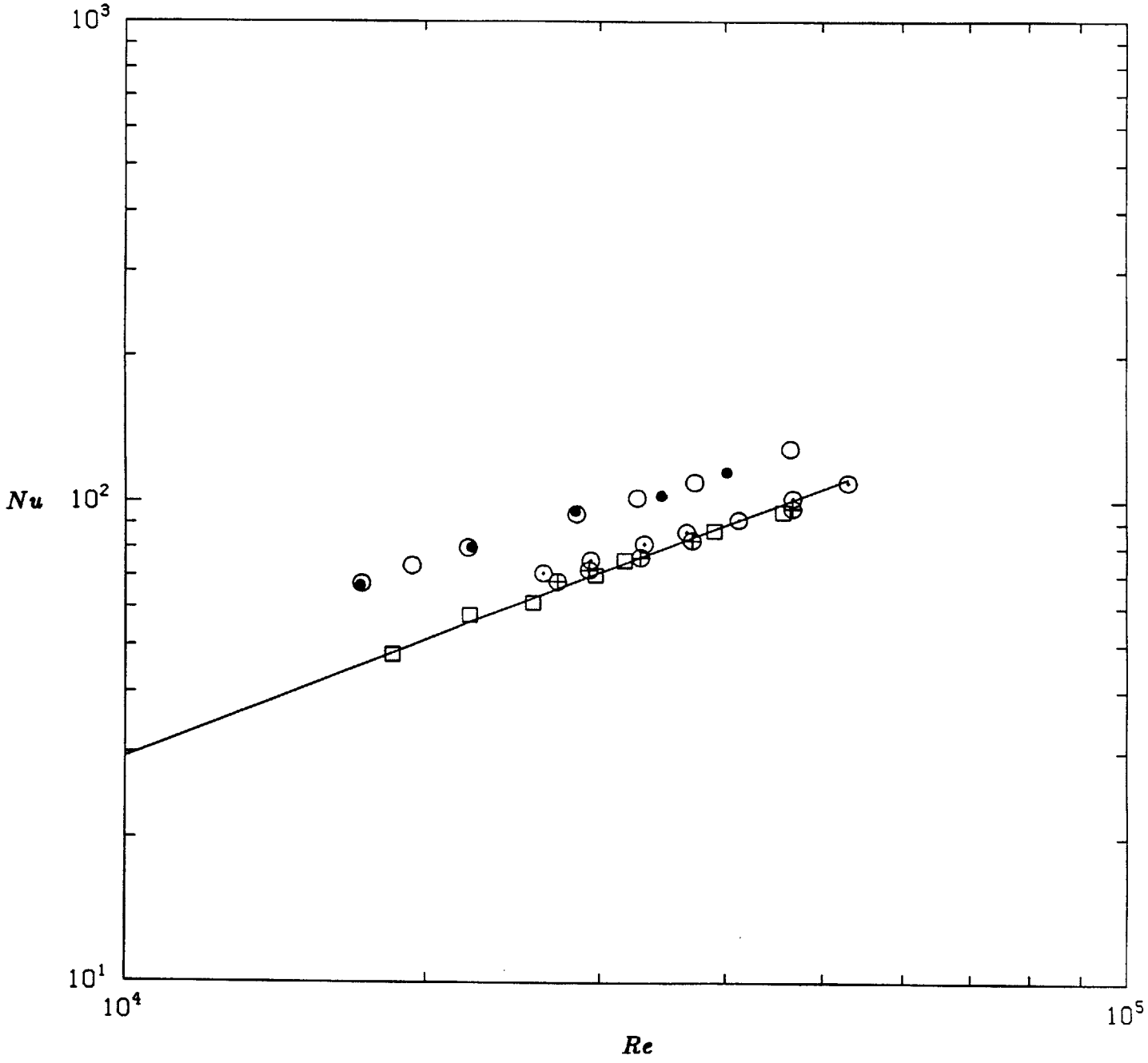


Figure 37

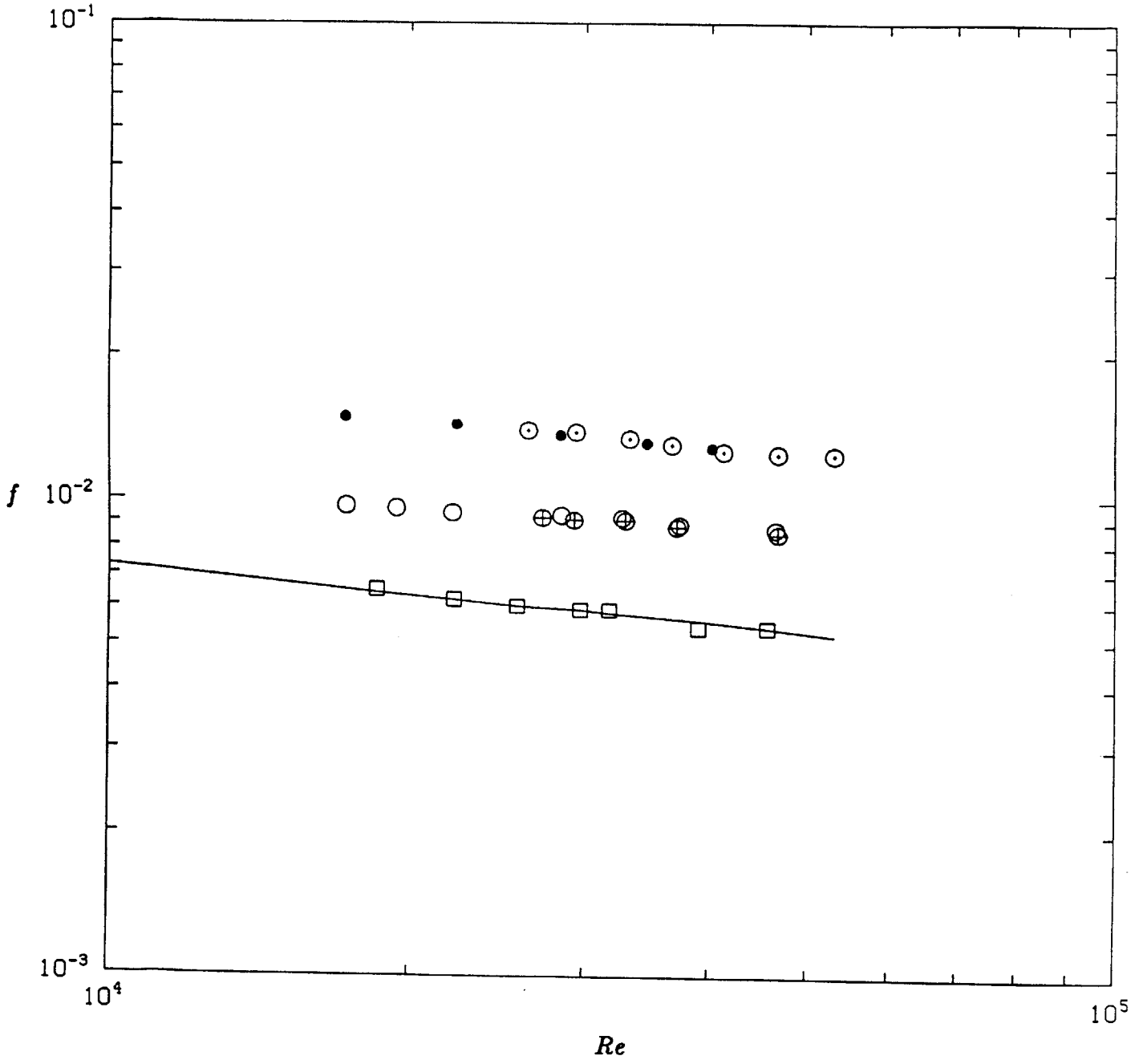


Figure 38

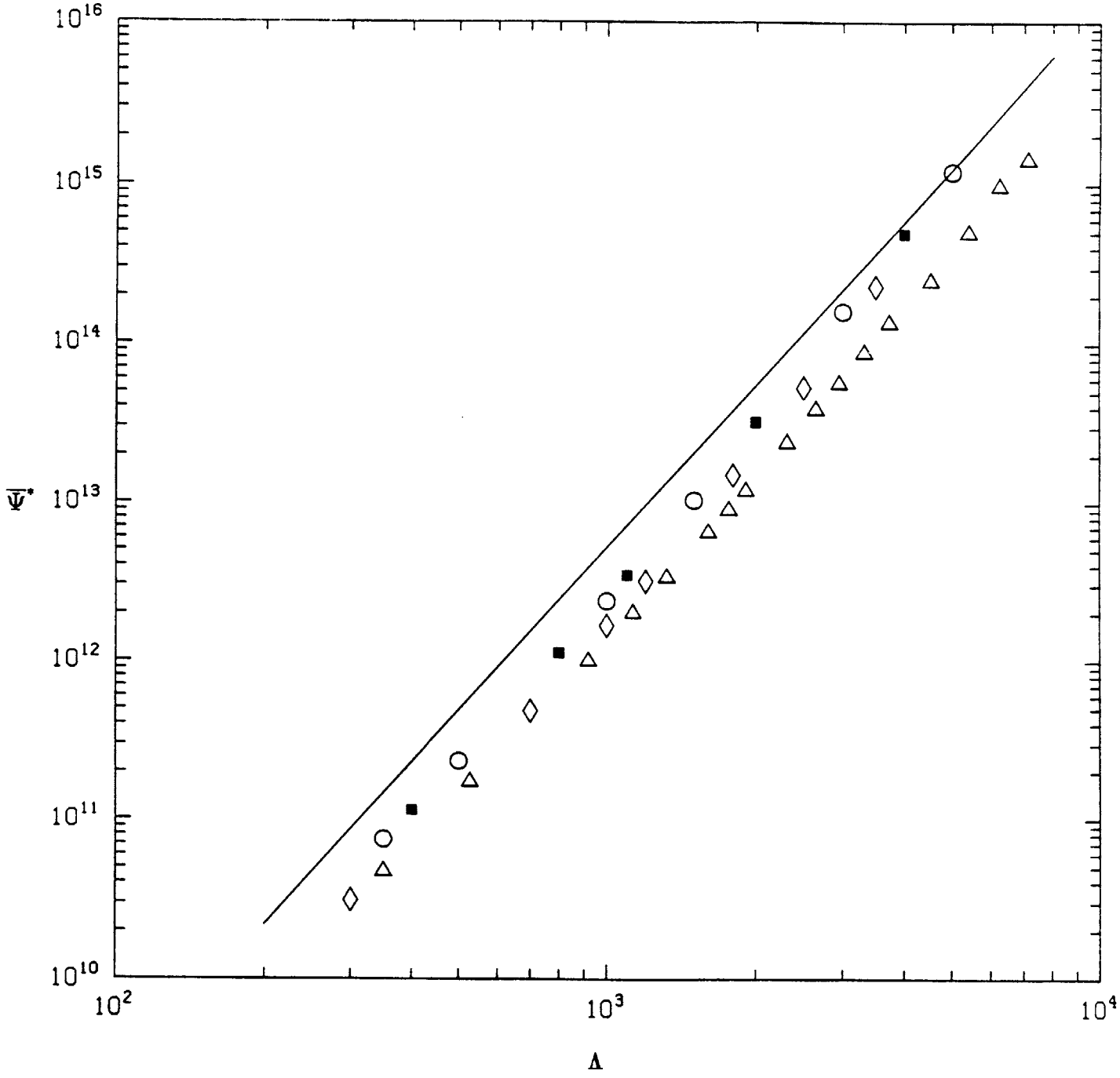

10^{16}
10^{15}
10^{14}
10^{13}
10^{12}
10^{11}
10^{10}
$\overline{\Psi}^*$
10^2
10^3
10^4
Λ

Figure 39